Direct Current Conductor Corona Modelling and Metrology

by

Abraham Johannes Otto

Dissertation presented for the degree of Doctor of Philosophy in Engineering at Stellenbosch University

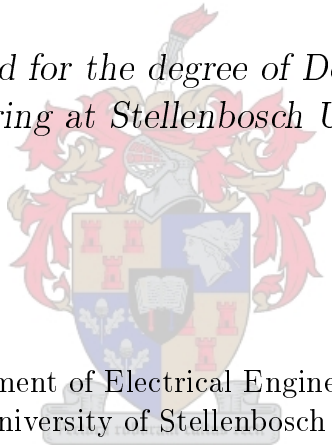

Department of Electrical Engineering
University of Stellenbosch
Private Bag X1, 7602 Matieland, South Africa

Promoter: Prof H.C. Reader
Chair of High Frequency Electronics
E&E Engineering
University of Stellenbosch

September 2009

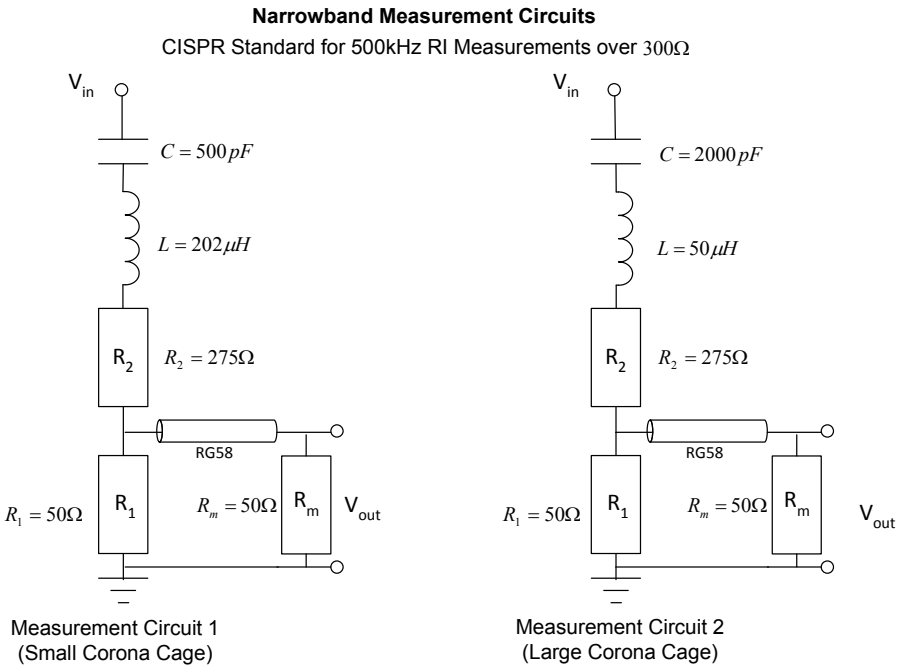

Figure 5.20: Schematics for CISPR narrowband measurement circuits as applied by Eskom for RI measurements over 300Ω

In [87] it is defined that the levels of radio noise (RN), generated by the conductors under test, are expressed in decibels (dB) relative to $1\mu V$ across 300Ω. The test circuit is calibrated accordingly and a correction factor is applied to the measured readings. The correction factor is given by the circuit attenuation (A) and resistive network factor (R) both measured in decibels (dB) as per equation 5.3.3.

$$V(dB/1\mu V/300\Omega) = V_m + A + R \tag{5.3.3}$$

If $R_1 = R_m$ as in figure 5.20, then R is given by

$$R = 20\log(\frac{600}{R_1}) \tag{5.3.4}$$

The transfer functions for the narrowband measurement circuits used on the small cage and large cage systems are shown in figures 5.21 and 5.22 respectively.

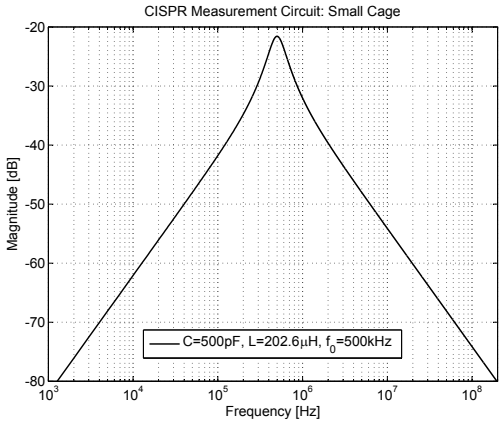

Figure 5.21: Transfer function for the CISPR standard measurement circuit used on the small corona cage

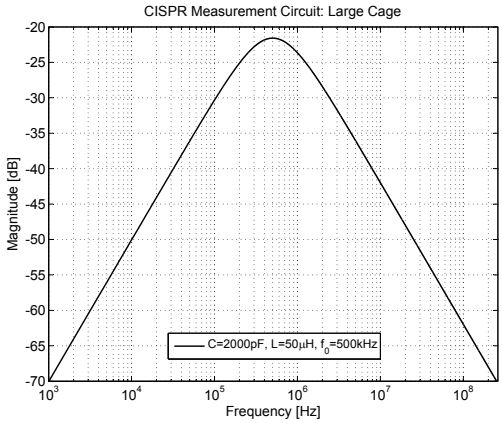

Figure 5.22: Transfer function for the CISPR standard measurement circuit used on the large corona cage at Megawatt Park

5.4 Radio Noise Meters

The block diagram for a typical radio noise (RN) meter is shown in figure 5.23. The RN measurement device used in this study adheres to the CISPR standard with a 500kHz tuned bandpass filter and 9kHz intermediate frequency (IF) bandwidth as the input. This means that the EMI receiver allows the centre frequency of 500kHz to be swept through a bandwidth of 9kHz at a specified number of points [9]. The output of the filter is fed into a detection network consisting of a half-wave rectifier, a weighting circuit and an indicating meter measuring the arithmetic mean value of the output voltage from the weighting circuit [88]. Such a radio noise meter is shown in figure 5.24.

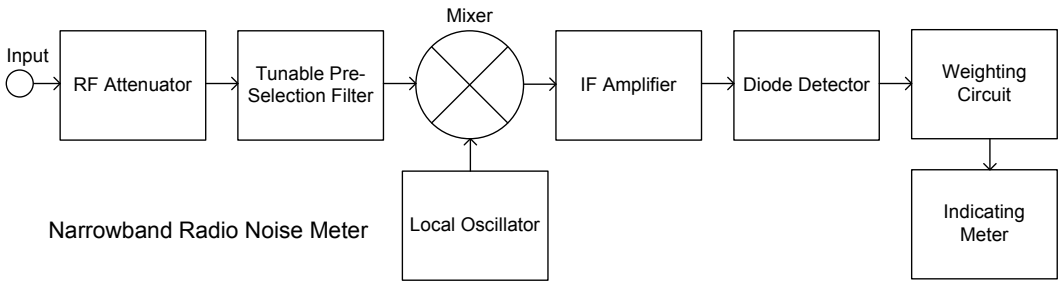

Figure 5.23: Block diagrams for a typical radio noise meter [9]

The three common detectors in radio frequency (RF) emissions measurements are peak (P),

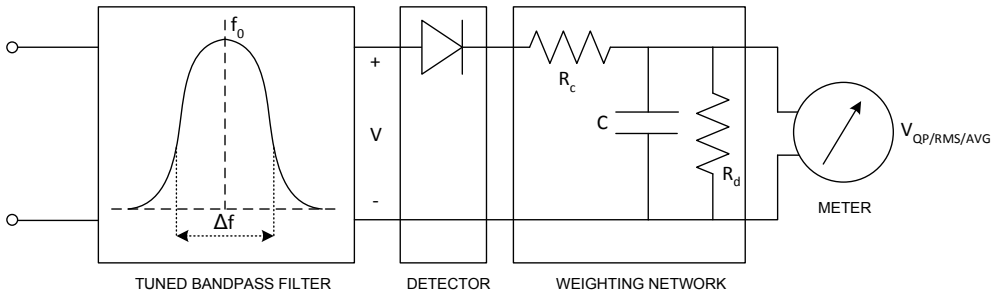

Figure 5.24: Schematic of a radio noise meter with quasi-peak detector [88]

quasi-peak (QP) and average (AVG) [89]. These are explained graphically in figure 5.25 for various waveforms. The characteristics of these measurements are different over frequency bands and are defined in [90]. The CISPR QP measurements are commonly made with the weighting network adjusted to a 1ms charging time constant and 160ms discharge time constant for the frequency band up to 30MHz.

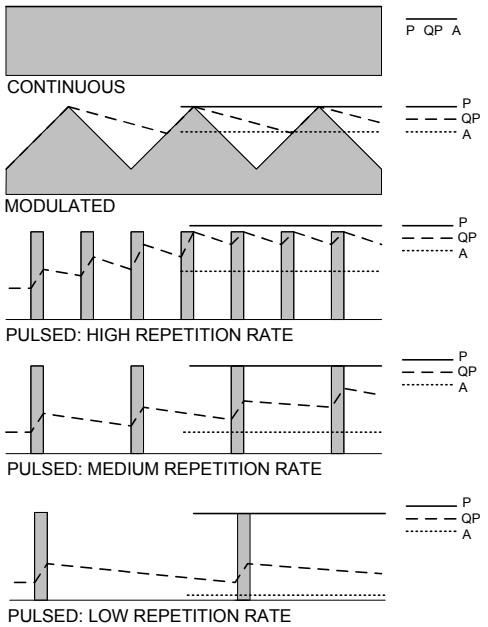

Figure 5.25: The indicated level versus the modulated waveforms for various detectors (P=Peak; QP=Quasi-Peak; A=Average) [89]

The other type of accepted RN measurements adhere to the *American National Standards Institute* ANSI standard with a 1MHz tuned bandpass filter and a 5kHz bandwidth as the input.

The ANSI receivers have a 1ms charging time constant and a 600ms discharge time constant. It was found in [88] and [55] that that when the repetition rate of the pulses approach the receiver bandwidth, the ANSI with a narrower bandwidth reaches the peak reading at a lower repetition rate. This can be seen in the graphical explanation for the high repetition rate in figure 5.25. Due to the wider bandwidth and faster discharge time, the CISPR meter has more dynamic range than that of the ANSI meter. The CISPR meter was used for all frequency domain measurements discussed in this dissertation. The QP, RMS and AVG levels for an ideal RN meter were derived in [88] as per equations 5.4.1 to 5.4.3.

$$i_c = \frac{R_d}{R_c} \int_{V=V_{QP}}^{\infty} \frac{V - V_{QP}}{R_c} p(V) dV \tag{5.4.1}$$

$$V_{RMS} = \sqrt{\int_0^{\infty} V^2 p(V) dV} \tag{5.4.2}$$

$$V_{AVG} = \int_0^{\infty} V p(V) dV \tag{5.4.3}$$

where i_c is the average charge current that is equal to the average discharge current, R_d, R_c, V and V_{QP} are as shown in figure 5.24 and $p(V)$ is the amplitude probability density function (pdf).

5.5 Importance of Impedance Matching in Wideband Corona Measurements

To investigate the importance of correct impedance matching during wideband measurements, a small laboratory corona cage of radius R=400mm and length 1.8m, with a smooth aluminium conductor of radius of r=7mm were used as in figure 5.26. Small conical artificial corona sources were formed out of conductive silicone rubber and placed on the smooth conductor at uniformly spaced positions. This would be similar to field enhancements caused by water droplets that form on a conductor during rain conditions, which was modelled in [91]. The artificial corona sources would generate corona at a much lower surface voltage gradient than that of the smooth aluminium conductor. This would ensure that the partial discharges measured are only from

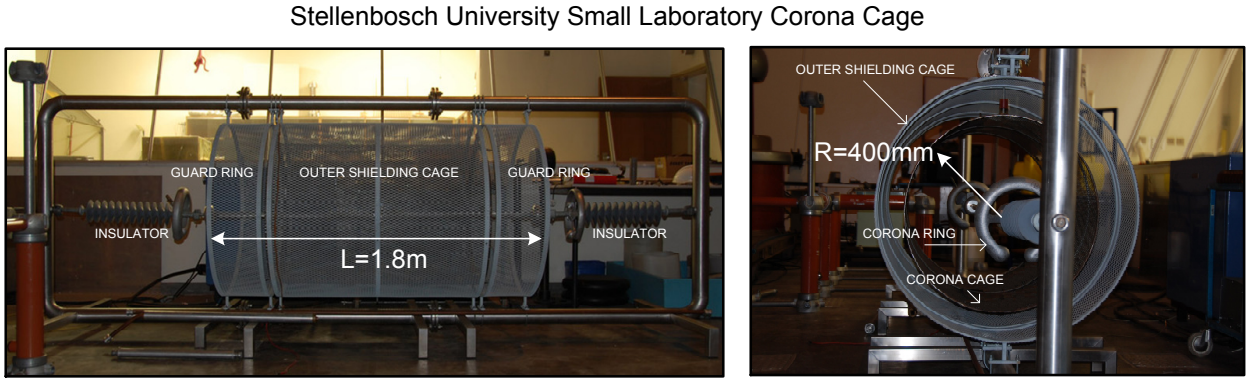

Figure 5.26: Small laboratory corona cage at the University of Stellenbosch

the sources at known positions. The number of sources would help limit and control the number of discharges and repetition rate between these discharges. Discharges for single and multiple artificial corona sources at various surface voltage gradients were recorded visually with an ultra-violet (UV)) intensifying camera, and are shown figures 5.27 and 5.28 respectively. More captured images are shown in appendix B.

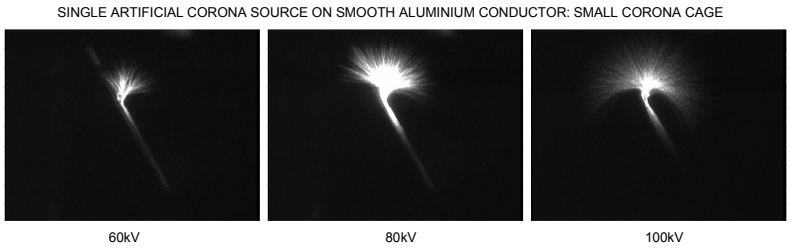

Figure 5.27: Various positive voltages applied to single artificial source on smooth aluminium conductor in small corona cage

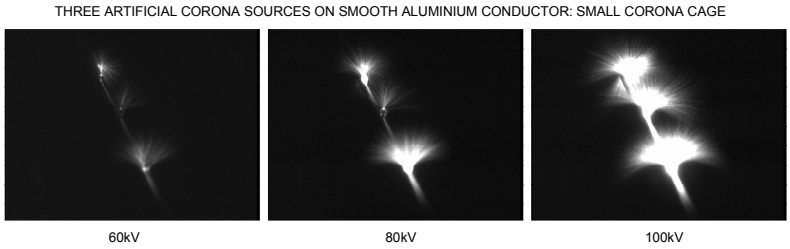

Figure 5.28: Various positive voltages applied to three artificial sources on smooth aluminium conductor in small corona cage

These measurements were done at sea level using a coupling capacitor and matching impedances to capture the corona events on the conductor. The effects of having the one side of the corona cage open-circuited, or unmatched, were compared to having it matched in its characteristic impedance as shown in figure 5.29.

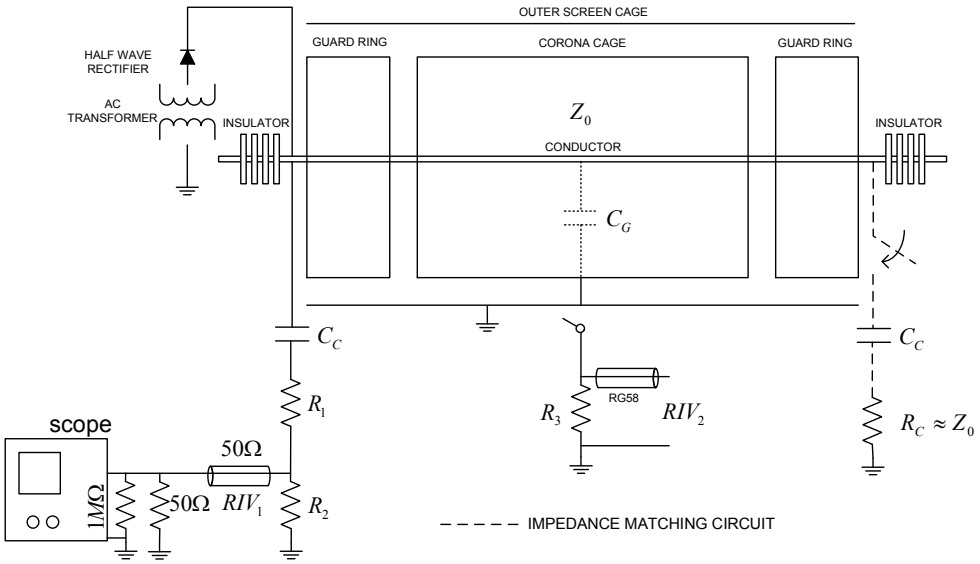

Figure 5.29: Schematic of small laboratory corona cage with characteristic impedance matching circuit

5.5.1 Termination Into Characteristic Impedance

The capacitance (C) and the inductance (L) of the measurement geometry are used to approximate the characteristic impedance of the system such that

$$Z_0 \approx \sqrt{\frac{L}{C}} \tag{5.5.1}$$

where L is given by 5.5.2 and C is given by 5.5.3 for a corona cage of radius R, conductor radius r and length l.

$$L = \frac{\mu_0}{2\pi} \ln(\frac{R}{r}) l \tag{5.5.2}$$

$$C = \frac{2\pi\epsilon_0 l}{\ln(\frac{R}{r})} \tag{5.5.3}$$

The permeability and premittivity of free space is given by $\mu_0 = 4\pi \times 10^{-7} H/m$ and $\epsilon_0 = 8.854 \times 10^{-12} F/m$ respectively. In the case of a test line, the term R in equations 5.5.2 and 5.5.3 can be approximated by $R \approx 2H$, where H is the height of the conductor above the ground plane [11]. The resistor values of the measurement circuit, shown in figure 5.29, were chosen such that the impedance looking from the cage is matched in $R_1 + R_2 = Z_0$, while the impedance looking from the 50Ω measurement cable is matched in $R_2||(R_1 + Z_0) = 50\Omega$. Care was taken to terminate the measurement cable going to the high input impedance oscilloscope into a 50Ω shunt resistor in order to avoid any reflections. A similar approach to matching the measurement system was discussed in [92].

5.5.2 Time Domain Parameter Definitions

The rise time, t_r, is defined between the 10% and 90% values of the maximum amplitude on the rising edge such that

$$t_r = t_{90} - t_{10} \tag{5.5.4}$$

This is similar for the fall time, t_f, which is between the 10% and 90% values of the maximum amplitude on the falling edge of the pulse. The pulse duration, t_d, is defined between the 10% values of the rise and fall time of the pulse. These times are shown in figure 5.30.

5.5.3 Unmatched System Time Domain Measurements

An attempt was made to measure single pulses beyond the corona inception level in the time domain using an unmatched measurement system. Two arrangements were considered in the small laboratory cage: 1) a single artificial corona source in the middle of the conductor, 2) multiple artificial corona sources uniformly spaced. Examples of captured time domain pulses for these two cases are shown in figures 5.31 and 5.32 respectively. The current produced by the empirical formula, given by equation 2.5.1, is also plotted.

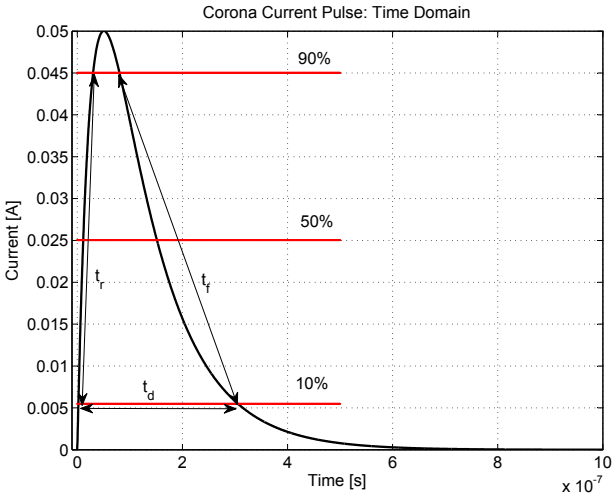

Figure 5.30: Positive corona current pulse with rise time, fall time and pulse duration definition

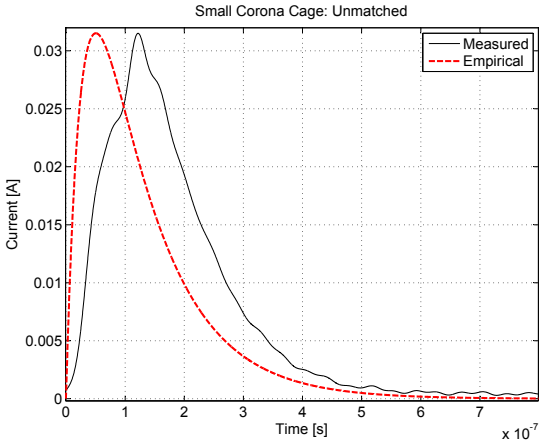

Figure 5.31: Typical distorted positive corona current pulse measured with unmatched system and single artificial corona sources

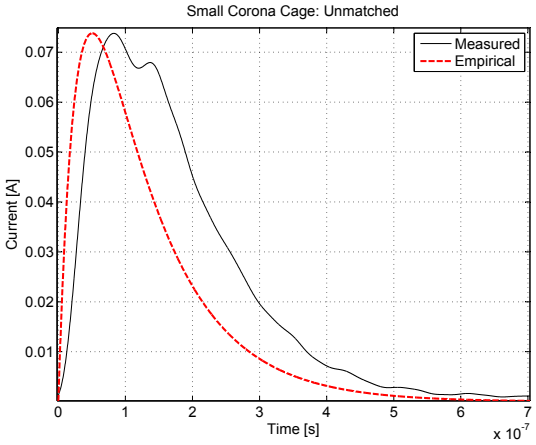

Figure 5.32: Typical distorted positive corona current pulse measured with unmatched system and multiple artificial corona sources

Although the basic pulse shape was generally captured for a single source, the multiple sources delivered pulses that were quite deformed and distorted. For each corona current pulse injected into the conductor at the artificial source, the pulse reaching the matched coupling capacitor circuit will be absorbed, while the pulse reaching the open circuit will be reflected back on to the conductor. This would immediately imply more pulses than those injected at the corona sources will propagate on the conductor under test. This leads to an increase in pulse repetition as well as pulse distortion due to superposition. It also makes it difficult to measure single corona events beyond inception. The effect increases more so when a higher surface voltage gradient is applied to more sources.

5.5.4 Matched System Time Domain Measurements

Next, both ends of the corona cage were terminated in its characteristic impedance as in figure 5.29. Again time domain measurements were taken for 1) a single artificial corona source in the middle of the conductor, 2) multiple artificial corona sources uniformly spaced. For the single corona source, pulse shapes were recorded that correlated with the empirical formula presented in equation 2.5.1, and an example is shown in figure 5.33.

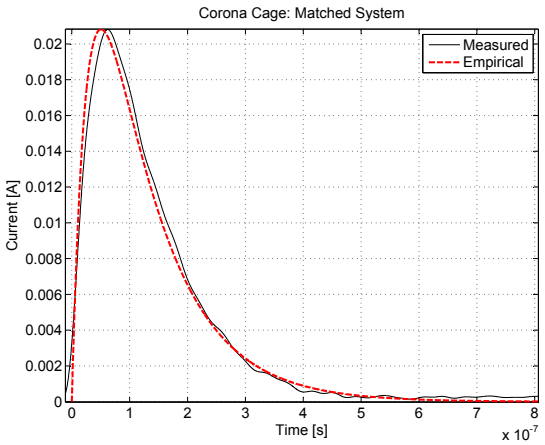

Figure 5.33: Time domain data for typical positive corona current pulse captured on matched system

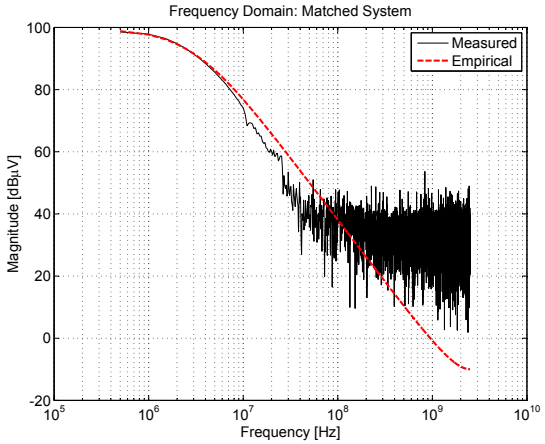

Figure 5.34: Frequency domain data for typical positive corona current pulse captured on matched system

The frequency domain data for the captured and empirical time domain pulses were calculated using the *Fast Fourier Transform* (FFT), and are shown in figure 5.34 as dB over $1\mu V$. Single pulses were also captured for the case of multiple sources, although some degree of pulse shape distortion was sometimes noticed at higher surface voltage gradients. This is due to the

superposition of pulses being injected into the conductor at a source, while pulses from a neighbouring source are already propagating in the same direction. The variation of the matched and unmatched average amplitude measurements and the empirical values for typical positive corona pulses, discussed in section 2.5.1, are shown in figures 5.35 and 5.36.

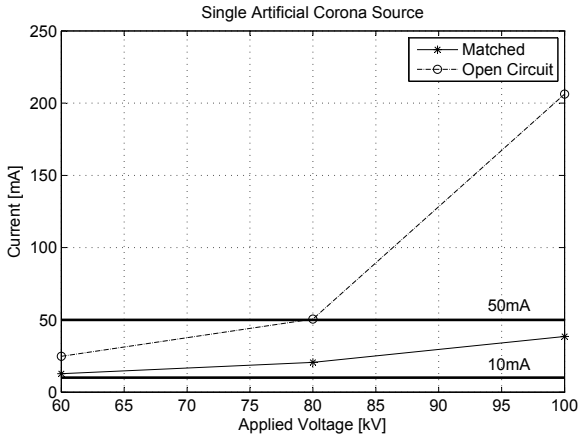

Figure 5.35: Amplitude variation between single source measurements in matched and unmatched systems and empirical values

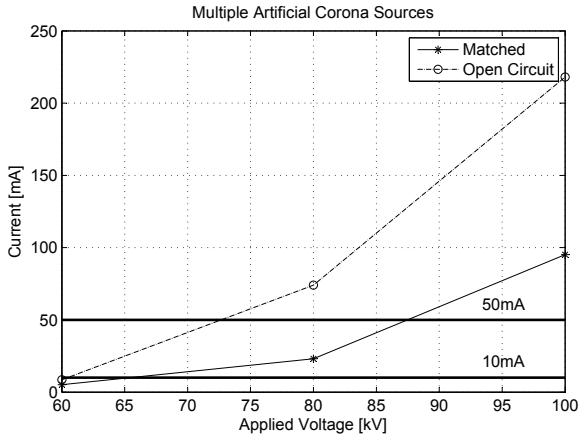

Figure 5.36: Amplitude variation between multiple source measurements in matched and unmatched systems and empirical values

5.5.5 Frequency Domain Measurements

Frequency domain measurements were made on a wideband measurement system using a *Rohde & Schwarz* EMI receiver with a pre-selection filter centre frequency of 500kHz (bandwidth of 9kHz). The quasi-peak results measured in $dB\mu V$ are again for 1) a single artificial corona source in the middle of the conductor, 2) multiple artificial corona sources uniformly spaced. These QP results are shown in figures 5.37 and 5.38. It was noted in [93] that the QP reading of a RN meter depends upon the amplitude and charge content of the higher corona pulses, and it is therefore important to minimise the pulse distortion due to superposition when impedance mismatches are present.

The laboratory corona cage was again either open circuited or matched in its characteristic impedance Z_0. This is different to the CISPR narrowband measurement that uses an inductor to resonate with the coupling capacitor in the measurement circuit, hence only allowing the one frequency component through to the RN meter. In the wideband measurements discussed, all

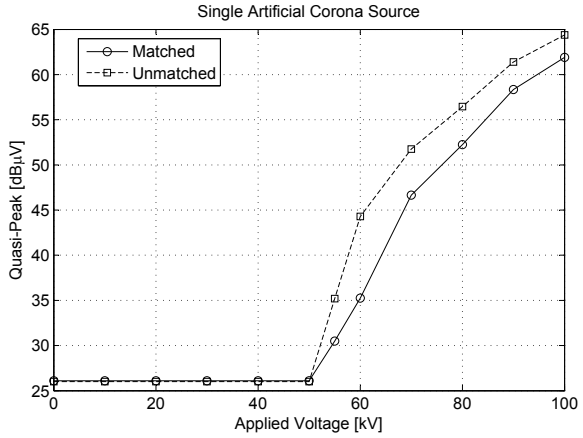

Figure 5.37: Quasi-peak measurements of single artificial corona source at various surface voltage gradients for matched and unmatched systems

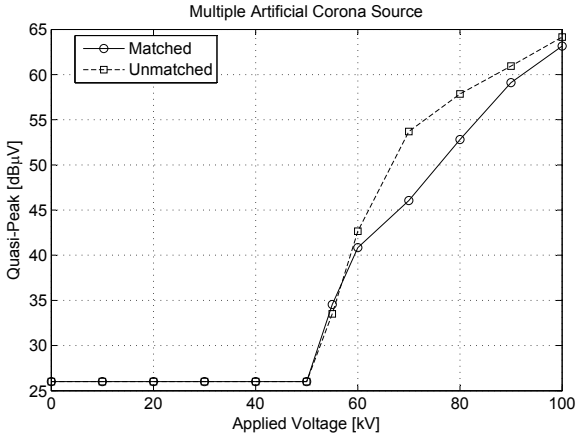

Figure 5.38: Quasi-peak measurements of multiple artificial corona sources at various surface voltage gradients for matched and unmatched systems

the frequency components are allowed through to the RN meter. Finally, a set of measurements were conducted on a single Zebra conductor in the Eskom Megawatt Park large corona cage. Frequency domain measurements were made on a matched and unmatched wideband system. The results were then compared to the frequency domain measurements on a tuned narrowband system adhering to the CISPR standard discussed in section 5.3.2.

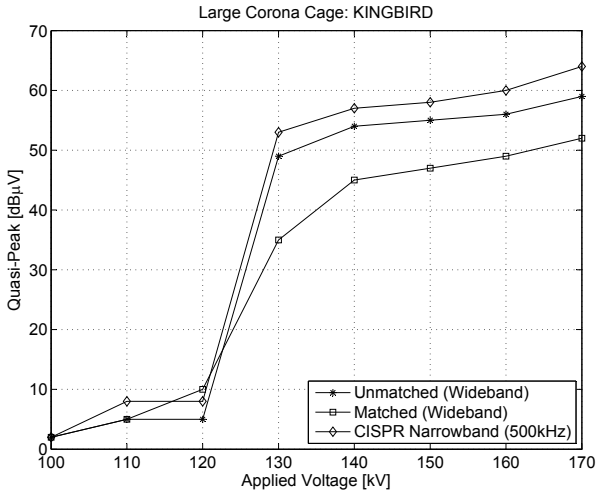

Figure 5.39: Wideband RI levels on matched and unmatched large corona cage system

It is shown in section 6.1.2 that when the necessary impedance correction factors are applied to

both wideband and narrowband measurements, the conducted RI levels should be consolidated. It is clear from figure 5.39, however, that when the necessary correction factors are applied to the present wideband and CISPR narrowband measurements, the unmatched system will deliver a much higher RI level than that of the matched system or CISPR narrowband measurement. The importance of correct impedance matching when making the wideband measurements is thus evident from the presented time and frequency domain results.

Chapter 6

RI Performance Evaluation and Excitation Functions

Various conductor corona test methods used to generate experimental data for corona performance predictions on transmission lines were considered in chapter 5. The ability to predict the radio noise (RN) performance of a transmission line is necessary to verify the reliability of the line design. Having successfully characterised the various conductor corona test methods and measurement circuits available to Eskom for monopolar corona performance evaluation, the next step is to compare these methods and derive the radio interference (RI) generation or excitation functions. The generation function results are compared to empirical RI prediction formulas derived by EPRI (*Electric Power Research Institute*), IREQ (*Hydro-Quebec Institute of Research*) and BPA (*Bonneville Power Association*). The question whether a corona cage, especially a small corona cage, can be used to accurately predict RI performance levels of DC conductors by applying methods discussed in [9] is investigated.

The measurements at the Eskom Megawatt Park corona test facility in Midrand, Johannesburg, were made possible by Mr. Riaan Roets from *Kiepersol Technologies*. Further assistance was provided by Mr. Coenie Esterhuizen and Mr. Jaco Badenhorst (*Eskom*).

6.1 RI Measurements Using Three Corona Test Methods

6.1.1 Measurement Program

Both time domain and frequency domain radio interference (RI) measurements using the small corona cage, the short test line, as well as the large outdoor corona cage are included in the measurement program in figure 6.1. The measurement circuits used to make the wideband and CISPR narrowband measurements were discussed in sections 5.3.1 and 5.3.2 respectively. The RI performance of a single *Zebra* conductor of 28.68mm diameter, as well as a single *Kingbird* conductor of 23.88mm diameter was evaluated. These measurements were all made at the Eskom Megawatt Park corona test facility in Midrand at an altitude of 1550m above sea level. Altitude tests using the two types of conductor and the small mobile corona cage at various heights above sea level are discussed in appendix E. Attention was given to correct impedance matching for wideband measurement systems.

		DC Conductor Corona Measurement Program							
		Radio Interference (RI)							
		Monopolar Zebra Conductor				Monopolar Kingbird Conductor			
		Positive Polarity (+DC)		Negative Polarity (-DC)		Positive Polarity (+DC)		Negative Polarity (-DC)	
		CSIPR FD (500kHz)	TD & FD (Wideband)	CSIPR FD (500kHz)	TD & FD (Wideband)	CISPR FD (500kHz)	TD & FD (Wideband)	CISPR FD (500kHz)	TD & FD (Wideband)
High Altitude 1550m	Small Corona Cage	✓	✓	✓	✓	✓	✓	✓	✓
	Large Corona Cage	✓	✓	✓	✓	✓	✓	✓	✓
	Test Line	✓	✓	✓	✓	✓	✓	✓	✓
	Actual Line	+DC and -DC Cahora Bassa HVDC Scheme ✘							
Variable Altitude	Small Corona Cage	✓	✓	✓	✓	✓	✓	✓	✓
Sea Level	Small Corona Cage	✓	✓	✓	✓	✓	✓	✓	✓

✓ Measurements Done
✘ Measurements Not Done
FD: Frequency Domain
TD: Time Domain

Figure 6.1: Dissertation measurement program

The capacitances and inductances per unit length of the two conductor types in the various corona test methods are presented in table 6.1, while the characteristic impedances are presented in table 6.2.

Conductor Corona Test Methods						
	Small Corona Cage		**Short Test Line**		**Large Corona Cage**	
Conductor	**C** $[pF/m]$	**L** $[nH/m]$	**C** $[pF/m]$	**L** $[\mu H/m]$	**C** $[pF/m]$	**L** $[\mu H/m]$
Zebra	14.05	792	10.06	1.11	10.11	1.10
Kingbird	13.44	828	9.75	1.14	9.79	1.14

Table 6.1: Capacitances and inductances for conductors in various corona test methods

Characteristic Impedance Z_0			
Conductor	**Small Corona Cage**	**Short Test Line**	**Large Corona Cage**
Zebra	237.4Ω	331.5Ω	329.8Ω
Kingbird	248.2Ω	342.3Ω	340.6Ω

Table 6.2: Characteristic impedances for conductors in various corona test methods

6.1.2 Frequency Domain Measurements

6.1.2.1 Small Corona Cage

The characteristic impedance for the small corona cage with a single *Zebra* conductor is $Z_0 \approx 237\Omega$. Measurements on both wideband and CISPR narrowband systems were made on the Zebra conductor in the small corona cage. The positive DC measurement results in $dB\mu V$ over the 237Ω in a wideband system are shown in figure 6.2. These were measured with the EMI receiver with centre frequency 500kHz and bandwidth 9kHz as discussed in section 5.4. The measurement circuit made use of a 500pF coupling capacitor as discussed in section 5.3. The levels include the impedance correction factors. The CISPR narrowband measurement, in $dB\mu V$ over 300Ω, as well as the wideband measurements for the Zebra conductor are compared in figure 6.4, and the correlation between them show that the correct impedance correction factors were successfully applied in both cases. The *Kingbird* conductor in the small corona cage has a characteristic impedance of $Z_0 \approx 248\Omega$. Only the CISPR narrowband measurement results, measured in $dB\mu V$ over 300Ω, are shown in figure 6.3. The 500pF coupling capacitor and 202μH tuning inductor were used in the narrowband measuring circuit for this $f_0 = 500kHz$ measurement, as discussed in section 5.3.2.

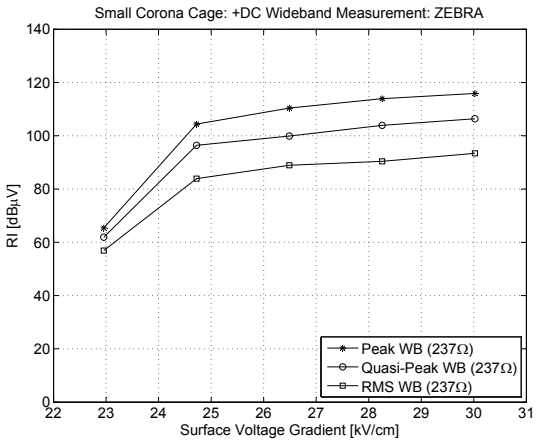

Figure 6.2: Peak, Quasi-Peak and RMS RI levels in $dB\mu V$ for a single Zebra conductor in a wideband small corona cage system

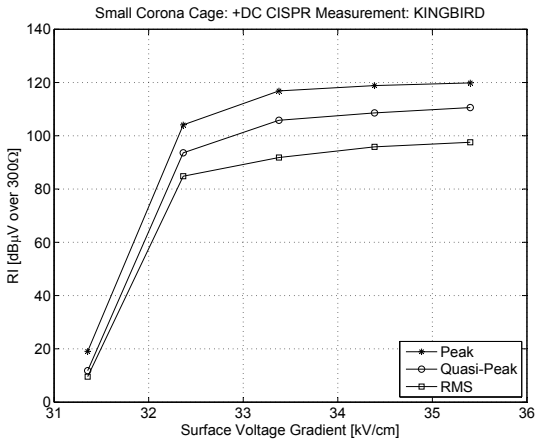

Figure 6.3: Peak, Quasi-Peak and RMS RI levels in $dB\mu V$ over 300Ω for a single Kingbird conductor in a narrowband small corona cage system

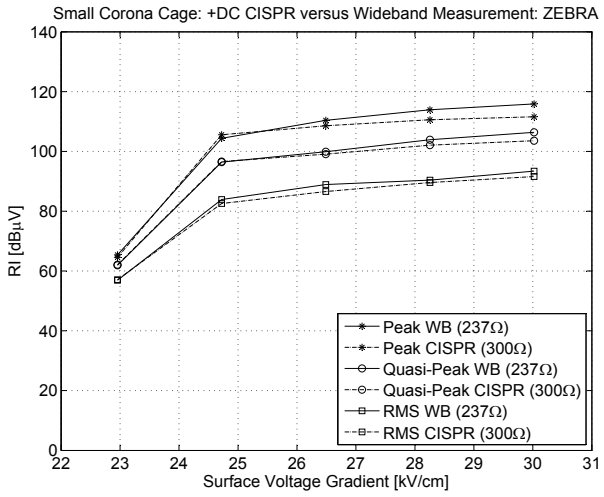

Figure 6.4: Average wideband and CISPR narrowband measurements for Zebra conductor in small corona cage

6.1.2.2 Short Test Line

The characteristic impedance for the short, 1.8m high, test line with a single *Zebra* conductor is $Z_0 \approx 330\Omega$. The positive DC measurement results over the 330Ω in a wideband system are shown in figure 6.5. Again, these were measured with the EMI receiver with centre frequency 500kHz and bandwidth 9kHz as discussed in section 5.4. The measurement circuit made use of a 368pF coupling capacitor as discussed in section 5.3. The levels include the relevant impedance correction factors. The characteristic impedance for the short test line with a single *Kingbird* conductor is $Z_0 \approx 340\Omega$. The CISPR narrowband measurement results, measured in $dB\mu V$ over 300Ω, are shown in figure 6.6.

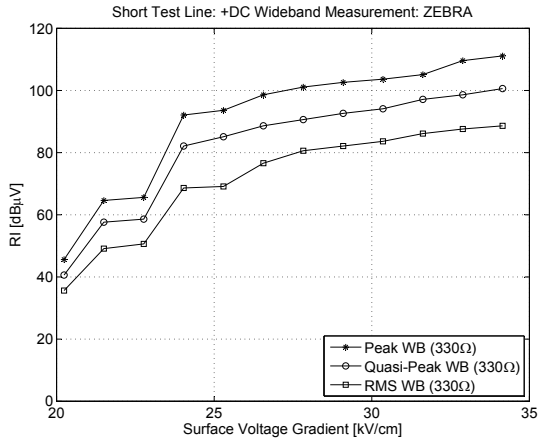

Figure 6.5: Peak, Quasi-Peak and RMS RI levels in $dB\mu V$ for a single Zebra conductor in a wideband short test line system

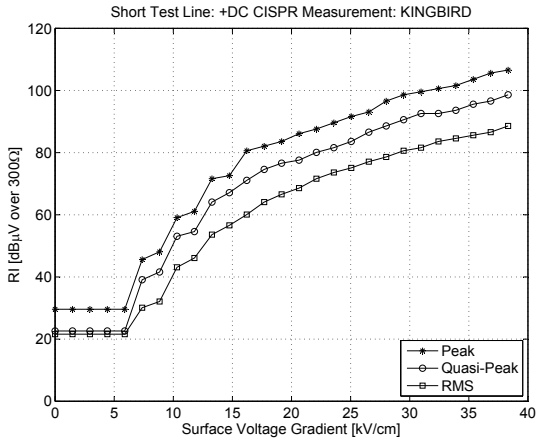

Figure 6.6: Peak, Quasi-Peak and RMS RI levels in $dB\mu V$ over 300Ω for a single Kingbird conductor in a narrowband short test line system

6.1.2.3 Large Corona Cage

The characteristic impedance for the large corona cage with a single Zebra conductor is $Z_0 \approx 330\Omega$. This is the same characteristic impedance as that of the single zebra on the short test line. The positive DC measurement results over the 330Ω in a wideband system are shown in figure 6.7. These were measured with the EMI receiver with centre frequency 500kHz and bandwidth 9kHz. The measurement circuit made use of a 368pF coupling capacitor. The levels include the impedance correction factors. The CISPR narrowband measurement results, measured in $dB\mu V$ over 300Ω, are shown in figure 6.8.

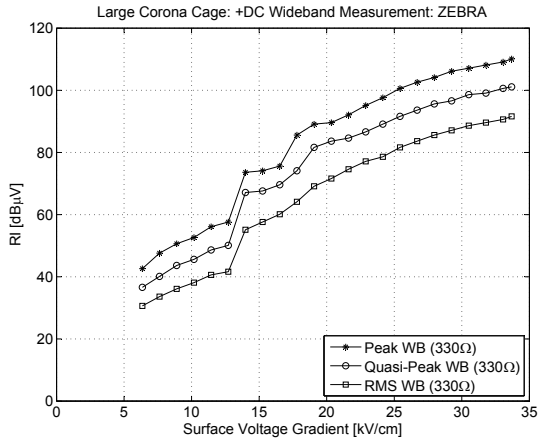

Figure 6.7: Peak, Quasi-Peak and RMS RI levels in $dB\mu V$ for a single Zebra conductor in a wideband large corona cage system

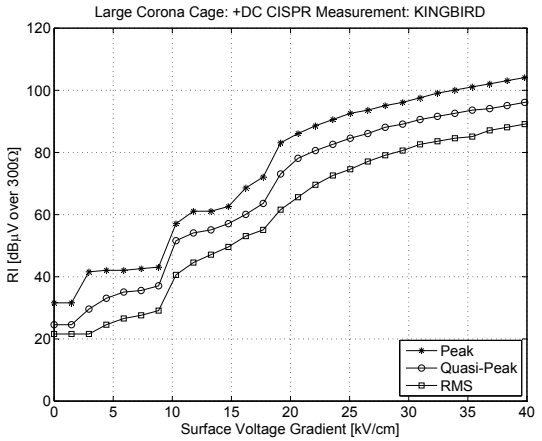

Figure 6.8: Peak, Quasi-Peak and RMS RI levels in $dB\mu V$ over 300Ω for a single Kingbird conductor in a narrowband large corona cage system

6.1.3 Conductor Corona Test Method Comparison

The peak (PK), quasi-peak (QP) and root-mean-square (RMS) wideband radio interference performance levels of the *Zebra* conductor evaluated in the three test systems are shown in figures 6.9, 6.11 and 6.13. The CISPR RI performance levels measured in $dB\mu V$ over 300Ω for the *Kingbird* conductor evaluated in the three test systems are shown in figures 6.10, 6.12 and 6.14. In order use these results to predict the RI performance on an actual line, the *excitation* or*generation* functions need to be derived and applied to the measured levels. This is done in section 6.4 where the performance predictions are also compared to empirical prediction formulas.

The frequency domain measurements on all three conductor corona test methods display the same trend: the RI levels measured in the small corona cage is noticeably higher than the the large corona cage and test line for all the detector circuits in the RN meter. This is due to the significant amount of space charge, created when the conductor voltage is raised following onset, building up in the smaller electrode arrangement of the small corona cage. There is of course the interaction of the electric field producing the ions and the distortion of the electric field caused by the created space charge [12]. The time domain measurements show a similar trend and are discussed in section 6.1.4.

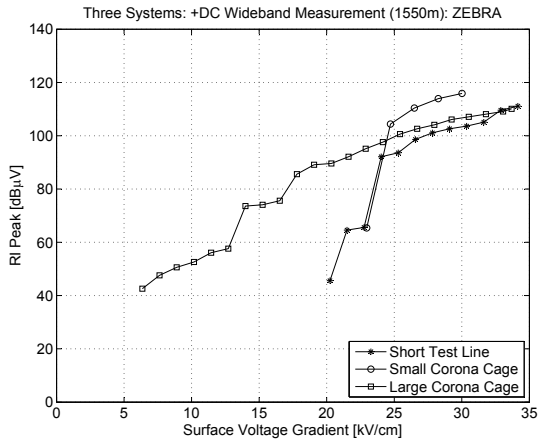

Figure 6.9: Peak RI levels in $dB\mu V$ using the three corona measurement methods to evaluate Zebra conductor

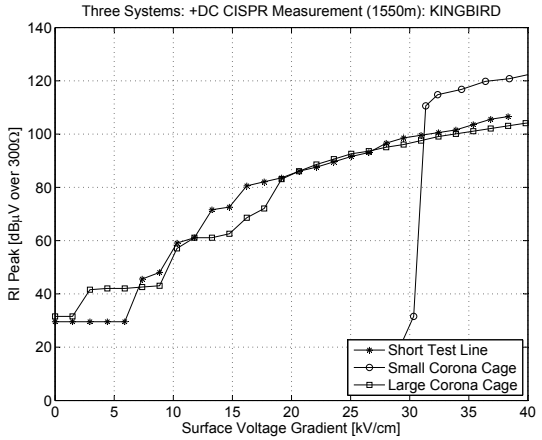

Figure 6.10: Peak RI levels in $dB\mu V$ over 300Ω using the three corona measurement methods to evaluate Kingbird conductor

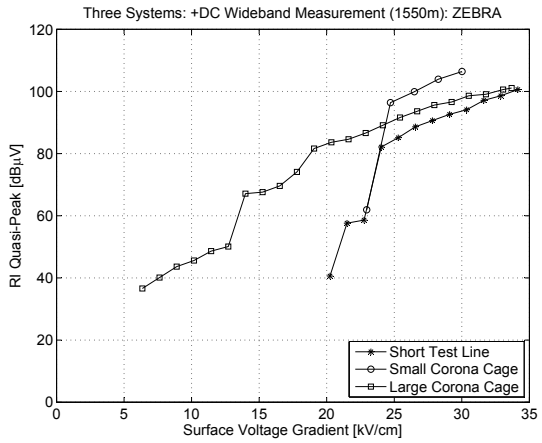

Figure 6.11: Quasi-Peak RI levels in $dB\mu V$ using the three corona measurement methods to evaluate Zebra conductor

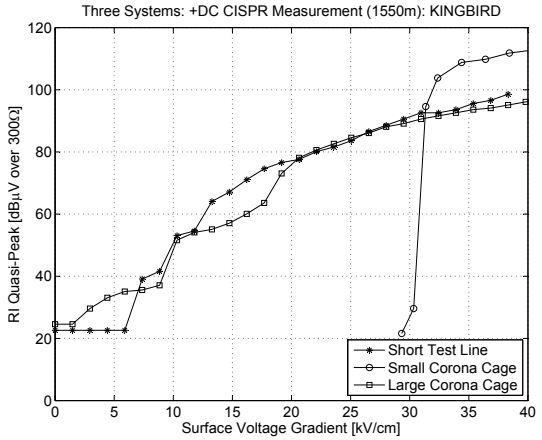

Figure 6.12: Quasi-Peak RI levels in $dB\mu V$ over 300Ω using the three corona measurement methods to evaluate Kingbird conductor

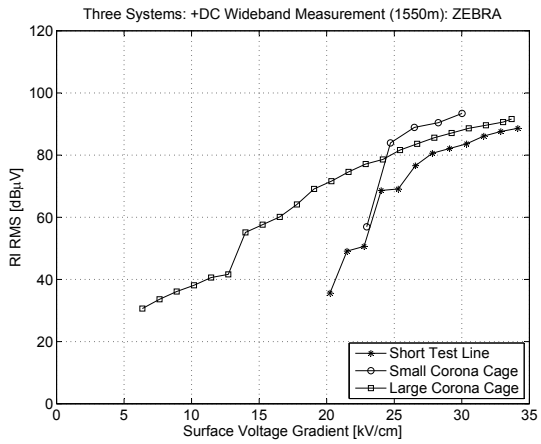

Figure 6.13: RMS RI levels in $dB\mu V$ using the three corona measurement methods to evaluate Zebra conductor

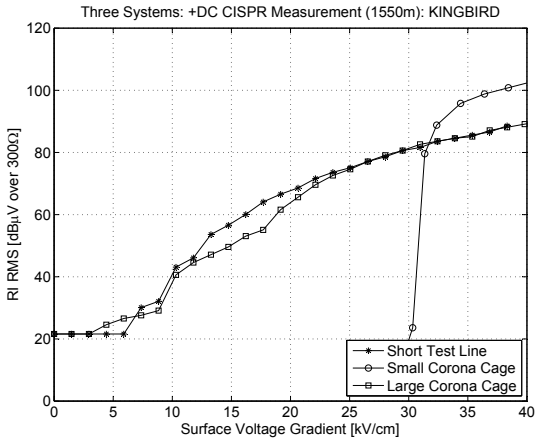

Figure 6.14: RMS RI levels in $dB\mu V$ over 300Ω using the three corona measurement methods to evaluate Kingbird conductor

6.1.4 Time Domain Parameter Extraction

Corona pulse trains were captured using a high-speed data-acquisition sampling card (*NI PCI-5124*) in order to obtain statistical distributions of the amplitudes and repetition rates (pulses per second). Examples of corona pulse trains at similar surface voltage gradients recorded on the various conductor corona test methods are shown in figures 6.15 to 6.17. The slight irregularity in the DC waveform is due to the diode ripple in the half wave rectifier DC source.

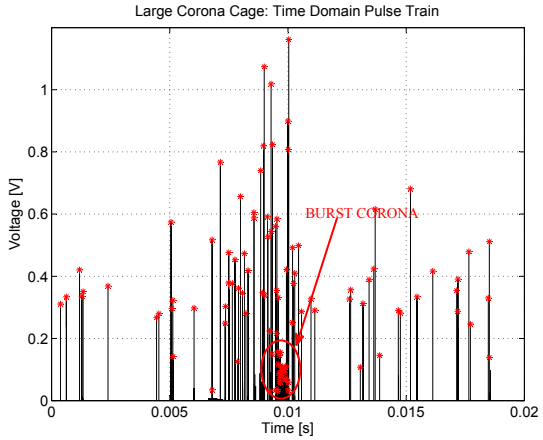

Figure 6.15: Time pulse trains recorded on large corona cage with surface voltage gradient $36kV/cm$

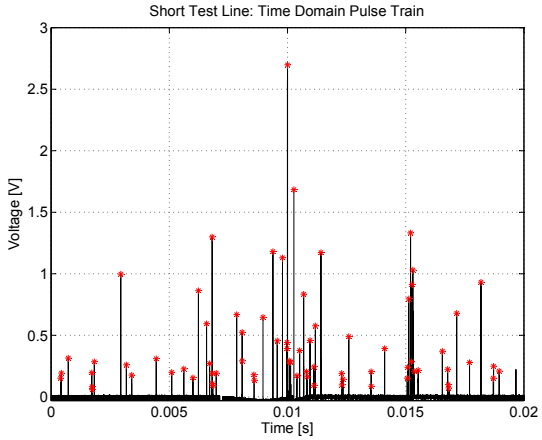

Figure 6.16: Time pulse trains recorded on short test line with surface voltage gradient $36kV/cm$

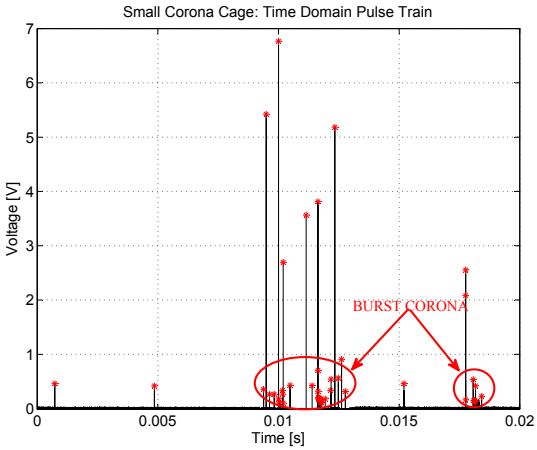

Figure 6.17: Time pulse trains recorded on small corona cage with surface voltage gradient $36kV/cm$

The average number of pulses per second recorded on the Zebra and Kingbird conductors using the various corona test methods are shown in figure 6.18 and 6.19 respectively. If the conductors of the same type are assumed to have more or less the same roughness factors and surface conditions, then the short 3.6m conductor in the small corona cage is expected to have the least number of distributed sources. The least number of pulses per second measured on both conductors are indeed in the small cage. The average number of pulses per second per metre of conductor, at the same surface voltage gradient, has the same order of magnitude. The number of pulses measured on the Zebra is much higher than the Kingbird at similar surface voltage gradients. This means that there are possibly more nucleation points and corona sources on the Zebra conductor. This is confirmed by the quasi-peak results in section 6.1.3, where a higher 500kHz RI level is measured on the Zebra conductor at much lower gradients. The average peak voltages measured in the time domain are shown in figures 6.20 and 6.21. Again, much higher amplitude levels at similar surface voltage gradients are measured on the small corona cage system using the same coupling capacitors terminated in the measurement system's characteristic impedance. Using numerical and analytical methods in section 4.2, it was shown that the space charge created during a single corona event will have between 5 and 20 times less travel-time before reaching the ground electrode in the small corona cage, than on the short test line and large corona cage respectively. As discussed previously, the space charge reaching the ground electrode will take a certain time to be cleared out of the measurement system due to the time constants determined by the capacitance, resistance and inductance of the test method. This implies that if the space charge is not cleared fast enough between corona events, the accumulated space charge from a preceding event could repel approaching ions from a following event. This could then cause space charge to accumulate and build-up

inside the electrode gap, causing a distortion of the electric field. This would also influence the conductor surface voltage gradient and inception levels. As seen from the time and frequency domain results, there was no corona below a certain level in the small cage system, and then all of a sudden a very aggressive type of discharge as the gradient was increased. The observed aggressive discharge sound in the small cage was also very different from the more uniformly distributed discharge sound in the large cage and test line for both types of conductors at similar gradients.

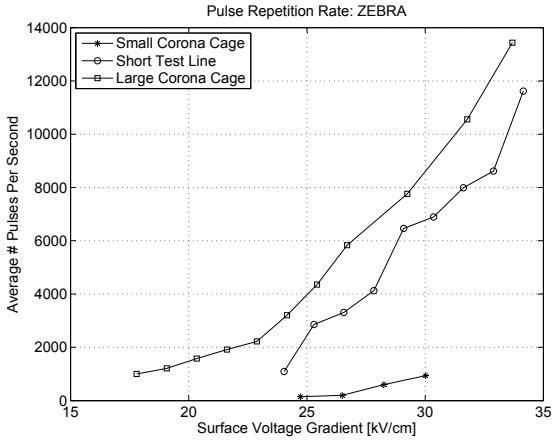

Figure 6.18: The average number of pulses per second measured in the time domain on the three systems evaluating the Zebra conductor (+DC)

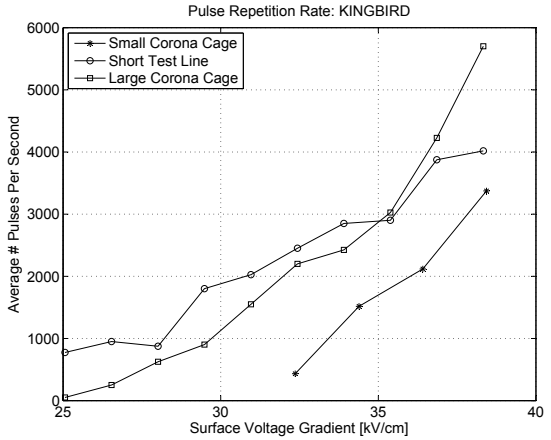

Figure 6.19: The average number of pulses per second measured in the time domain on the three systems evaluating the Kingbird conductor (+DC)

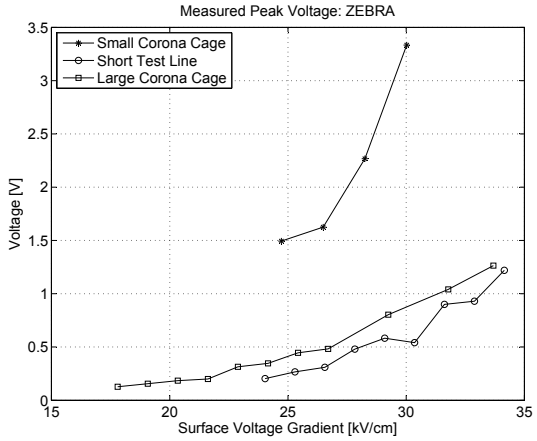

Figure 6.20: The measured peak voltage in the time domain on the three systems evaluating the Zebra conductor (+DC)

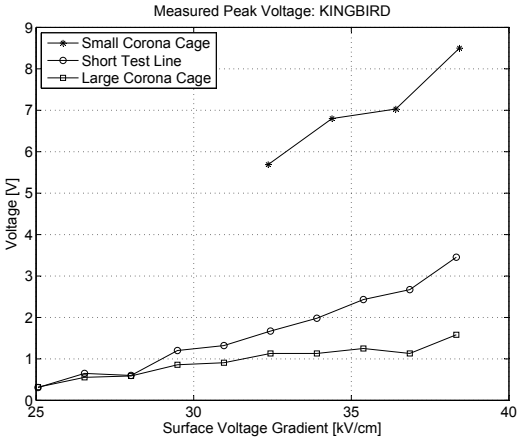

Figure 6.21: The measured peak voltage in the time domain on the three systems evaluating the Kingbird conductor (+DC)

It was found in [94] that the amplitude distribution for various electrode arrangements of positive DC corona, as the case of AC corona, is *Gaussian*. It was also found that the variation in the pulse repetition rates for DC corona near inception is *Poissonian*, while higher DC levels are also *Gaussian*. The tests performed in [94] were only up to 12.3kV and not done on actual transmission lines, but rather on point-to-plane configurations. The statistical analysis of the time domain measurements in terms of the amplitude and repetition time distributions for surface voltage gradients of $36kV/cm$ and $38kV/cm$ are shown in figures 6.22 to 6.33.

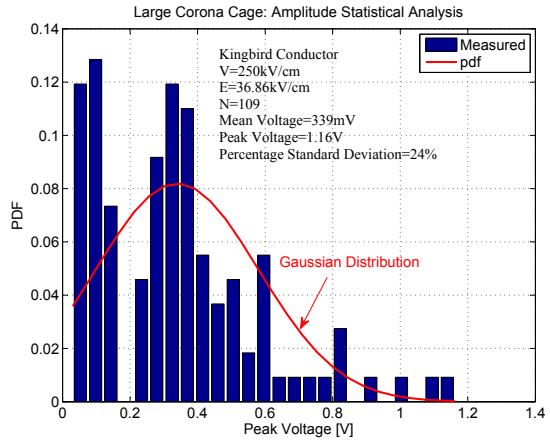

Figure 6.22: Statistical analysis of amplitude distribution for large corona cage with surface voltage gradient $E = 36.86kV/cm$

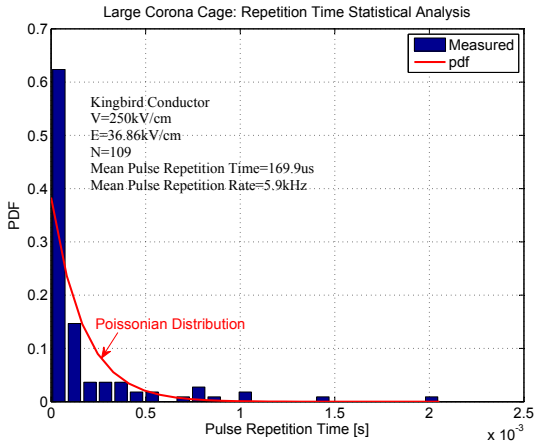

Figure 6.23: Statistical analysis of pulse repetition rate distribution for large corona cage with surface voltage gradient $E = 36.86kV/cm$

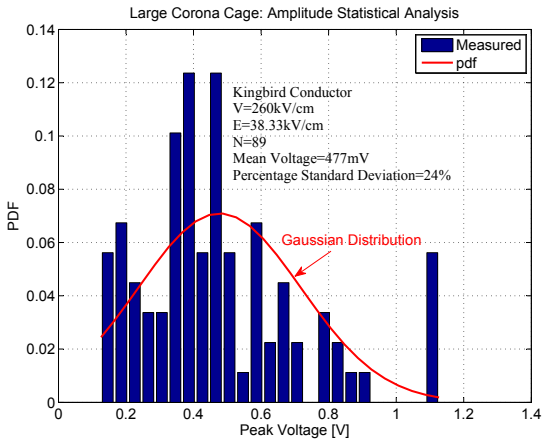

Figure 6.24: Statistical analysis of amplitude distribution for large corona cage with surface voltage gradient $E = 38.33kV/cm$

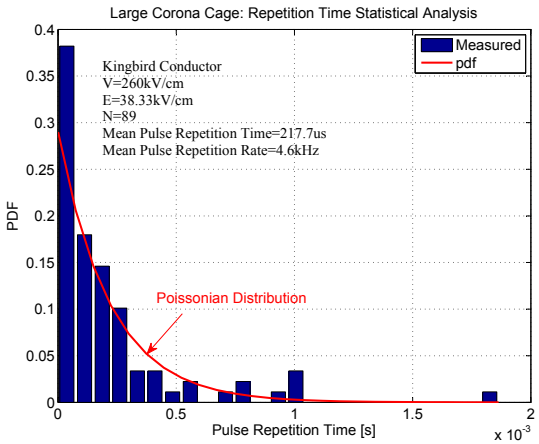

Figure 6.25: Statistical analysis of pulse repetition rate distribution for large corona cage with surface voltage gradient $E = 38.33kV/cm$

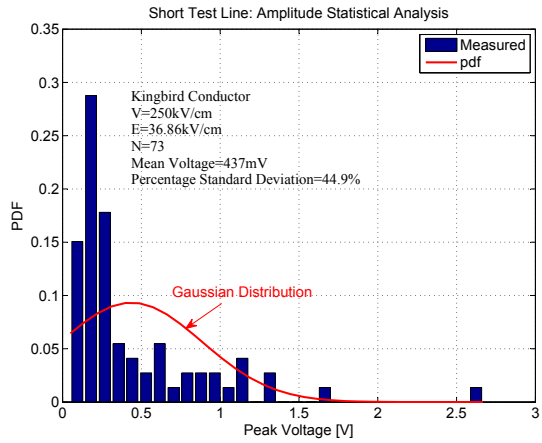

Figure 6.26: Statistical analysis of amplitude distribution for short test line with surface voltage gradient $E = 36.86kV/cm$

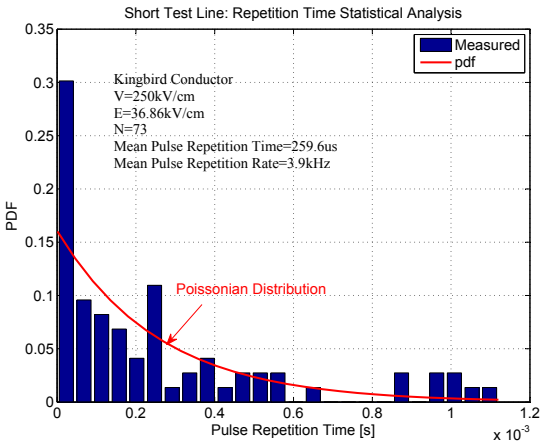

Figure 6.27: Statistical analysis of pulse repetition rate distribution for short test line with surface voltage gradient $E = 36.86kV/cm$

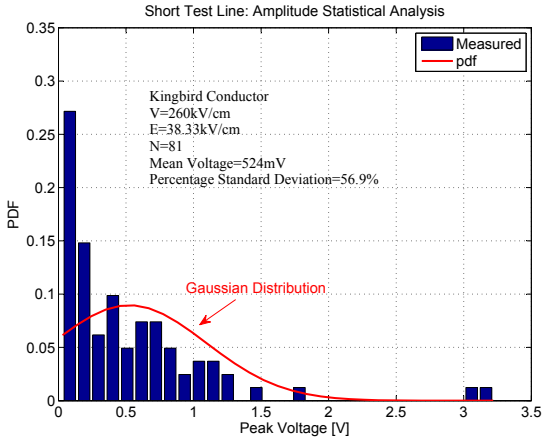

Figure 6.28: Statistical analysis of amplitude distribution for short test line with surface voltage gradient $E = 38.33kV/cm$

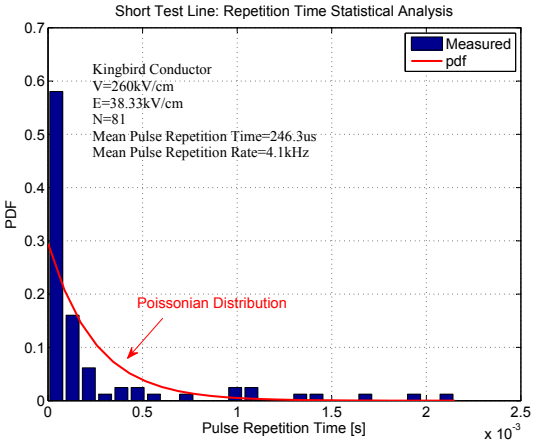

Figure 6.29: Statistical analysis of pulse repetition rate distribution for short test line with surface voltage gradient $E = 38.33kV/cm$

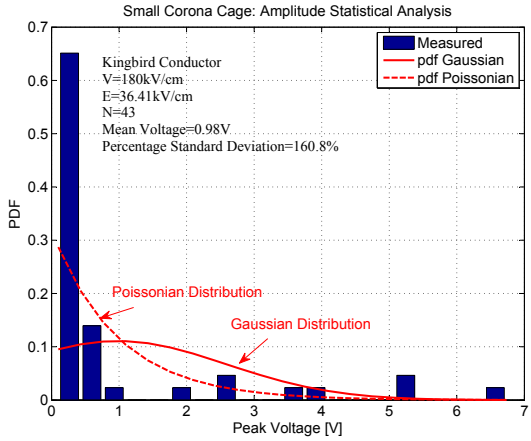

Figure 6.30: Statistical analysis of amplitude distribution for small corona cage with surface voltage gradient $E = 36.41kV/cm$

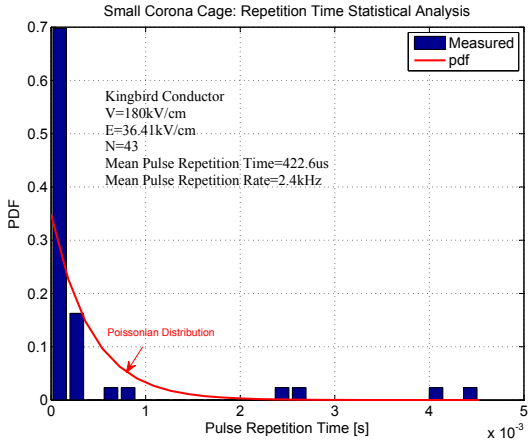

Figure 6.31: Statistical analysis of pulse repetition rate distribution for small corona cage with surface voltage gradient $E = 36.41kV/cm$

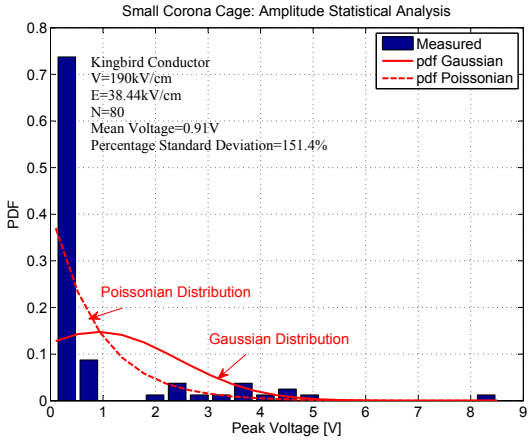

Figure 6.32: Statistical analysis of amplitude distribution for small corona cage with surface voltage gradient $E = 38.44kV/cm$

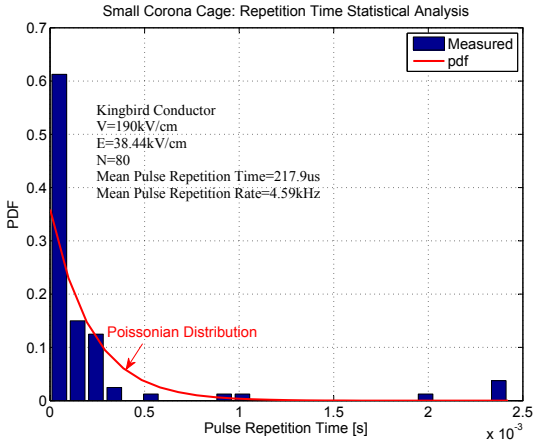

Figure 6.33: Statistical analysis of pulse repetition rate distribution for small corona cage with surface voltage gradient $E = 38.44kV/cm$

The repetition rate time distributions at these high surface gradients on all three measurement systems appear to be *Poissonian*, while the amplitude distributions on the large cage and test line are *Gaussian*. The small cage amplitude seem to fit the *Poissonian* distribution better than the *Gaussian*. This, however, is probably due to the short conductor length and few distributed corona sources. In order to get accurate statistical distributions for fair weather conditions, the chosen length of the conductor should be much longer than the measurement systems investigated in this dissertation. It is recommended in [11] and [50] that the minimum length of conductor required in a corona cage to simulate adequate fair weather corona performance, and to derive similar distributions found on actual transmission lines, is 100m. Test lines are usually between 300m and a few kilometres to observe adequate distributions.

6.1.5 Wideband Excitation

To derive a wideband excitation from the time domain measurements, the time domain data was transformed to the frequency domain using the *Fourier Transform*. The numerical relationship between the discretized transform and inverse transform pair for vectors of length N is given in [95] and [96] by equations 6.1.1 and 6.1.2.

$$X_k = \sum_{n=0}^{N-1} x_n e^{(j2\pi k/N)n} \tag{6.1.1}$$

$$x_n = \frac{1}{N} \sum_{k=0}^{N-1} X_k e^{(j2\pi n/N)k} \tag{6.1.2}$$

The transfer function of the measurement circuit, discussed in section 5.3.1, was then de-embedded from the measured data in the frequency domain. This provides the time domain pulses in a form similar to when they propogate on the conductor. It is important to remember that the wavelength, λ, of a frequency component, f, is determined by equation 6.1.3.

$$\lambda = \frac{v_c}{f} \tag{6.1.3}$$

where v_c is the propagation velocity in m/s. The 500kHz frequency component of the propogating pulse therefore has a wavelength of about 600m. This implies that the electrically short measurement system, matched in its characteristic impedance at both ends, will not appear

like a distributed element, but rather like a lumped element generating the corona pulses. The RN meter's quasi-peak detector circuit, as discussed in section 5.4, can then be applied to the propagating corona pulse trains as shown in figure 6.34.

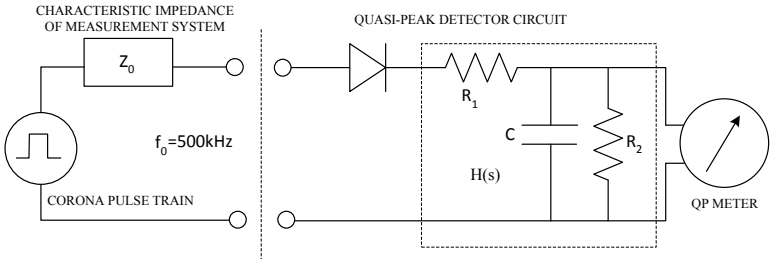

Figure 6.34: Lumped corona pulse train generator element and QP detector circuit

The dectector transfer function, $H(s)$, multiplied by the corona pulse train in the frequency domain should then yield the same results at 500kHz as the EMI receiver's QP detector during the narrowband measurements. The results of the wideband RI levels compared to the narrowband CISPR measurements for the Kingbird conductor evaluated on all three conductor corona test methods are shown in figure 6.35. The wideband and narrowband measurement results agree in the area of operational interest (E>30kV/cm). A similar trend in the small corona cage predicting a much higher RI level than the large corona cage and short test line is evident.

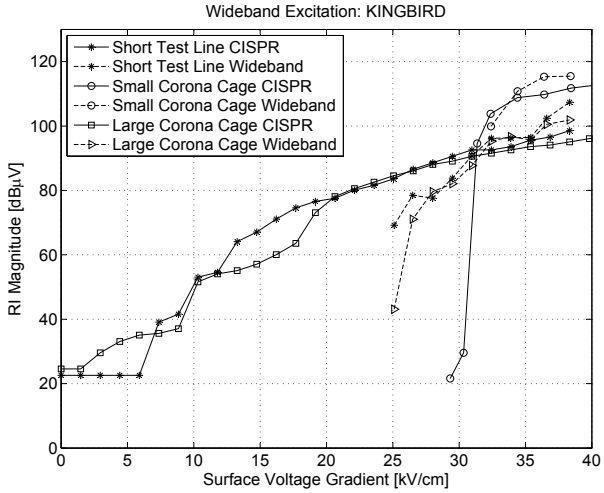

Figure 6.35: Wideband RI excitation compared to CISPR narrowband excitation

The ability to derive the monopolar RI performance excitation from wideband measurements is important, as it can now be derived for frequencies other than the 500kHz relevant to power line carrier (PLC) systems. Due to the quasi-peak detector in CISPR EMI receivers being centred around 500kHz, and only frequency domain methods applied to RI excitation measurements, this was not possible before. The variation of the RN with frequency can also be investigated.

6.2 Excitation Function Theory

The corona streamer is the source for RI and is usually represented as a current source or generator into the conductor. The ideal current source will inject current into a single conductor that depends only on the characteristics of the streamer [97]. It was however shown in [98] that the corona streamer will induce currents into all conductors in a multi-conductor bundle, and not only the conductor that formed the streamer. The current source is therefore a combination of the corona streamer characteristic, as well as the characteristic of the conductor under corona and the self and mutual capacitances of each conductor in the bundle. The *excitation* or *generation* function for a single conductor above a ground plane is defined in [97] as

$$i = \frac{C}{2\pi\epsilon_0}\Gamma \tag{6.2.1}$$

with Γ being the *excitation function* measured in dB over $\mu\text{A}/\sqrt{m}$, C is the capacitance of the conductor bundle in the measurement system in F/m, i is the measured RI current in $\text{dB}\mu\text{A}/\sqrt{m}$ and $\epsilon_0 = 8.854 \times 10^{-12}\text{F/m}$ [92].

6.2.1 Demonstration by Means of the Potential Function

Consider the coaxial or cylindrical conductor arrangement similar to a corona cage of radius R and conductor radius r both at zero potential [97]. Now suppose an infinitely thin cylinder of space charge density q_0 per unit length is placed within this coaxial element at radius ρ as in figure 6.36. The presence of q_0 will induce a charge q onto the grounded centre conductor. The electrostatic field at a point x is given by *Gauss's* law in equation 6.2.2.

$$E(x) = \begin{cases} \frac{q}{2\pi\epsilon_0}\frac{1}{x} & \text{if } r < x < \rho \\ \frac{q+q_0}{2\pi\epsilon_0}\frac{1}{x} & \text{if } \rho < x < R \end{cases} \tag{6.2.2}$$

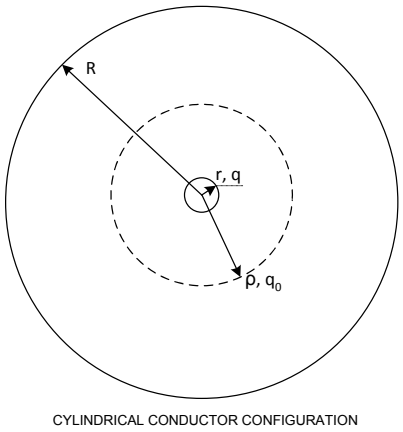

Figure 6.36: A coaxial element with space charge density q_0 at radius ρ

The potential difference is found by integrating from r to R as in equation 6.2.3.

$$V_r - V_R = \int_r^\rho E(x)dx + \int_\rho^R E(x)dx = \frac{1}{2\pi\epsilon_0}[q\ln(\frac{R}{r}) + q_0\ln(\frac{R}{\rho})] \tag{6.2.3}$$

Seeing that both the conductor and corona sheath is at zero potential, the charge per unit length induced on the centre conductor is given by

$$q = -q_0 \cdot \frac{\ln(\frac{R}{\rho})}{\ln(\frac{R}{r})} \tag{6.2.4}$$

When the space charge q_0 expands at a velocity $d\rho/dt$, the injected current is given by the rate of the induced charge dq/dt. This current is given by equation 6.2.5.

$$i = \frac{dq}{dt} = \frac{dq}{d\rho} \times \frac{d\rho}{dt} = \frac{1}{\ln(\frac{R}{r})} \cdot \frac{q_0}{\rho} \times \frac{d\rho}{dt} \tag{6.2.5}$$

The capacitance per unit length of the coaxial configuration is given by equation 6.2.6.

$$C = \frac{2\pi\epsilon_0}{\ln(\frac{R}{r})} \tag{6.2.6}$$

Therefore, substituting for $\frac{1}{\ln(R/r)} = \frac{C}{2\pi\epsilon_0}$ in equation 6.2.5, the injected current is given by equation 6.2.7.

$$i = \frac{C}{2\pi\epsilon_0} \times \frac{q_0}{\rho} \cdot \frac{d\rho}{dt} \tag{6.2.7}$$

The injected current is the product of two components that depends on: 1) the electrode geometry, and 2) the characteristics of the space charge, its quantity and its law of movement. The excitation function quantity due to the space charge movement was defined in [97] as in equation 6.2.8.

$$\Gamma = \frac{q_0}{\rho} \cdot \frac{d\rho}{dt} \tag{6.2.8}$$

6.2.2 Excitation Function: Corona Cages

The derivation of the generation function of a corona cage with outer sheath radius R, conductor radius r and length L is considered next. The quasi-peak value, measured with the CISPR narrowband measurement in $dB\mu V$ discussed in section 5.3.2, is used to derive the necessary excitation function. The current term i in the excitation function, as per equation 6.2.1, can therefore be expressed in terms of the measured quasi-peak voltage, V_m, and the measurement resistance R_m as shown in figure 5.20.

$$i_{\mu A/\sqrt{m}} = \frac{10^{V_m/20}}{R_m \cdot \sqrt{L}} \tag{6.2.9}$$

The capacitance of the corona cage is given by equation 5.5.3 as $C = \frac{2\pi\epsilon_0}{\ln(\frac{R}{r})}$. This implies that the generation function Γ, measured in dB over $1\mu A/\sqrt{m}$, is given by

$$\Gamma = 20\log(\frac{10^{V_m/20} \cdot \ln(\frac{R}{r})}{R_m\sqrt{L}}) \tag{6.2.10}$$

The expression for the generation function of a large corona cage is therefore given by equation 6.2.11.

$$\Gamma_{[dB\mu A/\sqrt{m}]} = V_m - 20\log(R_m) + 20\log(\ln(\frac{R}{r_{eq}})) - 20\log(\sqrt{L}) \tag{6.2.11}$$

The term r_{eq} is the equivalent radius of a bundled conductor with n sub-conductors of radius r, and a bundle radius of R given by equation 6.2.12.

$$r_{eq} = [n \cdot r \cdot (R)^{n-1}]^{\frac{1}{n}} \tag{6.2.12}$$

For simplicity, let the terms in equation 6.2.11 be expressed in the form

$$\Gamma_{[dB\mu A/\sqrt{m}]} = V_m + A + B + C \tag{6.2.13}$$

where $A = -20\log(R_m)$; $B = +20\log(\ln(\frac{R}{r_{eq}}))$ and $C = -20\log(\sqrt{L})$. The large and small corona cages with CISPR narrowbands measuring circuits used during the evaluation of the Zebra and Kingbird conductors in this dissertation then produce the generation functions Γ_{LC} and Γ_{SC} respectively, as shown in table 6.3.

Corona Cage Excitation Functions								
	Large Corona Cage				**Small Corona Cage**			
Conductor	**A [dB]**	**B [dB]**	**C [dB]**	Γ_{LC} $[dB\mu A/\sqrt{m}]$	**A [dB]**	**B [dB]**	**C [dB]**	Γ_{SC} $[dB\mu A/\sqrt{m}]$
Zebra	27.96	14.81	16.02	$V_m - 29.17dB$	27.96	11.95	5.56	$V_m - 21.57dB$
Kingbird	27.96	15.09	16.02	$V_m - 28.89dB$	27.96	12.34	5.56	$V_m - 21.1dB$

Table 6.3: Corona cage excitation functions

6.2.3 Excitation Function: Test Line

Similar techniques, as discussed in section 6.2.2, can be used to derive the excitation function for a short test line of height H, length L and conductor radius r. The capacitance of the test line is given by equation 6.2.14 as

$$C = \frac{2\pi\epsilon_0}{\ln(\frac{2H}{r})} \tag{6.2.14}$$

The derived generation function for the test line is given by equation 6.2.15.

$$\Gamma_{[dB\mu A/\sqrt{m}]} = V_m - 20\log(R_m) + 20\log(\ln(\frac{2H}{r_{eq}})) - 20\log(\sqrt{L}) \tag{6.2.15}$$

Again, for simplicity, let the terms in equation 6.2.15 be expressed in the form similar to equation 6.2.13 where $A = -20\log(R_m)$; $B = +20\log(\ln(\frac{2H}{r_{eq}}))$ and $C = -20\log(\sqrt{L})$. The short test line with CISPR measurement circuits used during the evaluation of the Zebra and Kingbird conductors in this dissertation then produce the generation function Γ_{TL} as shown in table 6.4.

Test Line Excitation Functions				
Conductor	**A [dB]**	**B [dB]**	**C [dB]**	Γ_{TL} $[dB\mu A/\sqrt{m}]$
Zebra	27.96	14.85	12.79	$V_m - 25.9dB$
Kingbird	27.96	15.13	12.79	$V_m - 25.62dB$

Table 6.4: Corona cage excitation functions

6.3 RI Excitation Functions and Empirical Predictions

Various corona generated radio interference (RI), television interference (TVI) and electromagnetic interference (EMI) prediction formulas for AC and DC high voltage transmission lines were presented in [99]. The experimental data available for the derivation of empirical formulas for all the corona effects from HVDC lines are much more limited than that of HVAC lines [11]. The general form for comparing measured and predicted (calculated) RI levels generated by corona is given in by 6.3.1

$$RI = RI_0 + RI_g + RI_d + RI_D \tag{6.3.1}$$

where RI is the value in dB above $1\mu V$ calculated for a new transmission line and RI_0 is the reference value for a line configuration. The remaining terms are adjustment factors for conductor surface gradient g, conductor diameter d and lateral distance D from a conductor bundle being considered [11]. Other terms that might be added to equation 6.3.1 is the number of sub-conductors, measuring frequency, altitude above sea level and weather conditions. Different empirical formulas exist for radiated and conducted RI levels generated by corona.

6.3.1 Radiated Radio Interference

RI is caused by the movement of ion space charge created during the corona streamer discharge process [97]. The early experimental studies of [100] found the variation of RI in dB above 1μV/m with respect to the radial distance D in m between the conductor and meter antenna, as well as the measuring frequency f in MHz is given by

$$RI = RI_0 - 29.4log\frac{D}{D_0} - 20log\frac{1+f^2}{1+f_0^2} \tag{6.3.2}$$

where RI_0, D_0 and f_0 are reference values. Further work in [101] on the measurement of an experimental line in Sweden led to the derivation of the following empirical formula

$$RI = 25 + 10log(n) + 20log(r) + 1.5(g - g_0) - 40log\frac{D}{D_0} \tag{6.3.3}$$

where n is the number of sub-conductors in the bundle, r is the sub-conductor radius in cm, g is the maximum bundle gradient in kV/cm and D is the radial distance in m from the the positive conductor to the measuring point. The reference values $D_0 = 30m$ and $g_0 = 22\delta$, where δ is the relative air density (RAD) given by equation 2.1.2.

6.3.2 Conducted Radio Interference

RI tests were conducted by EPRI in the United States [48]. Their results showed that the RI level in dB tends to be linear with line voltage. They also found that there was some roll off in the linearity at higher voltages. They assumed this was due to saturation effects [102]. An empirical formula was developed from this test program to calculate the *monopolar* RI for voltages up to ±400kV. This empirical formula is given in equation 6.3.4

$$RI = 214\log(\frac{g_{max}}{14}) - 278[\log(\frac{g_{max}}{14})]^2 + 40\log(r) \tag{6.3.4}$$

where g_{max} is the maximum surface voltage gradient and r is the radius of one conductor. A study was done by BPA where a formula to predict the average fair weather RI levels, measured with a CISPR QP detector, for a *bipolar* DC line was developed [103]. The BPA formula is given by equation 6.3.5.

$$RI = 51.7 + 86\log(\frac{g}{g_0}) + 40\log(\frac{d}{d_0}) \tag{6.3.5}$$

where g is the maximum surface voltage gradient in kV/cm and d is the conductor diameter in cm. Another study was done by IREQ for *monopolar* schemes in [85] and *bipolar* schemes with voltages between ±600kV and ±1200kV in [104]. This empirical RI excitation functions were developed for different seasons of the year, as well as fair and foul weather conditions. The empirical prediction formula is given by equation 6.3.6.

$$\Gamma = \Gamma_0 + k_1 \cdot (g - g_0) + k_2 \cdot \log(\frac{n}{n_0}) + k_3 \cdot \log(\frac{d}{d_0}) \tag{6.3.6}$$

where Γ is the RI excitation function in dB above $1\mu A/\sqrt{m}$, g is the maximum surface voltage gradient in kV/cm, n is the number of sub-conductors in the bundle and d is the sub-conductor diameter in cm; k_1, k_2 and k_3 are empirical constants and Γ_0, g_0 and d_0 are reference values. The bipolar values for k_1, k_2 and Γ_0 for different seasons and fair and foul weather conditions are given in table 6.5 for reference values of $n_0 = 6$, $d_0 = 4.064cm$ and $g_0 = 25kV/cm$, while $k_3 = 40$.

Bipolar Empirical Parameters				
Season	**Weather**	Γ_0	k_1	k_2
Summer	Fair	27.0	1.83	45.8
	Foul	20.4	1.39	48.0
Fall/Spring	Fair	23.4	1.68	29.0
	Foul	19.8	1.68	63.5
Winter	Fair	18.7	1.63	19.7
	Foul	19.5	1.47	10.0

Table 6.5: Parameters defining the IREQ bipolar empirical formula [11]

More work by IREQ regarding bipolar schemes were done when they considered the long term statistical study of corona electric field and ion-current performance of ± 900kV bipolar HVDC transmission lines in [105]. For the case of *monopolar* DC, the parameters defining the excitation function developed by IREQ in [85] is given in table 6.6. The empirical constant k_3 could not be defined in this study as only one single conductor was used as a reference. The IREQ results furthermore suggest that the RI levels during average rain conditions are 3dB less than during

fair weather conditions. The RI levels under heavy rain conditions can be up to 6dB less.

Monopolar Empirical Parameters				
Polarity	**Weather**	Γ_0	k_1	k_2
+DC	Fair	33.29	2.28	-11.47
	Foul	31.7	1.69	-7.33
-DC	Fair	6.28	0.23	3.05
	Foul	6.3	0.46	-6.05

Table 6.6: Parameters defining the IREQ monopolar empirical formula [85]

6.4 Excitation Function Results

The excitation functions derived in equations 6.2.11 and 6.2.15 for the corona cages and short test line respectively are now applied to the quasi-peak measurements in section 6.1.2. These generation functions, measured in dB over $1\mu\text{A}/\sqrt{m}$, are then compared to the monopolar *EPRI* RI prediction formula in equation 6.3.4, the *IREQ* monopolar RI prediction formula in equation 6.3.6, as well as the *BPA* bipolar RI prediction formula in equation 6.3.5. The results are shown for the Zebra and Kingbird conductors in figures 6.37 and 6.38 respectively. The empirical constant k_3 in the IREQ prediction was chosen as $k_3 = 20$ for the Zebra conductor and $k_3 = 30$ for the Kingbird conductor predictions.

In the case of both conductors, the large corona cage and short test line deliver similar RI performance predictions. These furthermore correlate well with the EPRI prediction formula for monopolar DC conductors up to ±400kV. The results for the positive fair weather monopolar RI excitation functions correspond well to work done in [85]. Similar performance trends are observed in that the small corona cage RI levels are a lot higher than that of the large corona cage, short test line or prediction formulas.

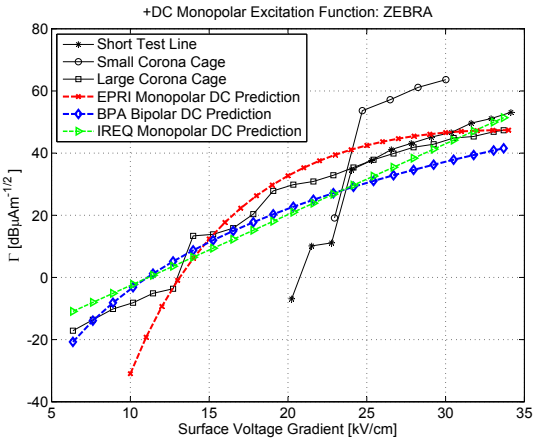

Figure 6.37: Zebra excitation functions of three corona test methods compared to empirical predictions

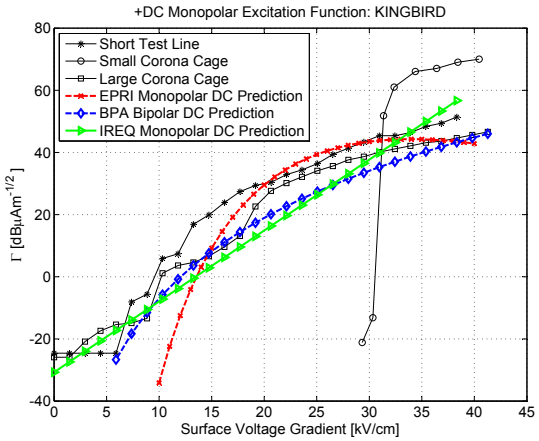

Figure 6.38: Kingbird excitation functions of three corona test methods compared to empirical predictions

6.4.1 Possible Altitude Correction

The measurements made on the various conductor corona test methods were done at a high altitude of 1550m above sea level. It is however not clear if altitude correction factors have necessarily been taken into account during the derivation of the EPRI, IREQ and BPA prediction formulas. The correction factor will be due to the difference in height between the Eskom Megawatt Park facility and the EPRI, IREQ and BPA facilities. If it is assumed that the EPRI High Voltage Test Facility is situated at a height of between 300 and 400m above sea level, while the BPA and IREQ High Voltage Test Facilities are situated between 0 and 100m above sea level, the altitude correction factors in table 6.7, as per equation 2.7.1, need to be applied to the predictions. The altitude corrected results are shown in figures 6.39 and 6.40.

Altitude Correction Factors		
Test Site	**Altitude**	**Correction Factor**
EPRI	300 to 400m	3.5dB
BPA	0 to 100m	4.5dB
IREQ	0 to 100m	4.5dB

Table 6.7: Altitude correction factors assumed for various prediction formulas

The large corona cage and short test line excitation functions still agree well with the EPRI and IREQ empirical RI prediction formulas as discussed before. This is especially the case

for the surface voltage gradient levels where transmission lines can be expected to operate (>30kV/cm).

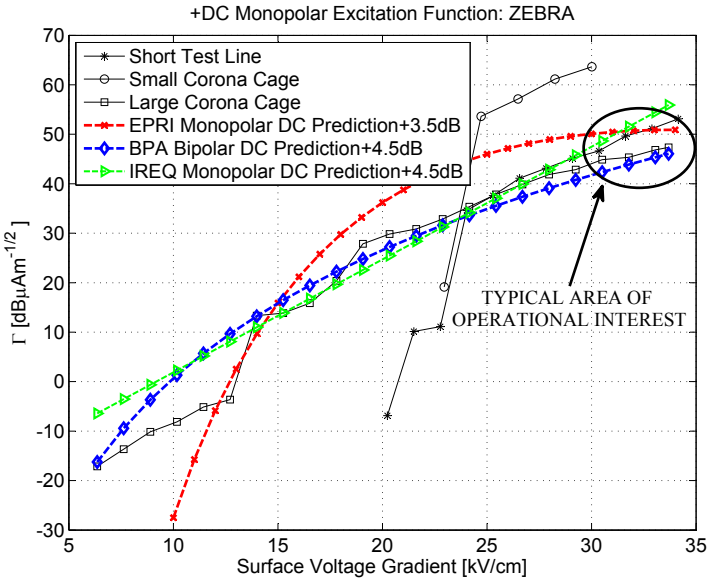

Figure 6.39: Zebra excitation functions of three corona test methods compared to empirical predictions with altitude correction factor

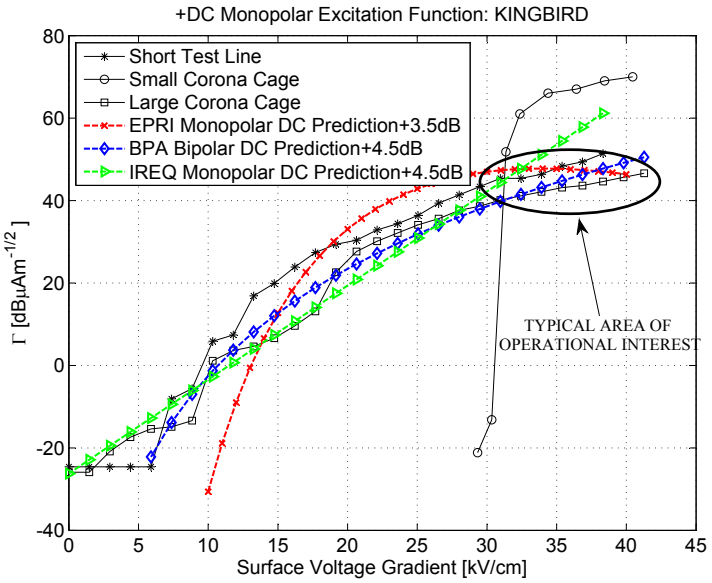

Figure 6.40: Kingbird excitation functions of three corona test methods compared to empirical predictions with altitude correction factor

Chapter 7

Conclusions and Recommendations for Future Work

In general, conductor corona test methods are used not only to study the corona physics, but also to generate experimental data to be used in the excitation functions to predict the corona performance on transmission lines. The ability to predict radio noise (RN) performance of a transmission line is necessary to verify the reliability of the line design. The RN prediction for communication system design is also of particular importance. The power line carrier (PLC) system needs to transmit the carrier signal successfully in that frequency band between various teleprotection devices on the Cahora Bassa high voltage direct current (HVDC) scheme. It is well known that conductor corona test methods, such as corona cages and test lines, can be used to evaluate the corona performance of conductors used on high voltage alternating current (HVAC) transmission schemes. The main difference between HVDC and HVAC schemes, however, is the continuous formation and build-up of space charge due to the electrostatic field of the former. The possibility of using the same conductor test methods to predict the corona performance of HVDC conductors was investigated in this disseration.

To draw accurate conclusions regarding a specific conductor corona test method, the underlying corona and space charge processes had to be understood. A comprehensive physics background to direct current (DC) corona and space charge effects was presented. This included the various primary and secondary ionization, attachment and photoionization gas discharge processes. These processes give rise to electron avalanches and breakdown mechanisms that lead to corona partial discharges. Both positive and negative polarity DC corona were investigated in the time and frequency domain. The effect of the corona-generated space charge on the electrical envi-

ronment around the conductor, as well as the influence of altitude, air pressure, humidity and temperature on the RI levels were discussed. A particle-in-cell (PIC) computational code was developed to aid in the visualisation of the processes that give rise to corona partial discharges. Higher order basis functions were implemented in the finite element method used to solve the Poisson field equation. First order linear triangular elements use linear interpolation functions to solve for the potentials at the grid points. This implies that the electric field, which is the negative gradient of the potential, is constant in an element. By using second order quadratic interpolation functions, a linear electric field interpolation is obtained in an element. This results in a higher level of accuracy for the space charge field solution. The computational tool, together with a designed and developed electrometer-type circuit, provided a better understanding of the particle dynamics and spatial-temporal development of space charge created during corona events.

Conducted RI corona performance of a single Zebra and Kingbird conductor was evaluated using three conductor corona test methods available to Eskom. These include the Eskom Megawatt Park large outdoor corona cage, a short test line and a small corona cage at high altitude. The measurement systems and background environment were critically evaluated, and the transfer functions and earthing structures were characterised. It was shown that the outer structure of the large outdoor corona cage at the Eskom Megawatt Park corona test facility provides excellent shielding against background RN coupling. Time domain reflectometry techniques showed a change in effective characteristic impedance experienced by pulses propagating outside the guard rings on the large cage. This is the first time that the large corona cage system and measurement circuits at these local high voltage test facilities were investigated in such detail.

The CISPR narrowband measurements were made in accordance to relevant CISPR standards for radio noise measurements of high voltage transmission lines. This typically includes a measuring circuit consisting of a tuned series coupling capacitor and inductor terminated into 300Ω. The narrowband measurements are made with an EMI receiver's quasi-peak (QP) detector circuit. The receiver has a pre-selection filter centred at 500kHz with a 9kHz bandwidth. Both narrowband and wideband measurement circuits were characterised, and the necessary impedance correction factors were calculated successfully. The conducted RI performance results of both the Zebra and Kingbird displayed similar trends on all three measurement systems. The small corona cage measured a much higher dBμV over 300Ω RI level, per surface voltage

gradient, than the large corona cage and short test line.

The importance of correct impedance matching during wideband measurements is discussed in detail. Time domain and frequency domain measurements were made using matched wideband measurement systems, and the results obtained correlate with the measurements on the narrowband system after applying the necessary impedance correction factors. Wideband time domain measurements were made with a high-speed data-acquisition sampling card to obtain a high enough resolution to analyse the amplitude and repetition rate time distributions statistically. To obtain adequate statistical distributions for fair weather corona performance, however, longer line lengths than those investigated in this dissertation are suggested. In the time domain, a similar trend was again observed to that of the wideband and narrowband frequency domain results. The amplitude levels measured in the small corona cage are much higher than the large cage and test line systems.

Excitation functions were derived for the various conductor corona test methods for both the wideband time domain and narrowband frequency domain measurements. The wideband excitation functions were derived by de-embedding the measurement circuit transfer function from the measured time pulse trains, and applying the quasi-peak detector transfer function. The wideband time domain results correlate with the narrowband frequency domain results at 500kHz. The ability to derive the monopolar RI performance excitation from wideband measurements is important, as it implies that it can be derived for frequencies other than the 500kHz relevant to power line carrier (PLC) system. Due to the quasi-peak detector in CISPR EMI receivers being centred around 500kHz, and only frequency domain methods applied to RI excitation measurements, this was not possible before. The variation of the RN with frequency can also be investigated. The excitation functions are compared to empirical prediction formulas derived by EPRI, IREQ and BPA. The derived excitation functions correlate with the prediction formulas within a few dB in the operational range higher than 30kV/cm. The results still agree after altitude correction factors are applied to the empirical predictions. Again, similar performance trends are observed in that the small corona cage RI levels are a lot higher than that of the large corona cage, short test line and prediction formulas.

Using numerical and analytical methods it was shown that the space charge created during a single corona event will have between 5 and 20 times less travel-time before reaching the ground electrode in the small corona cage, than on the short test line and large corona cage

respectively. The space charge reaching the ground electrode will take a certain time to be cleared out of the measurement system due to the time constants defined by the capacitance, resistance and inductance. If the space charge is not cleared fast enough between corona events, the accumulated space charge from a preceding event will repel approaching ions from a following event. This will then cause space charge to build up inside the electrode gap, causing a distortion of the electric field. The conductor surface voltage gradient and inception levels will also be influenced. As a consequence of the physics, computational modelling and both frequency and time domain measurements, the small corona cage was found incapable of predicting the RI performance of a transmission line accurately. This is due to the space charge accumulation in the small electrode gap.

It is important to be able to compare the RI corona performance in a conductor corona test method to that of an actual line. This can be done, for example, with a quad-Zambezi conductor bundle similar to that of the Cahora Bassa HVDC scheme, in a large corona cage or a scaled test line model with a few span lengths. To achieve similar operational surface voltage gradients, a DC source larger than the one available for the research in this dissertation would be needed. As soon as a large enough source becomes available, this should become a research topic to consider. Other future work may include the effect of altitude on RI and CL levels during light and heavy rain conditions. These tests will be especially valuable for the CL component which is worse under heavy rain conditions.

The research leading up to the culmination of this dissertation has relied on experiments which involve large systems such as the Eskom Megawatt Park outdoor corona cage. These facilities are not available permanently. Many findings of the work have been published in conference papers and technical reports such as [2], [20], [81], [102] and [106]. However, the final and most important experiments could only be formulated once all the major features of the experiments had been fully understood. This forms the pinnacle of the research and was only completed within the last period of the doctoral work. As a consequence, the major work is yet to published in a peer-reviewed journal. This submission is in preparation.

Bibliography

[1] E. F. Raynham, *Apollo-Cahora Bassa Enigma and Diversions*, C. Yelland, Ed. EE Publishers (Pty) Ltd., 2004. ix, 5, 6

[2] A. J. Otto and S. Miya, "The differences of electric field strengths and ionic currents under HVDC lines of negative and positive polarity," RES/SC/08/30170, Eskom Sustainability and Innovation, Tech. Rep., 2009. 5, 38, 93, 145

[3] G. C. Sibilant, A. C. Britten, and H. A. Roets, "Initial results of DC and AC conductor corona tests in Eskom's corona cage test facility," in *Proceedings of Electric Power Research Institure (EPRI) Conference, Denver*, 2007. ix, 6, 7

[4] J. P. Holtzhausen, H. Hendricks, and P. J. Pieterse, "Corona on the Cahora Bassa DC line: Theory and tests on a scale model," in *Proceedings of the 11th South African Universities Power Engineering Conference, SAUPEC*, 2002. 6

[5] E. Acha, V. A. Agelidis, O. Anaya-Lara, and T. J. E. Miller, *Power Electronic Control in Electrical Systems.* Newnes Power Engineering Series, 2002. 6

[6] A. C. Britten, "Verbal Correspondence," Corporate Consultant, Eskom Corporate Services, 2009. 7

[7] *WESTCOR - Western Power Corridor*, Annual Report, 2006-2007. 7

[8] J. D. Cobine, *Gaseous Conductors - Theory and Engineering Applications.* Dover Publications, Inc. New York, 1958. 13, 20

[9] R. G. Urban, "Modelling corona noise on high voltage transmission lines," Master's thesis, University of Stellenbosch, 2001. xii, 13, 27, 106, 117

[10] F. W. Peek, *Dielectric Phenomena in High Voltage Engineering.* McGraw-Hill Book Company, 1915. 13

[11] P. Maruvada, *Corona Performance of High Voltage Transmission.* Research Studies Press Ltd., 2000. xix, 13, 14, 15, 17, 18, 19, 20, 22, 27, 29, 30, 32, 33, 35, 39, 42, 70, 93, 94, 96, 97, 111, 130, 136, 138

[12] M. P. Sarma and W. Janischewskyj, "D. C. corona on smooth conductors in air," *Proc. IEEE*, vol. 116, no. 1, January, 1969. 14, 21, 24, 36, 57, 59, 122

[13] J. B. Whitehead, *High Voltage Corona in International Critical Tables.* McGraw-Hill, 1929. xix, 14

[14] P. K. Paniker, "Ionization of air by corona discharge," Master's thesis, The University of Texas at Arlington, 2003. 14, 18

[15] N. G. Trinh, "Partial discharges in air part ii: Selection of line conductors," *IEEE Electrical Insulation Magazine*, vol. 11, no.3, pp. 5–11, May/June 1995. 14, 39

[16] F. F. Chen, *Introduction to Plasma Physics.* Plenum Press, New York, 1974. 15, 41, 42, 164

[17] N. G. Trinh, "Short notes on the physics of corona discharges," *IEEE/PES Special Course on Corona and Field Effects of High Voltage Transmission Lines, Portland*, July 20-24, 1981. 16, 18, 30, 31, 32, 35

[18] F. W. Sears, M. W. Zemansky, and H. D. Young, *University Physics, 7th Edition.* Addison-Wesley, 1987. ix, 16, 17

[19] F. J. Bueche, *Introduction to Physics for Scientists and Engineers, 4th Edition.* McGraw-Hill, 1986. 17

[20] A. J. Otto, P. J. Pieterse, and H. C. Reader, "An electrometer to measure ion space charge," in *Proceedings of the 18th South African Universities Power Engineering Conference (SAUPEC), Stellenbosch, South Africa*, pp.117-121, January 2009. 17, 80, 145

[21] E. Kuffel, W. S. Zaengl, and J. Kuffel, *High Voltage Engineering Fundamentals.* Butterworth-Heinemann, 2000. 17, 18, 47, 94

[22] E. Nasser, *Fundamentals of Gaseuos Ionization and Plasma Electronics.* Wiley-Interscience, 1971. 17, 19, 24, 25, 26

[23] G. L. Smith, "Distributed source corona photoionization calculations applicable to finite element computer models," *Proc. IEEE Industry Applications Society Annual Meeting*, pp. 1204–1209, 1983. 18, 57

[24] P. S. Maruvada, "Corona-generated space charge environment in the vicinity of HVDC transmission lines," *IEEE Transactions on Electrical Insulation*, vol. EI-17 No.2, pp. 125–130, 1982. 19, 36, 38

[25] B. L. Qin, "High voltage DC bipolar corona via particle-in-cell simulation," Ph.D. dissertation, Washington State University, 1993. 20, 21, 22, 24, 26, 36, 40, 44, 46, 53, 56, 57, 65, 163, 164, 169

[26] J. S. Townsend, *Electricity in Gasses.* Oxford University Press, 1915. 20

[27] T. H. Teich, "Emission gasionisierender Strahlung aus Elektronenlawinen," *Zeitschrift fur Physik*, vol. 199, pp. 378–410, 1967. 23

[28] G. W. Penney and G. T. Hummert, "Photoionization measurements in Air, Oxygen and Nitrogen," *J. of Appl. Phys.*, vol. 41, pp. 572–577, 1970. 23

[29] H. Raether, *Electron Avalanches and Breakdown in Gases.* London: Butterworth & Co. (Publishers) Ltd., 1964. 24, 32

[30] S. C. Brown, *Basic Data of Plasma Physics.* The M.I.T. Press, 1967. 24, 26

[31] J. B. Hasted, *Physics of Atomic Collisions, 2nd edition.* New York: American Elsevier Publishing Company, Inc., 1972. 24, 26

[32] H. Parekh and K. D. Srivastava, "Effect of avalanche space charge field on the calculation of corona onset voltage," *IEEE Trans. on Electrical Insulation*, vol. EI-14, no. 4, pp. 181–192, 1979. 24, 25

[33] S. C. Brown, *Introduction to Electrical Discharges in Gases.* New York: John Wiley & Sons, Inc., 1966. 24

[34] L. B. Loeb, *Electrical Coronas: Their Basic Physical Mechanisms.* University of California Press, 1965. 26, 57

[35] B. Rakoshdas, "Pulses and radio influence voltage of direct voltage corona," *IEEE Trans.*, vol. PAS-83, pp. 483–491, May 1964. 27

[36] S. K. Nayak and M. J. Thomas, "Computation of EMI fields generated due to corona on high voltage over head power transmission lines," in *Proceedings of Seventh International Conference on Electromagnetic Interference and Compatibilty (INCEMIC), Bangalore, pp.15-19*, 2002. 28

[37] E. O. Brigham, *The Fast Fourier Transform and its Applications.* Prentice Hall, Inc., 1988. 28

[38] R. G. Urban, "Power line corona noise prediction for small cage measurement," Ph.D. dissertation, University of Stellenbosch, 2004. 30

[39] M. Abdel-Salam and E. K. Stanek, "Mathematical-physical model of corona from surfaces on high-voltage lines," *IEEE Transactions on Industry Applications*, vol. IA-23, no.3, pp. 481–489, 1987. x, 30, 57, 58

[40] G. A. Dawson, "A model for streamer propagation," *Zeitschrift fur Phyics*, vol. 183, p. 159, 1965. 32

[41] N. G. Trinh and J. B. Jordan, "Modes of corona discharges in air," *IEEE Trans. on Power Apparatus and Systems*, vol. PAS-87, no. 5, pp. 1207–1215, May 1968. 32

[42] *IEEE Guide for Measurement of DC Electric-Field Strength and Ion Related Quantities.* IEEE Std 1227-1990, (R2001). ix, xi, 36, 81, 82

[43] A. P. Fews, R. J. Wilding, P. A. Keitch, N. K. Holden, and D. L. Henshaw, "Modification of atmospheric DC fields by space charge from high-voltage power lines," *Atmospheric Research*, vol. 63, pp. 271–289, 2002. 36

[44] T. D. Bracken, A. S. Capon, and D. V. Montgomery, "Ground level electric fields and ion currents on the Celilo-Sylmar ±400kV DC intertie during fair weather," *IEEE Trans.*, vol. PAS-97, pp. 370–378, March/April 1978. 36

[45] G. Hartmann, "Theoretical evaluation of Peek's law," *IEEE Transactions on Industry Applications*, vol. IA-20, no. 6, pp. 1647–1651, 1984. 37

[46] P. S. Maruvada, R. D. Dallaire, O. C. Norris-Elye, C. V. Thio, and J. S. Goodman, "Environmental effects of the Nelson River HVDC transmission lines - RI, AN, electric field, induced voltage, and ion current distribution tests," *IEEE Transactions on Power Apperatus and Systems*, vol. PAS-101, pp. 951–959, 1982. 37

[47] F. Fatokun, "Corona ions from high voltage powerlines: Production, effect on ambient particles and implications on human exposure studies," Ph.D. dissertation, Queensland University of Technology, 2008. 38, 39

[48] *EPRI High-Voltage Direct Current Handbook.* EPRI, Palo Alto CA:, 1994. 38, 137, 182

[49] D. Govender and G. C. Sibilant, "HVDC line space charge effects," RES/RR/08/29087, Eskom Sustainability and Innovation, Tech. Rep., 2008. 38, 182

[50] *CISPR 18: Radio Interference Characteristics of Overhead Power Lines and High Voltage Equipment.* CISPR Standard, Publication 18-1, 1982. 38, 97, 130

[51] *EPRI Advanced HVDC Systems at ±800kV and Above.* EPRI, Palo Alto, CA:, 2007. 39

[52] J. M. K. MacAlpine and C. H. Zang, "The effect of humidity on the charge/phase-angle patterns of AC corona pulses in air," *IEEE Transactions on Dielectrics and Electrical Insulation*, vol. 10, no. 3, pp. 506–513, 2003. 39

[53] H. Jianfeng, G. Zhicheng, and W. Liming, "Study on AC and DC corona inception voltage at different air pressures and relative humidity conditions," in *Proceedings of the XIVth International Symposium on High Voltage Engineering*, 2005. 39

[54] F. G. Heymann, "Corona on wires in air," *Transactions of the South African Institute of Electrical Engineers (SAIEE)*, vol. 56, Part 11, pp. 271–290, 1965. 39

[55] R. G. Olsen and S. D. Schennum, "A method for calculating wide band electromagnetic interference from power line corona," *IEEE Transactions on Power Delivery*, vol. 10, no. 3, pp. 1535–1540, 1995. 39, 108

[56] CIGRÉ/IEEE, "Survey on extra high voltage transmission line radio noise," *IEEE/PES Special Course: Corona and Field Effects of AC and DC High Voltage Transmission Lines*, pp. 221–230, Spetember, 1982. 39

[57] W. Baoquan, L. Dichen, and W. Xiong, "The study of the radio interference from ± 800kV Yun Guang UHVDC transmission line," in *International Conference on Power System Technology*, 2006. 39

[58] C. K. Birdsall and A. B. Langdon, *Plasma Physics Via Computer Simulation.* Taylor & Francis Group, 2005. 40, 53

[59] R. W. Hockney and J. W. Eastwood, *Computer Simulation Using Particles.* IOP Publishing Ltd., Institute of Physics, London, 1992. 40, 42, 49, 56

[60] B. L. Qin, J. N. Sheng, Z. Yan, and G. Gela, "Accurate calculation of ion flow under HVDC bipolar transmission lines," *IEEE Transactions on Power Delivery*, vol. 3, no. 1, pp. 368–376, 1988. 40

[61] B. L. Qin and P. Pedrow, "Particle-in-cell simulation of bipolar DC corona," *IEEE Transactions on Dielectrics and Electrical Insulation*, vol. 1, no.6, pp. 1104–1118, 1994. 40

[62] L. Arevalo, M. Becerra, and B. Roman, "Numerical simulation of the positive corona current behavior," in *Proceedings of the XIVth International Symposium on High Voltage Engineering*, August, 2005. 41, 58, 59

[63] ——, "Numerical simulation of negative corona in coaxial cylindrical arrangement," in *Proceedings of the XIVth International Symposium on High Voltage Engineering*, August, 2005. 41, 58, 59

[64] C. Soria, F. Pontiga, and A. Castellanos, "Numerical modeling of an electron avalanche in Oxygen by a particle method," in *IEEE Conference on Electrical Insulation and Dielectric Phenomena, Minneapolis*, October, 1997. 41

[65] Z. Al-Hamouz and M. Abdel-Salam, "Finite element solution of monopolar corona on bundle conductors," in *IEEE Industry Application Society, Annual Meeting, New Orleans, Louisiana*, October, 1997. 41

[66] H. Singer, H. Steinbigler, and P. Weiss, "A charge simulation method for the calculation of high voltage fields," *IEEE Power Engineering Society Winter Meeting*, pp. 1660–1668, 1973. 46, 47, 48

[67] J. Jin, *The Finite Element Method in Electromagnetics, 2nd edition.* John Wiley & Sons, Inc., New York, 2002. 49, 50, 55

[68] P. Silvester and R. Ferrari, *Finite Element for Electrical Engineers.* Cambridge University Press, 1996. 49, 50

[69] D. B. Davidson, *Computational Electromagnetics for RF and Microwave Engineering.* Cambridge University Press, 2005. 50, 51, 52, 157

[70] H. C. Martina and G. F. Carey, *Introduction to Finite Element Analysis.* McGraw-Hill, Inc., 1973. 50

[71] A. Friedman, S. E. Parker, S. L. Ray, and C. K. Birdsall, "Multi-scale particle-in-cell plasma simulation," *Journal of Computational Physics*, vol. 6, pp. 54–70, 1991. 56

[72] J. W. Daniel and R. E. Moore, *Computation and Theory in Ordinary Differential Equations.* W. A. Freeman & Co. , San Francisco, 1970. 56

[73] M. Khalifa and M. Abdel-Salam, "Improved calculation of corona pulse characteristics," *IEEE PES Winter Meeting, New York, N.Y.*, 1974. 57, 58, 59

[74] S. El-Debeiky and M. Khalifa, "Calculating the corona pulse characteristics and its radio interference," *IEEE Transactions on Power Apparatus and Systems*, vol. PAS-90, No. 1, pp. 165–179, 1971. 58, 59, 74, 75, 76

[75] H. A. Haus and J. R. Melcher, *Electromagnetic Fields and Energy.* Prentice Hall, New Jersey, 1989. 63, 86, 163

[76] S. Ramo, J. R. Whinnery, and T. V. Duzer, *Fields and Waves in Communications Electronics, 3rd edition.* John Wiley & Sons, Inc., 1994. 64, 87

[77] P. Hammond, *Electromagnetism for Engineers - An Introductionary Course.* Pergamon Press Ltd., 1978. 65, 163

[78] J. M. Meek and J. D. Craggs, *Electrical Breakdown in Gasses.* Oxford University Press, 1953. 74

[79] R. Bartinakas and E. McMahon, Eds., *Engineering Dielectrics Volume 1: Corona Measurement and Interpretation.* ASTM: American Society for Testing and Materials, STP 669, 1979. 74

[80] J. P. Holtzhausen, P. J. Pieterse, C. Wahl, and H. J. Vermeulen, "A comparison of the AC and DC corona inception levels and modes for various conductors in air," in *Proceedings of the 15th International Symposium on High Voltage Engineering, Ljubjana, Slovenia*, August 27-31, 2007. 74

[81] A. J. Otto, H. C. Reader, and P. J. Pieterse, "Ion space charge measurement and simulation," in *Proceedings of the 16th International Symposium on High Voltage (ISH), Cape Town, South Africa*, 24-28 August 2009. 80, 145

[82] N. G. Trinh and P. S. Maruvada, "A method of predicting the corona performance of conductor bundles based on cage test results," *IEEE Transactions on Power Apparatus and Systems*, vol. PAS-96, pp. 312–325, 1977. 93

[83] M. Moreau and C. H. Gary, "Predetermination of radio interference level of high voltage transmission lines. part i: Predetermination of the excitation function," *IEEE Transactions on Power Apparatus and Systems*, vol. PAS-91, pp. 284–291, 1972. 93

[84] M. G. Comber and L. E. Zaffanella, "The use of single-phased overhead test lines and test cages to evaluate the corona effects of EHV and UHV transmission lines," *IEEE Transactions on Power Apparatus and Systems*, vol. PAS-93, pp. 81–90, 1974. 93

[85] R. D. Dallaire, P. S. Maruvada, and N. Rivest, "HVDC monopolar and bipolar cage studies on the corona performance of conductor bundles," *IEEE Transactions on Power Apparatus and Systems*, vol. PAS-103, no. 1, pp. 84–91, January 1984. xix, 93, 138, 139

[86] M. C. Perz, "Method of evaluating corona noise generation from meaurements on short test lines," *AIEE Fall General Meeting, Chicago, Ill.*, pp. 833–844, 1962. 96

[87] *CISPR 18: Radio Interference Characteristics of Overhead Power Lines and High Voltage Equipment, Part 2: Methods of Measurement and Procedure for Determining Limits.* CISPR Standard, Publication 18-2, 1986. 97, 103, 105

[88] P. S. Maruvada, N. Hylten-Cavallius, and N. T. Chinh, "Radio noise meter response to random pulses by computer simulation," *IEEE PES Summer Meeting & EHV/UHV Conference*, pp. 905–915, 1973. xii, 106, 107, 108

[89] T. Williams, *EMC for Product Engineers, 4th Edition.* Newness, 2007. xii, 107

[90] *CISPR 16: Specification fir Radio Disturbance and Immunity Measuring Apparatus and Methods.* CISPR Standard, Publication 16-1, 2004. 107

[91] Z. Guan, L. Wang, B. Yang, and Z. Liang, "Electric field analysis of water drop corona," *IEEE Transactions on Power Delivery*, vol. 20, no.2, pp. 946–969, April 2005. 108

[92] N. G. Trinh, P. S. Maruvada, and B. Poirier, "A comparative study of the corona performance of conductor bundles for 1200kV transmission lines," *IEEE PES Summer Meeting & EHV/UHV Conference*, pp. 940–949, July, 1973. 111, 132

[93] O. Nigol, "Analysis of radio noise from high-voltage lines, i: Meter response to corona pulses," *IEEE Transactions on Power Apparatus and Systems*, vol. 83, pp. 524–533, 1964. 114

[94] M. M. Khalifa, A. A. Kamal, A. G. Zeitoun, R. M. Radwan, and S. El-Bedwaihy, "Correlation of radio noise and quasi-peak measurements to corona pulse randomness," *IEEE Transactions on Power Apparatus and Systems*, vol. PAS-88, no. 10, pp. 1512–1521, 1969. 127

[95] D. F. Williams, T. S. Clement, P. D. Hale, and A. Dienstfrey, "Terminology for high-speed sampling-oscilloscope calibration," in *68th Automatic Radio Frequency Techniques Group (ARFTG) Conference, Omni Interlocken Resort, Broomfield, Colorado*, December, 2006. 130

[96] F. G. Stremler, *Introduction to Communication Systems.* Reading, MA: Addison-Wesley Publishing Company, 1982. 130

[97] C. H. Gary, "The theory of the excitation function: A demonstration of its physical meaning," *IEEE Power Engineering Society Winter Meeting*, vol. Paper 71 TP 153-PW, p. 305:310, December 1970. 132, 134, 137

[98] G. E. Adams, "The calculation of the radio interference level of transmission lines caused by corona discharges," *AIEE Trans.*, vol. III, p. 411:419, June 1956. 132

[99] V. L. Chartier, "Methods of calculating the EMI from transmission lines," *IEEE/PES Special Course: Corona and Field Effects of AC and DC High Voltage Transmission Lines*, pp. 207–220, September, 20-24, 1982. 136

[100] F. W. Hirsch and E. Schaffer, "Progress report on the HVDC test line of the 400kV-Forschungsgemeinschaft: Corona losses and radio interference," *IEEE Trans.*, vol. PAS-88, pp. 1061–1069, July 1969. 137

[101] N. Knudsen and F. Iliceto, "Contribution to the electrical design of HVDC overhead lines," *IEEE Trans.*, vol. PAS-93, pp. 233–239, Januray/February 1974. 137

[102] A. J. Otto, "DC conductor corona: Interim report," RES/RR/08/29086, Eskom Sustainability and Innovation, Tech. Rep., 2009. 137, 145

[103] CIGRÉ, "Addendum to CIGRÉ Document No. 20 (1974)," in *CIGRÉ Brochure No. 61, p.106*, 1996. 137

[104] P. S. Maruvada, N. G. Trinh, R. D. Dallaire, N. Rivest, and P. Heroux, "Bipolar HVDC transmission system study between ±600kV and ±1200kV: Corona studies, phase 1," *Electric Power Research Institute, Palo Alto, California, EPRI EL*, 1979. 138

[105] P. S. Maruvada, R. D. Dallaire, P. Heroux, and N. Rivest, "Long term statistical study of the corona electric field and ion-current performance of a ± 900kV bipolar HVDC transmission line configuration," *IEEE Transactions on Power Apparatus and Systems*, vol. PAS-103, no. 1, pp. 76–83, 1984. 138

[106] A. J. Otto, R. Warrington, H. C. Reader, and R. van Zyl, "An interim report on the development of an electric field mill for HVDC application," RES/RR/09/30524, Eskom Sustainability and Innovation, Tech. Rep., 2009. 145

[107] *High Voltage Test Set PGK 260 HB, Data Sheet, Baur Pruef- und Messtechnik GmbH, Austria.* xv, 160, 161

[108] J. M. Wetzer and P. C. T. van der Laan, "Prebreakdown currents basic interpretation and time-resolved measurements," *IEEE Transaction on Electrical Insulation*, vol. 24, no.2, pp. 297–308, 1989. 163

[109] P. Lorrain and D. R. Corson, *Electromagnetism Principles and Applications.* W.H. Freeman and Company, New York, 1990. 164

[110] W. Wang, C. Li, J. Fan, C. Cu, Y. Jiang, and G. Cui, "Study of UHV DC corona performance in a mini corona cage," in *IEEE Electrical Insulation Conference and Electrical Manufacturing Expo*, 2007. 178

[111] V. L. Chartier and R. D. Stearns, "Examination of Grizzly Mountain data base to determine effects of relative air density and conductor temperature on HVDC corona phenomena," *IEEE Transactions on Power Delivery*, vol. 5, no. 3, pp. 1575–1582, 1990. 178

[112] H. A. Roets and N. P. Tlhatlhetji, "Measurement and prediction of corona-generated audible noise," RES/RR/04/24487, Eskom Technology Services International (TSI), Tech. Rep., 2004. 178

Appendix A

Computational Mathematics

A.1 Partial Differentiation of Matrices and Vectors

Assume C to be a scalar constant and $[A]$ a constant matrix:

$$\frac{\partial C\{x\}}{\partial\{x\}} = C \tag{A.1.1}$$

$$\frac{\partial\{x\}^T[A]\{x\}}{\partial\{x\}} = 2[A]\{x\} \tag{A.1.2}$$

A.2 Simplex Coordinate Formulas

A.2.0.1 Simplex Coordinates on a Triangle

$$\lambda_1 + \lambda_2 + \lambda_3 = 1 \tag{A.2.1}$$

A.2.0.2 Integration over Triangle

$$\int\int_S \lambda_1^i \lambda_2^j \lambda_3^k dS = \frac{2!i!j!k!}{(2+i+j+k)!} A \tag{A.2.2}$$

A.2.0.3 Gradient on a Triangle

$$\nabla\lambda_i = \frac{l_i}{2A}\hat{n}_i \tag{A.2.3}$$

with A the area of the triangle, l_i the length of edge i and $\hat{n}_i$ the normal vector on edge i, pointing into the triangle [69]

Appendix B

UV Intensifying Corona Camera

B.1 Electrometer Measurements

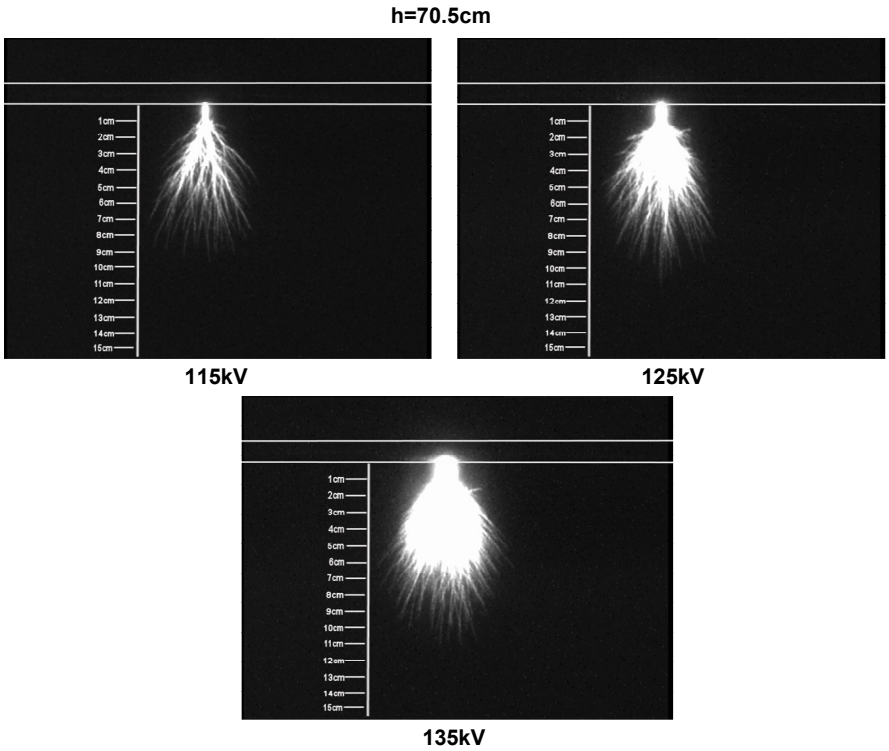

Figure B.1: A set of onset streamer discharges captured with a UV intensifying corona camera for a conductor height $h = 70.5cm$ (vertical scale in $1cm$ increments)

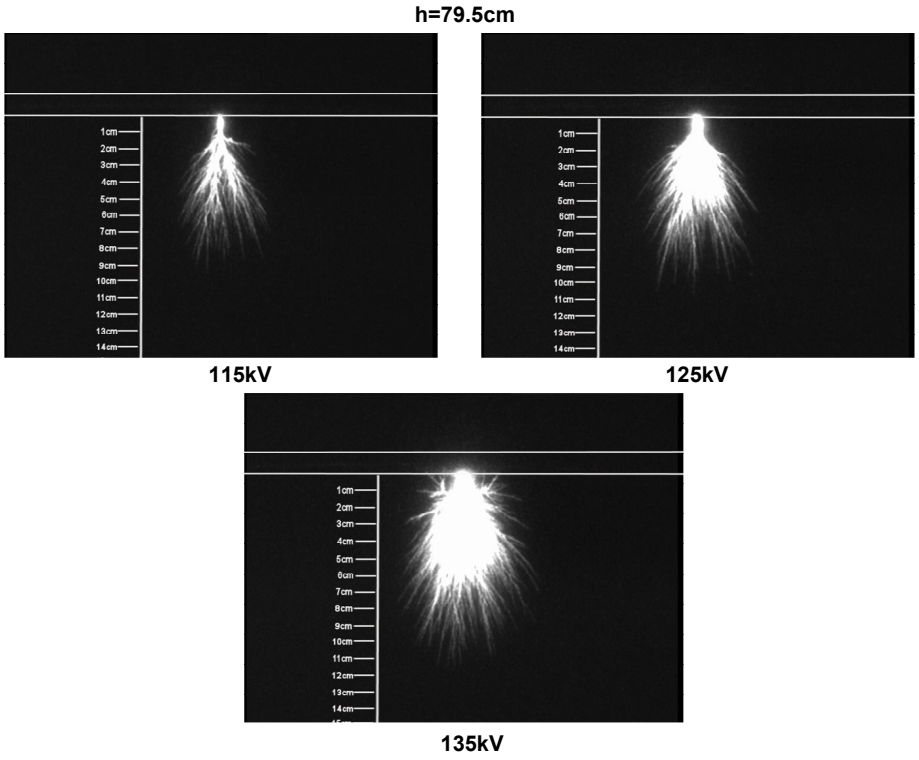

Figure B.2: A set of onset streamer discharges captured with a UV intensifying corona camera for a conductor height $h = 79.5cm$ (vertical scale in $1cm$ increments)

B.2 Corona Cage Measurements

The results for corona cage measurements for impedance matching tests are shown in this section.

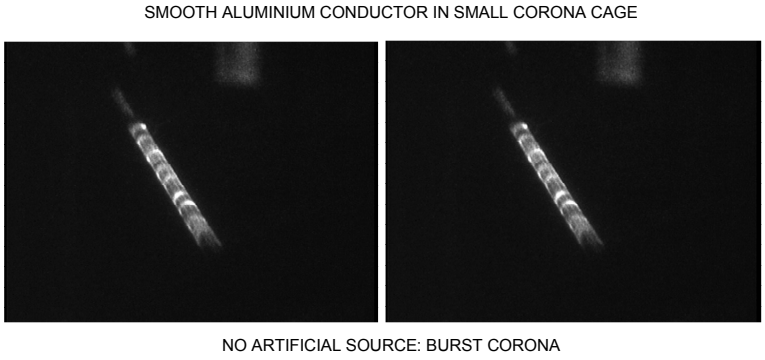

Figure B.3: Positive burst corona on smooth aluminium conductor in small corona cage

Appendix C

Direct Current Voltage Source

The direct current (DC) voltage source used for the various measurements is a BAUR PGK 260 HB test [107] as shown in figure C.1.The source is a single diode half wave rectification circuit that is rated at $\pm 260kV$ with an output current of $4mA$. The DC source uses a single phase power supply.

Figure C.1: BAUR PGK 260 HB voltage source [107]

The $500kHz$ blocking filter attached to the top of the DC voltage source is shown in figure C.2. The load diagram for the source is shown in figure C.3.

Figure C.2: DC Source with blocking filter attached

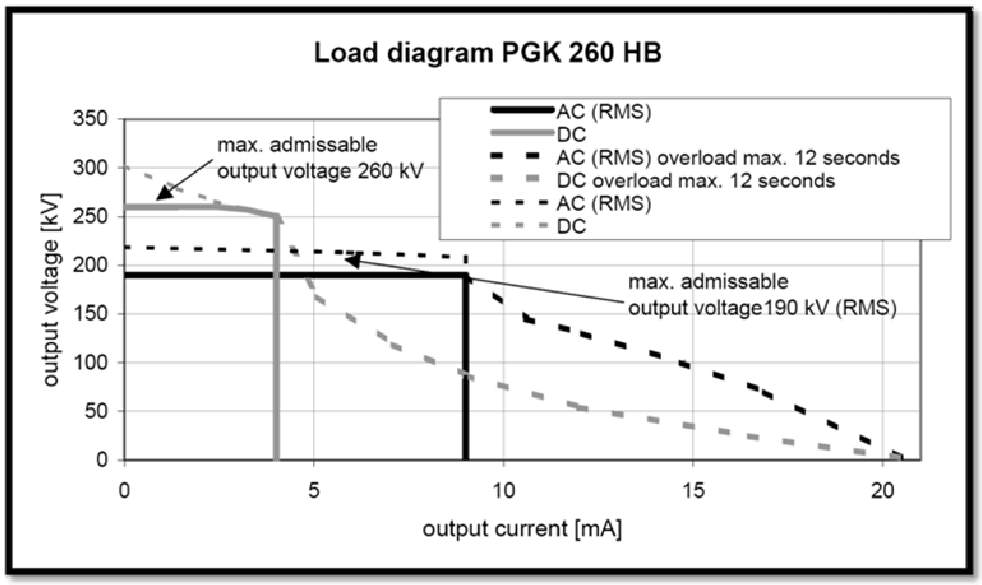

Figure C.3: Load diagram for DC voltage source [107]

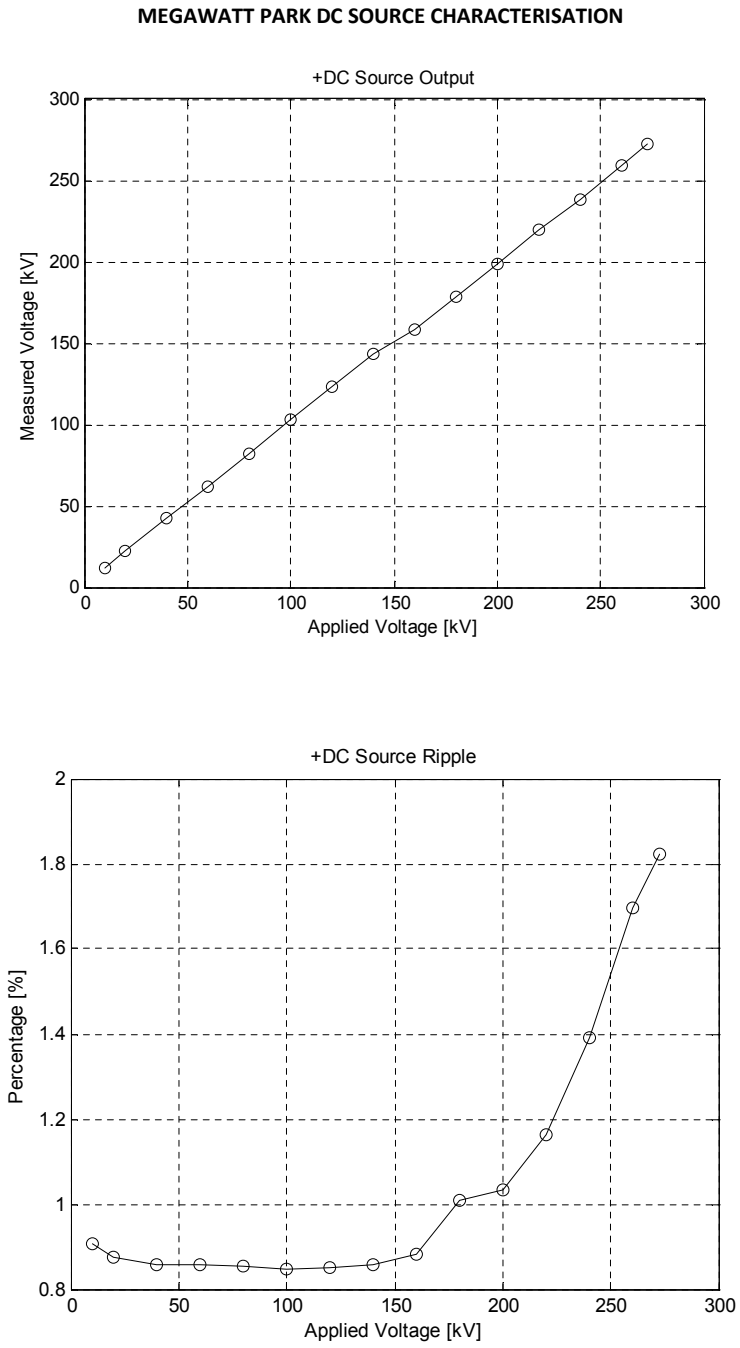

Figure C.4: Characterisation of DC source at Eskom's Megawatt Park test facility

Appendix D

Charge Motion Between Cylindrical Electrodes

This section investigates the analytical solution of charge motion between cylindrical electrodes in an electrostatic potential conductor corona process. The analytical modelling of charge shells were then used to evaluate and interpret particle simulation results. These techniques should be compared to [25] [108].

D.1 Analytical Solution - Anode Corona

In the case of an anode conductor of radius r_a and a cathode sheath of radius r_b in a cylindrical geometry there is a charge $+Q$ on the inner conductor and a charge $-Q$ on the outer sheath when applying an electrostatic voltage V_0. At a time $t = 0$ electron and positive ion shells are placed in the cylindrical system at a radius $r = r_0$. The electrons are collected and neutralized by the anode while the positive ions are collected and neutralized by the cathode. It is important to note that in order to solve the analytical solution to find the position of these particles at a time $t > 0$ it is assumed that the electric field between the two cylindrical conductors where not greatly affected by the space charge. For a cylindrical geometry of length l the electric flux density at any radius r is obtained by Gauss's theorem [77]

$$\vec{D} \times 2\pi r l = Q \tag{D.1.1}$$

The electric field in a cylindrical geometry as well as for a uniform line charge is given by [75]

$$\vec{E} = \frac{Q}{2\pi\epsilon_0 l}\frac{1}{r} \tag{D.1.2}$$

and knowing that $V = -\int_{r_b}^{r_a} E dr$ we have that

$$V = \frac{Q}{2\pi\epsilon_0 l} ln(r_b/r_a) \tag{D.1.3}$$

The capacitance $C = Q/V$ [109] of the cylindrical geometry hence yields

$$C = \frac{2\pi\epsilon_0 l}{ln(r_b/r_a)} \tag{D.1.4}$$

It was seen in equation 3.2.6 that the velocity of a particle is given by

$$\vec{v} = \mu\vec{E} - D\frac{\nabla n}{n}$$

where D is the *diffusion* constant and n is the *number density*. When considering a single simulation particle and hence neglecting the *diffusion* term the velocity is then given by [16] [25]

$$\frac{d\vec{r}(t)}{dt} = \mu\vec{E} \tag{D.1.5}$$

In order to find the position of a simulation particle at a time t one integrates equation D.1.5 which then yields

$$\int_{r_0}^{r(t)} r dr = \int_0^t \mu\frac{Q}{2\pi\epsilon_0 l} dt$$

$$r(t) = \sqrt{r_0^2 + \frac{2\mu V_0}{ln(r_b/r_a)}t} \tag{D.1.6}$$

The time it will take for a positive simulation particle to be collected by the cathode is calculated by setting $r(t) = r_b$ and $t = t_p$

$$t_p = \frac{ln(r_b/r_a)}{2\mu_p V_0}(r_b^2 - r_0^2) \tag{D.1.7}$$

Similarly for the electron simulation particles to be collected by the anode we set $r(t) = r_a$ and $t = t_e$

$$t_e = \frac{ln(r_b/r_a)}{2\mu_e V_0}(r_a^2 - r_0^2) \tag{D.1.8}$$

Consider the case where positive ions with charge $+Q$ is at a position r_p and electrons with negative charge $-Q$ is at a position r_e in a coaxial arrangement with conductor radius r_a and charge Q_a and sheath radius r_b and charge Q_b as in figure D.11.

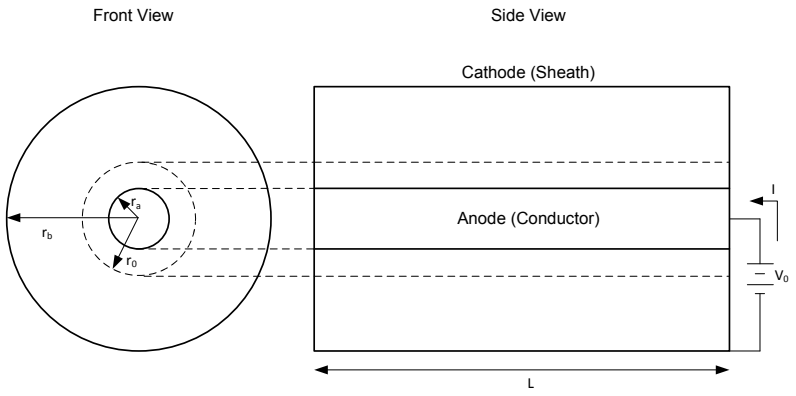

Figure D.1: Cylindrical electrodes: anode corona analytical study

Positive Ions and Electrons in System - $t\epsilon(0, t_e)$

The potential difference between the two electrodes from the boundary conditions when there are both positive ions and electrons available can be expressed as

$$V_0 = \int_{r_a}^{r_e(t)} E(r)dr + \int_{r_e(t)}^{r_p(t)} E(r)dr + \int_{r_p(t)}^{r_b} E(r)dr \tag{D.1.9}$$

where the electric field as a function of radial position is given by

$$E(r) = \begin{cases} \frac{Q_a}{2\pi\epsilon_0}\frac{1}{r} & \text{if } r\epsilon(r_a, r_e(t)) \\ \frac{Q_a - Q}{2\pi\epsilon_0}\frac{1}{r} & \text{if } r\epsilon(r_e(t), r_p(t)) \\ \frac{Q_a}{2\pi\epsilon_0}\frac{1}{r} & \text{if } r\epsilon(r_p(t), r_b) \end{cases} \tag{D.1.10}$$

Q_a is the total charge on the anode (conductor) and Q_b is total charge on the cathode (sheath). Substituting D.1.10 into D.1.9 and integrating yields

$$V_0 = \frac{Q_a}{2\pi\epsilon_0} ln(r_e(t)/r_a) + \frac{Q_a}{2\pi\epsilon_0} ln(r_p(t)/r_e(t)) - \frac{Q}{2\pi\epsilon_0} ln(r_p(t)/r_e(t)) + \frac{Q_a}{2\pi\epsilon_0} ln(r_b/r_p(t))$$

$$Q_a(t) = \frac{1}{ln(r_b/r_a)}(2\pi\epsilon_0 V_0 + Q ln(r_p(t)/r_e(t))) \tag{D.1.11}$$

The total charge at a time $t = t_e$ on the anode will however also consist of the electron charge neutralizing on the conductor at that time. This can be modeled as a unit step function $u(t)$ yielding

$$Q_a(t) = \frac{1}{ln(r_b/r_a)}(2\pi\epsilon_0 V_0 + Q ln(r_p(t)/r_e(t))) - Q u(t - t_e) \tag{D.1.12}$$

Similarly the total charge on the cathode (sheath) is given by

$$Q_b(t) = -Q_a(t) - Q u(t - t_e) \tag{D.1.13}$$

The current I that will flow in the external circuit as in figure D.11 is then given by

$$I_a = I_b = \frac{dQ_a}{dt}$$

$$\frac{dQ_a}{dt} = \frac{Q}{ln(r_b/r_a)}\frac{d}{dt}(ln(r_p(t)) - ln(r_e(t))) - Q\frac{d}{dt}(u(t-t_e))$$

$$\frac{dQ_a}{dt} = \frac{QV_0}{ln(r_b/r_a)^2}(\frac{\mu_p}{r_p(t)^2} - \frac{\mu_e}{r_e(t)^2}) - Q\delta(t-t_e) \tag{D.1.14}$$

For the total charge on the cathode (sheath) (equation D.1.13) the current is given by

$$\frac{dQ_b}{dt} = -\frac{QV_0}{ln(r_b/r_a)^2}(\frac{\mu_p}{r_p(t)^2} - \frac{\mu_e}{r_e(t)^2}) + Q\delta(t-t_e) - Q\delta(t-t_e)$$

$$\frac{dQ_b}{dt} = -\frac{QV_0}{ln(r_b/r_a)^2}(\frac{\mu_p}{r_p(t)^2} - \frac{\mu_e}{r_e(t)^2}) \tag{D.1.15}$$

Only Positive Ions in System - $t\epsilon(t_e, t_p)$

For the case when there are only positive ions present in the inter-electrode region the potential difference is given by

$$V_0 = \int_{r_a}^{r_p(t)} E(r)dr + \int_{r_p(t)}^{r_b} E(r)dr$$

$$V_0 = \frac{Q_a}{2\pi\epsilon_0} ln(r_p(t)/r_a) + \frac{Q_a + Q}{2\pi\epsilon_0} ln(r_b/r_p(t))$$

The total charge on the anode is thus given by

$$Q_a(t) = \frac{1}{ln(r_b/r_a)}(2\pi\epsilon_0 V_0 + Q ln(r_p(t)/r_b)) \tag{D.1.16}$$

while the total charge on the cathode is given by

$$Q_b(t) = -Q_a(t) + Qu(t - t_p) \tag{D.1.17}$$

The current in the external circuits is then given by

$$\frac{dQ_a}{dt} = \frac{Q}{ln(r_b/r_a)} \frac{d}{dt}(ln(r_p(t)))$$

$$\frac{dQ_a}{dt} = \frac{QV_0}{(ln(r_b/r_a))^2}(\frac{\mu_p}{r_p(t)^2}) \tag{D.1.18}$$

$$\frac{dQ_b}{dt} = -\frac{QV_0}{(ln(r_b/r_a))^2}(\frac{\mu_p}{r_p(t)^2}) + Q\delta(t - t_p) \tag{D.1.19}$$

The current for the simple anode corona model can be summarized as

$$i_a(t) = i_b(t) = \begin{cases} \frac{QV_0}{(ln(r_b/r_a))^2}(\frac{\mu_p}{r_p(t)^2} - \frac{\mu_e}{r_e(t)^2}) & \text{if } t\epsilon(0, t_e) \\ \frac{QV_0}{(ln(r_b/r_a))^2}\frac{\mu_p}{r_p(t)^2} & \text{if } t\epsilon(t_e, t_p) \\ 0 & \text{otherwise} \end{cases} \tag{D.1.20}$$

D.1.1 Specific Example - Anode Corona

We now consider a specific cylindrical electrode anode corona example similar to [25] which is solved analytically as well as numerically using the 2D PIC code. The results are then compared and discussed in this section.

Consider the following parameters with reference to figure D.11:

$$r_a = 3.7mm$$
$$r_b = 19cm$$
$$V_0 = 50kV$$
$$r_0 = r_a + 1cm = 1.37cm$$
$$\mu_p = 1.37cm^2.V^{-1}.s^{-1}$$
$$\mu_e = -300\mu_p cm^2.V^{-1}.s^{-1}$$
$$C_0 = \frac{2\pi\epsilon_0 l}{ln(r_b/r_a)} = 14.1pF$$
$$Q_0 = C_0V_0 = 707nC$$
$$Q = 100nC$$
$$l = 1m$$

The charge of the simulation particles Q has been chosen to be much smaller than the electrostatic charge Q_0 so that the trajectories of the simulation particles can be approximated using the electric field as if no space charge are present similar to [25].

Using techniques from the previous section and similar to [25] we can now express the total charge on the anode and cathode respectfully as

$$Q_a = C_0V_0 + Q\{[u(t) - u(t-t_e)]ln(r_p(t)/r_e(t))/ln(r_b/r_a) \\ -[u(t-t_e) - u(t-t_p)]ln(r_b/r_p(t))/ln(r_b/r_a)\}$$

$$Q_b = -C_0V_0 - Q\{[u(t) - u(t-t_e)]ln(r_p(t)/r_e(t))/ln(r_b/r_a) \\ +[u(t-t_e) - u(t-t_p)][1 - ln(r_b/r_p(t))/ln(r_b/r_a)]\}$$

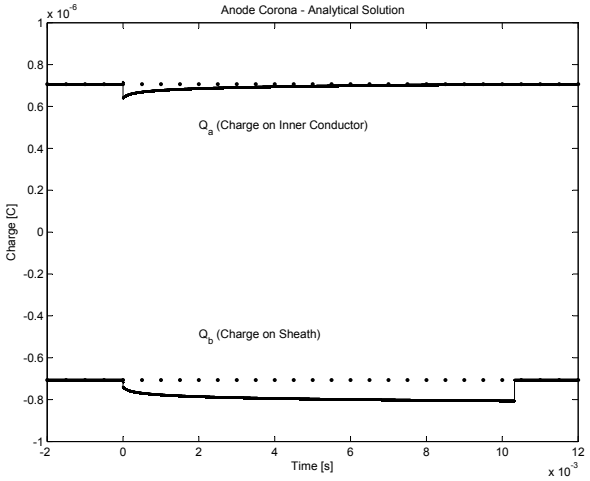

Figure D.2: Anode corona analytical solution to the total charge on the electrodes

The charge on the inner electrode (conductor) in the nanosecond scale is shown in figure D.3 while the charge on the outer electrode (sheath conductor) in the nanosecond scale is shown in figure D.4

From equation D.1.6 the position of the positive ion shells versus time can be expressed as

$$r_p = \sqrt{r_0^2 + \frac{2\mu_p V_0}{ln(r_b/r_a)}t} \tag{D.1.21}$$

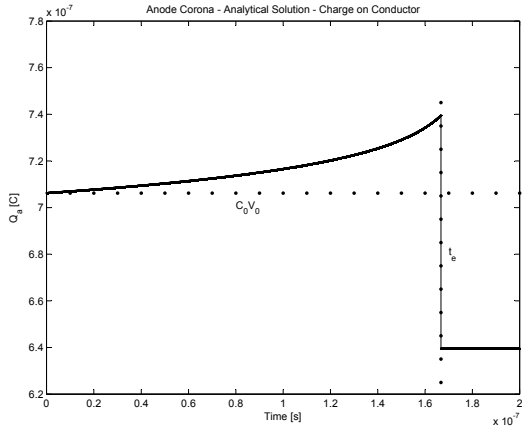

Figure D.3: Anode corona analytical solution to the charge on the inner electrode

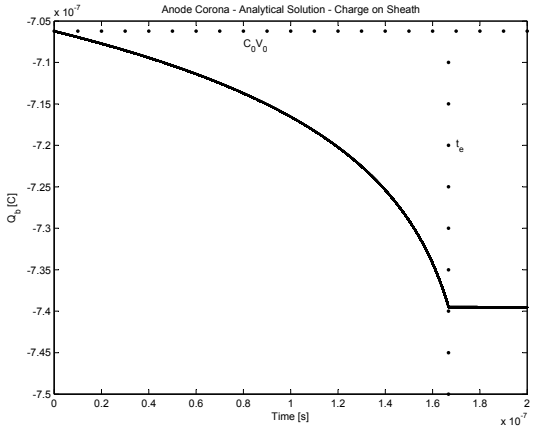

Figure D.4: Anode corona analytical solution to the charge on the outer electrode

while the position of the electron shells versus time (when assuming that the electron mobility is constant in the drift zone such that $\mu_e = -300\mu_p$) can be expressed as

$$r_e = \sqrt{r_0^2 - \frac{2(300\mu_e)V_0}{ln(r_b/r_a)}t} \tag{D.1.22}$$

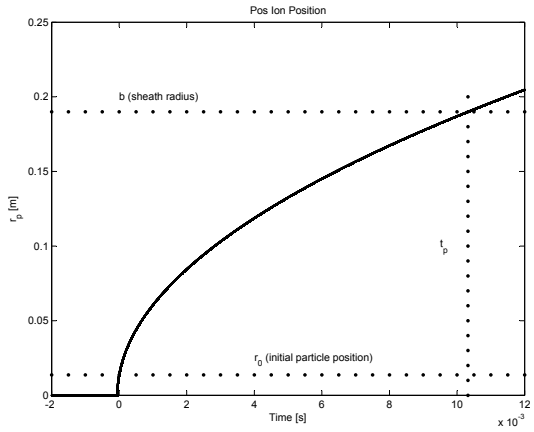

Figure D.5: Anode corona analytical solution for the positive ion position

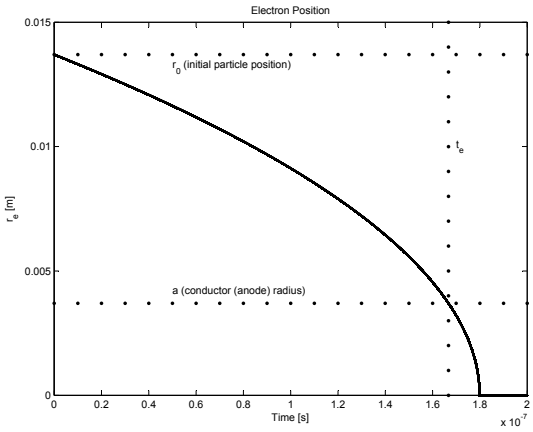

Figure D.6: Anode corona analytical solution for the electron position

From equation D.1.20 the current can be expressed as

$$i = \frac{V_0 Q \mu_p}{(ln(r_b/r_a))}\{[u(t) - u(t-t_e)][\frac{1}{r_p(t)^2} + \frac{300}{r_e(t)^2}] + [u(t-t_e) - u(t-t_p)]\frac{1}{r_p(t)^2}\} \quad \text{(D.1.23)}$$

The analytical solution to the current on the anode in the milisecond scale is shown in figure D.7, while the nanosecond scale is shown in D.8. The time it will take for the positive ion shells to neutralize on the cathode (equation D.1.7) is

$$t_p = \frac{ln(r_b/r_a)}{2\mu_p V_0}(r_b^2 - r_0^2) = 10.3ms$$

while the time it will take for the electron shells to neutralize on the anode (equation D.1.8) is

$$t_e = \frac{ln(r_b/r_a)}{2\mu_e V_0}(r_a^2 - r_0^2) = 167ns$$

The analytical solution to the current and charge on the anode in log-log scale is shown in figures D.9 and D.10 respectively.

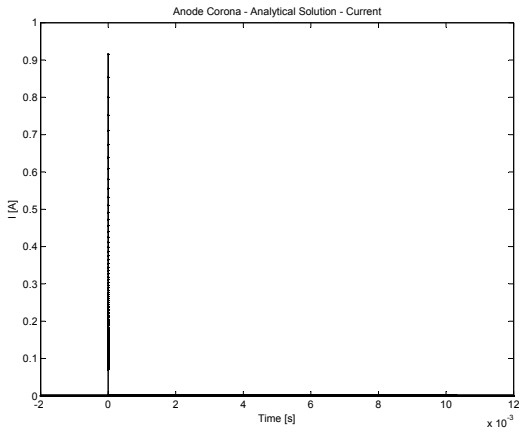

Figure D.7: Anode corona analytical solution for the current in a millisecond scale

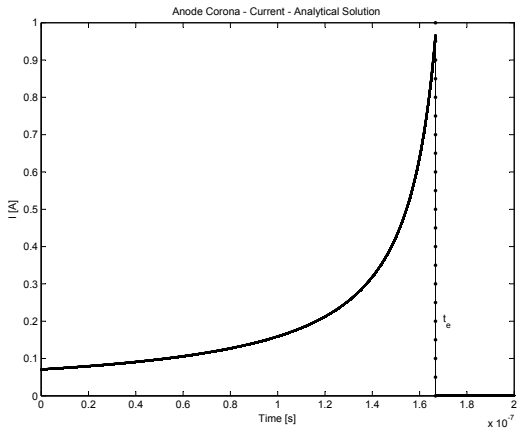

Figure D.8: Anode corona analytical solution for the current in a nanosecond scale

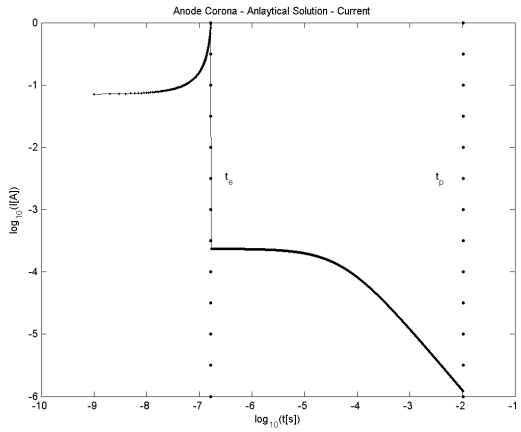

Figure D.9: Anode corona analytical solution for current (log-log scale)

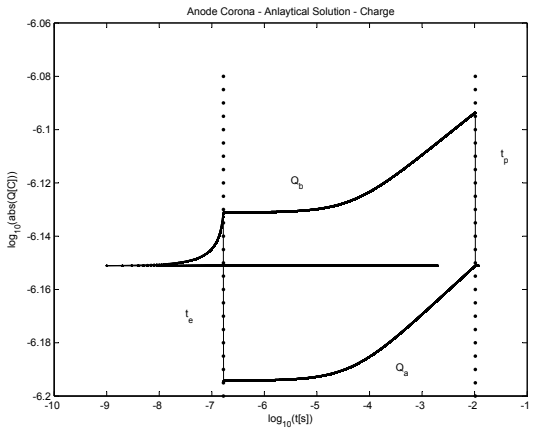

Figure D.10: Anode corona analytical solution for charge (log-log scale)

D.2 Analytical Solution - Cathode Corona

Electron and positive ion shells with charge $-Q$ and $+Q$ respectively are again placed at a position $r = r_0$ at time $t = t_0$. The electrons are drawn to the anode (sheath) and at a position $r = r_A$ they are assumed to be out of the ionization zone and are converted by attachment to negative ions. These negative ions are then neutralized on the sheath. The positive ion shells are drawn to and neutralized on the cathode (conductor).

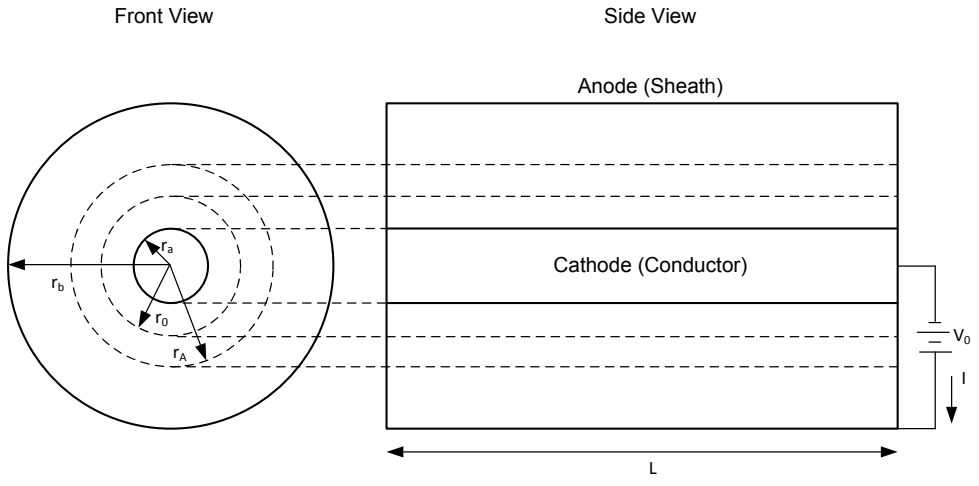

Figure D.11: Cylindrical electrodes: cathode corona analytical study

Positive Ions and Electrons in System - $t\epsilon(0, t_e)$

Similar to the analytical anode solution for both positive ions and electrons present the potential difference can again be written as

$$V_0 = -\int_{r_a}^{r_p(t)} Edr - \int_{r_p(t)}^{r_e(t)} Edr - \int_{r_e(t)}^{r_b} Edr$$

where the electric field as an expression of radial distance is this time given by

$$E(r) = \begin{cases} \frac{Q_a}{2\pi\epsilon_0}\frac{1}{r} & \text{if } r\epsilon(r_a, r_p(t)) \\ \frac{Q_a+Q}{2\pi\epsilon_0}\frac{1}{r} & \text{if } r\epsilon(r_p(t), r_e(t)) \\ \frac{Q_a}{2\pi\epsilon_0}\frac{1}{r} & \text{if } r\epsilon(r_e(t), r_b) \end{cases} \tag{D.2.1}$$

Using similar techniques described in the analytical solution of the anode corona one can show that

$$Q_a(t) = \frac{-1}{ln(r_b/r_a)}(2\pi\epsilon_0 V_0 + Qln(r_e(t)/r_p(t)))$$

$$Q_a(t) = \frac{1}{ln(r_b/r_a)}(2\pi\epsilon_0(-V_0) + Qln(r_p(t)/r_e(t))) \tag{D.2.2}$$

$$Q_b(t) = -Q_a(t) \tag{D.2.3}$$

The currents in the external circuits can similarly be expressed as

$$\frac{dQ_a}{dt} = \frac{QV_0}{(ln(r_b/r_a))^2}(\frac{\mu_p}{r_p(t)^2} - \frac{\mu_e}{r_e(t)^2}) \tag{D.2.4}$$

$$\frac{dQ_b}{dt} = -\frac{QV_0}{(ln(r_b/r_a))^2}(\frac{\mu_p}{r_p(t)^2} - \frac{\mu_e}{r_e(t)^2}) \tag{D.2.5}$$

These equations are for a time $t\epsilon(0, t_e)$.

Positive Ions and Negative Ions in System - $t\epsilon(t_e, t_p)$

The potential difference when there are positive ions and electrons that have been converted to negative ions - attachment available is given by

$$V_0 = -\int_{r_a}^{r_p(t)} Edr - \int_{r_p(t)}^{r_n(t)} Edr - \int_{r_n(t)}^{r_b} Edr$$

where the electric field in terms of radial position given by

$$E(r) = \begin{cases} \frac{Q_a}{2\pi\epsilon_0}\frac{1}{r} & \text{if } r\epsilon(r_a, r_p(t)) \\ \frac{Q_a+Q}{2\pi\epsilon_0}\frac{1}{r} & \text{if } r\epsilon(r_p(t), r_n(t)) \\ \frac{Q_a}{2\pi\epsilon_0}\frac{1}{r} & \text{if } r\epsilon(r_n(t), r_b) \end{cases} \tag{D.2.6}$$

Using similar techniques as before the total charge on the anode for a time $t\epsilon(t_e, t_p)$ is given by

$$Q_a(t) = \frac{1}{ln(r_b/r_a)}(2\pi\epsilon_0(-V_0) + Qln(r_p(t)/r_n(t))) + Qu(t - t_p) \tag{D.2.7}$$

while the total charge on the cathode is given by

$$Q_b(t) = -Q_a(t) + Qu(t - t_p) \tag{D.2.8}$$

The currents in the external circuits are given by

$$\frac{dQ_a}{dt} = \frac{QV_0}{(ln(r_b/r_a))^2}(\frac{\mu_p}{r_p(t)^2} - \frac{\mu_n}{r_n(t)^2}) + Q\delta(t - t_p) \tag{D.2.9}$$

$$\frac{dQ_b}{dt} = -\frac{QV_0}{(ln(r_b/r_a))^2}(\frac{\mu_p}{r_p(t)^2} - \frac{\mu_n}{r_n(t)^2}) - Q\delta(t - t_p) + Q\delta(t - t_p)$$

$$\frac{dQ_b}{dt} = -\frac{QV_0}{(ln(r_b/r_a))^2}(\frac{\mu_p}{r_p(t)^2} - \frac{\mu_n}{r_n(t)^2}) \tag{D.2.10}$$

Only Negative Ions in System - $t\epsilon(t_p, t_n)$

The potential difference when only negative ions remain in the inter-eletrode region is given by

$$V_0 = -\int_{r_a}^{r_n(t)} Edr - \int_{r_n(t)}^{r_b} Edr$$

while the electric field in terms of radial position is given by

$$E(r) = \begin{cases} \frac{Q_a}{2\pi\epsilon_0}\frac{1}{r} & \text{if } r\epsilon(r_a, r_n(t)) \\ \frac{Q_a - Q}{2\pi\epsilon_0}\frac{1}{r} & \text{if } r\epsilon(r_n(t), r_b) \end{cases} \tag{D.2.11}$$

Using similar techniques as before the total charge on the anode for a time $t\epsilon(t_p, t_n)$ is given by

$$Q_a(t) = \frac{1}{ln(r_b/r_a)}(2\pi\epsilon_0(-V_0) - Qln(r_n(t)/r_b)) \tag{D.2.12}$$

while the total charge on the cathode is given by

$$Q_b(t) = -Q_a(t) - Qu(t - t_n) \tag{D.2.13}$$

The currents in the external circuits are given by

$$\frac{dQ_a}{dt} = -\frac{QV_0}{(ln(r_b/r_a))^2}(\frac{\mu_n}{r_n(t)^2}) \tag{D.2.14}$$

$$\frac{dQ_b}{dt} = \frac{QV_0}{(ln(r_b/r_a))^2}(\frac{\mu_n}{r_n(t)^2}) - Q\delta(t - t_n) \tag{D.2.15}$$

where $t\epsilon(t_p, t_n)$.

The current for the cathode corona can thus be summarised as

$$i_a(t) = i_b(t) = \begin{cases} \frac{QV_0}{(ln(r_b/r_a))^2}(\frac{\mu_p}{r_p(t)^2} - \frac{\mu_e}{r_e(t)^2}) & \text{if } t\epsilon(0, t_e) \\ \frac{QV_0}{(ln(r_b/r_a))^2}(\frac{\mu_p}{r_p(t)^2} - \frac{\mu_n}{r_n(t)^2}) & \text{if } t\epsilon(t_e, t_p) \\ \frac{QV_0}{(ln(r_b/r_a))^2}(\frac{\mu_n}{r_n(t)^2}) & \text{if } t\epsilon(t_p, t_n) \\ 0 & \text{otherwise} \end{cases} \tag{D.2.16}$$

Appendix E

Altitude Effects on RI Measurements

A small mobile corona cage is used in an initial study to investigate the effect of altitude on corona inception and RI levels. The *Zebra* and *Kingbird* conductors discussed in chapter 5 were used in RI performance measurements at various altitude levels from 0 to 2000m above sea level for positive and negative polarity DC. Some aspects of the tests conducted can be compared to work done in [110]. Work regarding relative air density and conductor temperature on HVDC corona phenomena was furthermore done in [111].

It was concluded in this disseration's research regarding various corona test methods, that the small corona cage cannot be used to predict the RI on an actual transmission line accurately. The results discussed in this section can be used for performance comparison of different conductor types, not for actual RI prediction. The RI work discussed in this section compliments the effect of altitude on the AC and DC audible noise (AN) measurements done in [112]. Although differences in RI levels for similar voltage gradients at different altitudes are noted to be greater than the literature predicted 1dB/300m, further studies need to be done on a different measurement system. The higher RI levels at higher altitudes should be confirmed not to be space charge related effects. The possibility of using a portable type test line should be considered to perform RI measurements at various altitudes, to ensure that the space charge does not affect the conductor electric field conditions.

The altitude measurements done for this dissertation at the various testing sites in South Africa were made possible by Mr. Riaan Roets from *Kiepersol Technologies*. Further assistance was provided by Mr. Coenie Esterhuizen and Mr. Jaco Badenhorst (*Eskom*).

E.1 Altitude Measurements: Zebra Conductor

The small corona cage characterised in section 5.1.1 was used for measurements at various heights above sea level in order to investigate the effect of the change in air pressure on the inception and extinction gradients, as well as the RI levels at various gradients. The weather conditions, including the temperature and relative humidity (RH), as well as the air pressure values at each site were recorded as in tables E.1 and E.2.

The first set of alitude measurements were done using a single *Zebra* conductor with a diameter of $\phi = 28.68mm$. Only the CISPR $500kHz$ narrowband measurements, as discussed in section 5.3.2, were made during these tests. These measurements were made during the end of the summer in March 2009.

Altitude Measurements: Zebra Conductor					
Date	**Site**	**Height**	**Pressure**	**Temp**	**RH**
2009/03/14	Paarl	123m	748.6mmHg	31^oC	38%
2009/03/15	Montugu	553m	711.1mmHg	38.2^oC	38%
2009/03/12	Beaufort West	925m	693.8mmHg	27.5^oC	45%
2009/04/09	Midrand	$1550m$	637.6mmHg	24^oC	35%
2009/03/23	Clarens	$1900m$	615.1mmHg	29^oC	54%

Table E.1: Zebra altitude RI measurement sites and atmospheric conditions

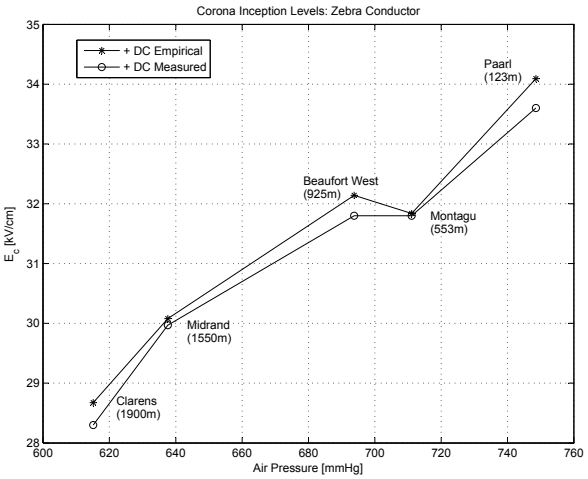

Figure E.1: Corona inception levels for Zebra conductor at various air pressures

Using equation 2.1.2, the corona inception levels for the *Zebra* conductor for the various air pressures and temperatures are calculated as in figure E.1. These calculations are for a Zebra conductor with roughness factor $m = 0.87$. The measured RI magnitude levels for various surface voltage gradients at different heights above sea level are shown in E.2.

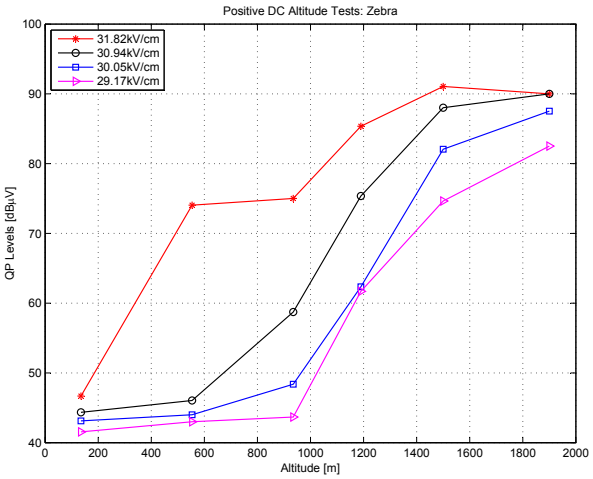

Figure E.2: RI magnitude levels for various surface voltage gradients at different heights above sea level

E.2 Altitude Measurements: Kingbird Conductor

The next set of altitude measurements were made with a *Kingbird* conductor with a diameter of $\phi = 23.88mm$. Both wideband time domain and frequency domain measurements, as well as the CISPR $500kHz$ narrowband measurements were made during the winter month of July.

Using equation 2.1.2, the corona inception levels for the *Kingbird* conductor for the various air pressures and temperatures are calculated as in figure E.3. These calculations are for a Kingbird conductor with roughness factor $m = 0.87$.

Altitude Measurements: Kingbird Conductor					
Date	**Site**	**Height**	**Pressure**	**Temp**	**RH**
2009/07/07	Paarl	156m	756.4mmHg	19.9^{o}C	58%
2009/07/08	Laingsburg	580m	719.3mmHg	18.3^{o}C	47.3%
2009/07/06	Beaufort West	951m	684.8mmHg	14.8^{o}C	38.2%
2009/07/09	De Aar	1240m	661.9mmHg	9.9^{o}C	43%
2009/07/17	Midrand	1550m	644.8mmHg	12.6^{o}C	54.5%
2009/07/14	Clarens	1900m	612.20mmHg	8.9^{o}C	35%

Table E.2: Kingbird altitude RI measurement sites and atmospheric conditions

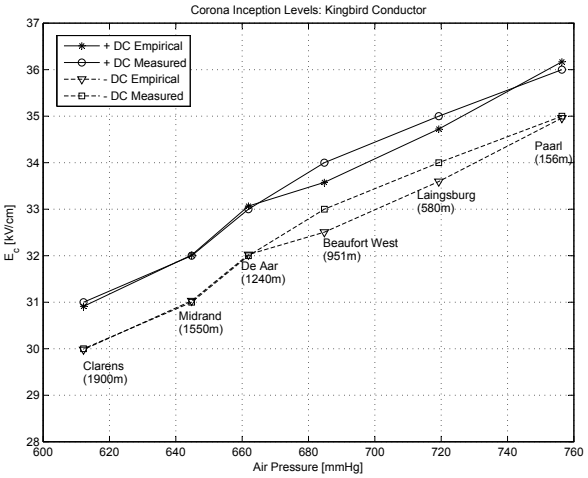

Figure E.3: Corona inception levels for Kingbird conductor at various air pressures

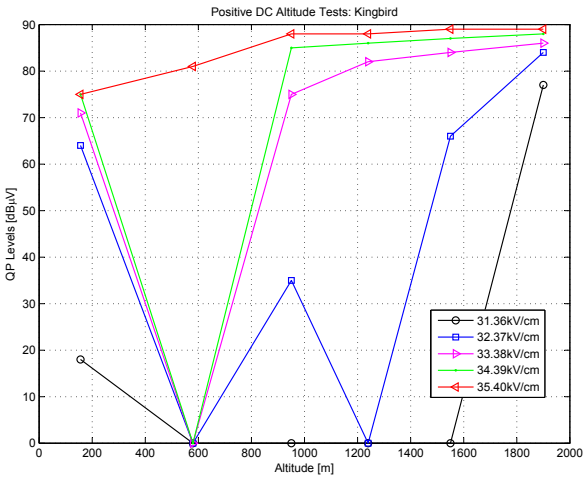

Figure E.4: RI magnitude levels for various surface voltage gradients at different heights above sea level

E.2.1 Paarl: 156m

The test site in Paarl is situated in the Cape Winelands are of the Western Cape region of South Africa at a height of about 156m above sea level. The measurements commenced at 11:30am, and there was a very slight wind blowing. It was noted in [48] and [49] that insects are attracted to positive pole DC conductors. This phenomena was indeed observed as insects formed small corona sources as shown in figure E.5 when doing the positive DC measurements.

Figure E.5: Insects attracted to the positive DC conductors, fittings and and generator feed

The insects had to be cleared regularly in order to not mistake their influence on the RI levels for the line's corona performance. It was furthermore noted that the insects were not drawn to the negative DC conductor. For the positive DC corona, a couple of onset streamer discharges were audible at a surface voltage gradient of $36.31kV/cm$. This was just high enough to put the Kingbird conductor into corona. The streamer discharges diminished and a hissing sound was audible at surface voltage gradient of $35.4kV/cm$. The hissing sound of the negative DC corona was not really audible below a surface voltage gradient of $34.39kV/cm$, which was the inception level. The widband and narrowband RI results are shown in figures E.6 to E.9.

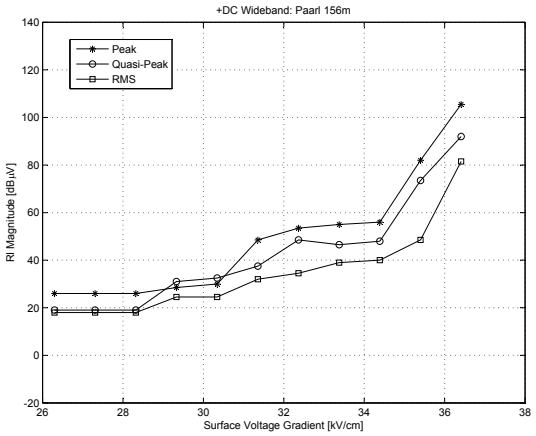

Figure E.6: Positive DC wideband measurements with EMI receiver tuned to $500kHz$

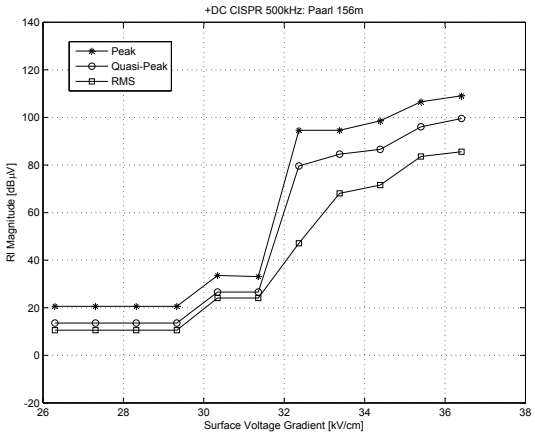

Figure E.7: Positive DC CISPR narrowband measurements with EMI receiver tuned to $500kHz$

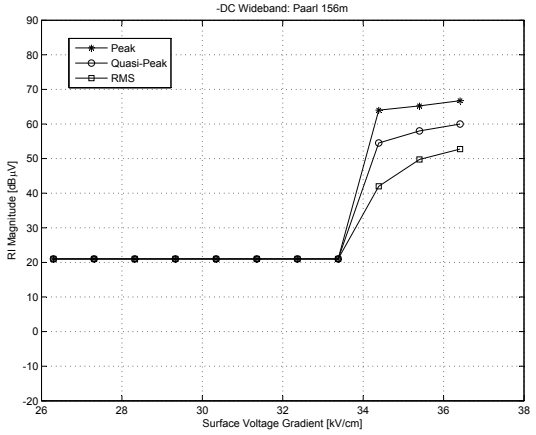

Figure E.8: Negative DC wideband measurements with EMI receiver tuned to $500kHz$

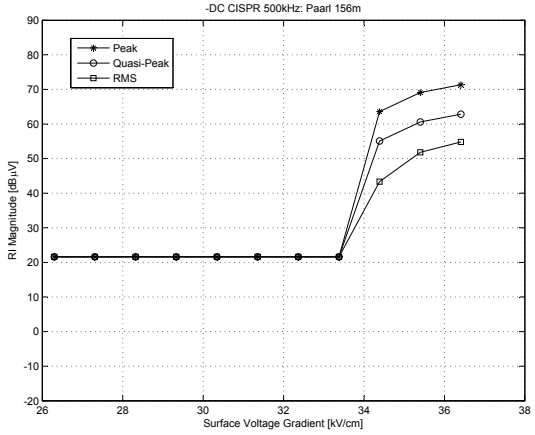

Figure E.9: Negative DC CISPR narrowband measurements with EMI receiver tuned to $500kHz$

E.2.2 Laingsburg: 580m

The test site in Laingsburg is situated at 580m above sea level in the Little Karoo area of the Western Cape region of South Africa. The measurements commenced at 11:38am. The positive DC corona inception level was noted to be at a surface voltage gradient of $35kV/cm$. The streamer discharges were not really audible below this level. The negative DC corona inception level was at a surface voltage gradient of $34kV/cm$. The wideband and narrowband RI results are shown in figures E.10 to E.13. A difference between the negative DC corona inception and extinction levels when moving up from a low to a high, and down from a high to a low surface voltage gradient was noted and is shown in figures E.36 and E.37.

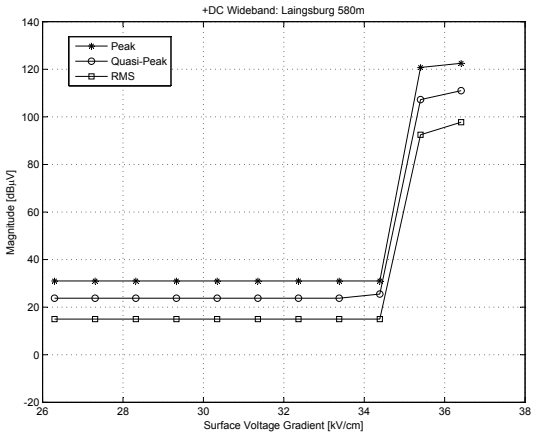

Figure E.10: Positive DC wideband measurements with EMI receiver tuned to $500kHz$

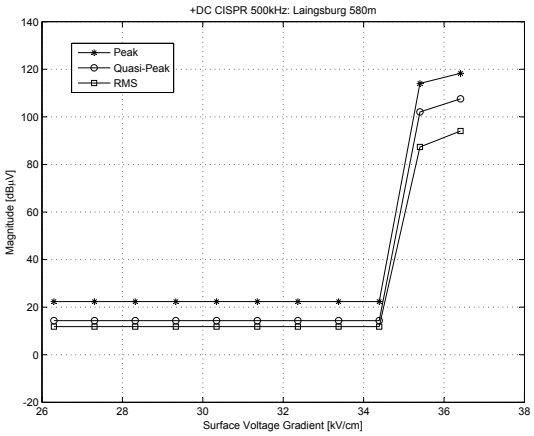

Figure E.11: Positive DC CISPR narrowband measurements with EMI receiver tuned to $500kHz$

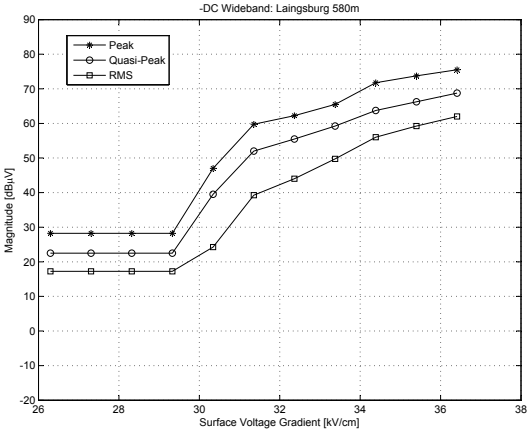

Figure E.12: Negative DC wideband measurements with EMI receiver tuned to $500kHz$

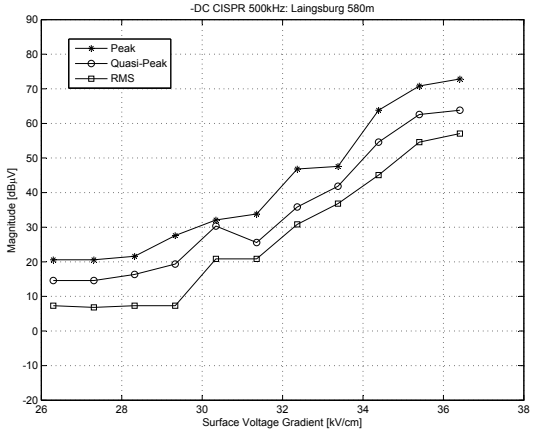

Figure E.13: Negative DC CISPR narrowband measurements with EMI receiver tuned to $500kHz$

E.2.3 Beaufort West: 951m

The test site in Beaufort West is situated at 951m above sea level, and is situated in the Great Karoo area of the Western Cape region of South Africa. The positive DC corona inception level was noted at a surface voltage gradient of $34.4kV/cm$, while the negative DC inception level was noted at $33.4kV/cm$. The wideband and narrowband RI peak, quasi-peak and rms results are shown in figures E.14 to E.17.

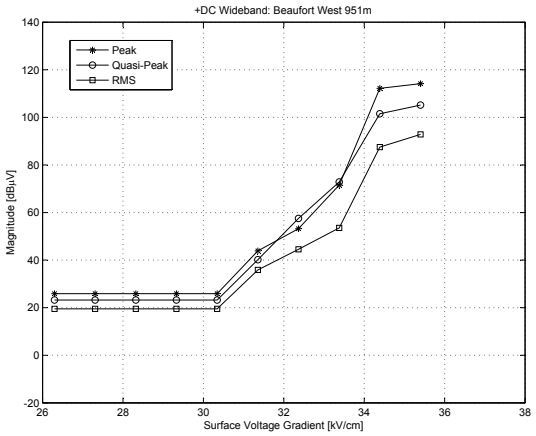

Figure E.14: Positive DC wideband measurements with EMI receiver tuned to $500kHz$

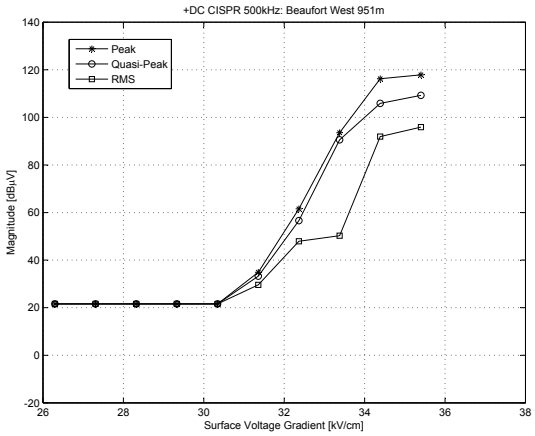

Figure E.15: Positive DC CISPR narrowband measurements with EMI receiver tuned to $500kHz$

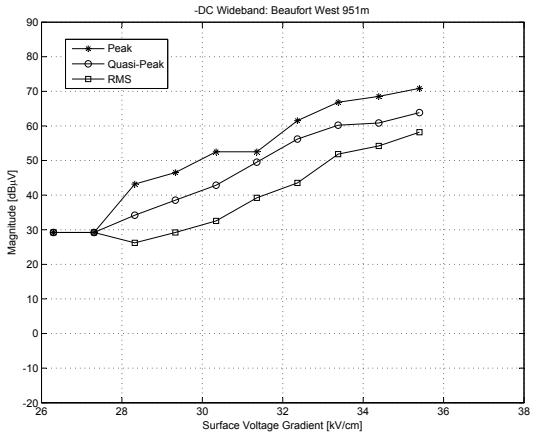

Figure E.16: Negative DC wideband measurements with EMI receiver tuned to $500kHz$

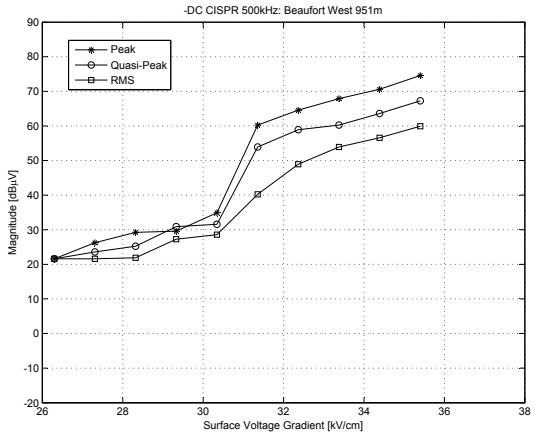

Figure E.17: Negative DC CISPR narrowband measurements with EMI receiver tuned to $500kHz$

E.2.4 De Aar: 1240m

The test site in De Aar is situated at 1240m above sea level in the Northen Cape region of South Africa. The measurement sequence commenced at 8:42am. The positive DC corona inception level was noted at $33.38kV/cm$, while the negative DC corona was $32.37kV/cm$. It should also be noted that the weather conditions were not only quite cold, but also quite windy when these tests were conducted. The wideband and narrowband RI peak, quasi-peak and rms results are shown in figures E.18 to E.21. The corona inception and extinction levels when moving up from a low to a high, and down from a high to a low surface voltage gradient are shown in figures E.40 and E.41.

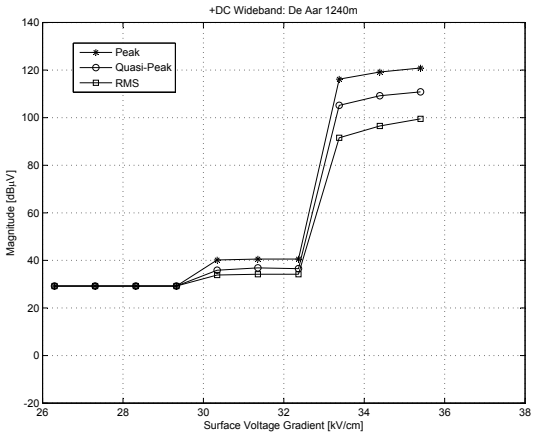

Figure E.18: Positive DC wideband measurements with EMI receiver tuned to $500kHz$

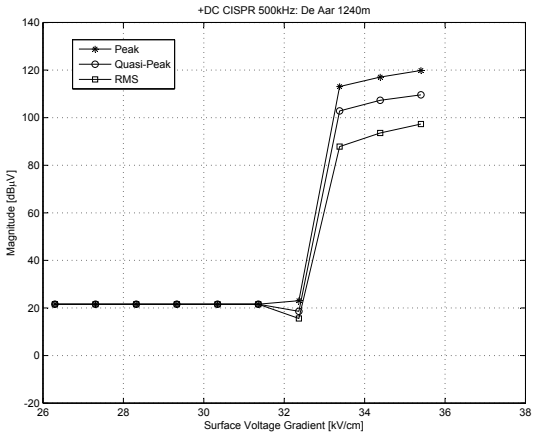

Figure E.19: Positive DC CISPR narrowband measurements with EMI receiver tuned to $500kHz$

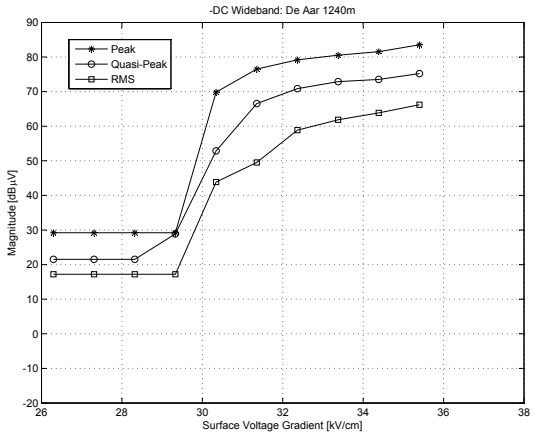

Figure E.20: Negative DC wideband measurements with EMI receiver tuned to $500kHz$

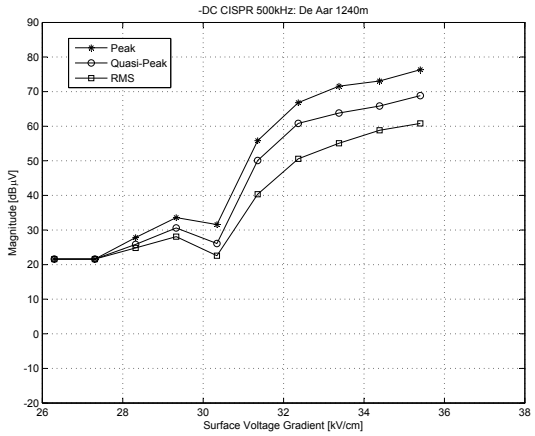

Figure E.21: Negative DC CISPR narrowband measurements with EMI receiver tuned to $500kHz$

E.2.5 Midrand: 1550m

The test site in Midrand is situated at 1550m above sea level in the Gauteng region of South Africa. The measurement sequence commenced at 9:50am. The positive DC corona inception level was noted at $32.37kV/cm$, while the negative DC corona was between $31.36kV/cm$ and $32.37kV/cm$. The wideband and narrowband RI peak, quasi-peak and rms results are shown in figures E.22 to E.25. The corona inception and extinction levels when moving up from a low to a high, and down from a high to a low surface voltage gradient are shown in figures E.44 and E.45.

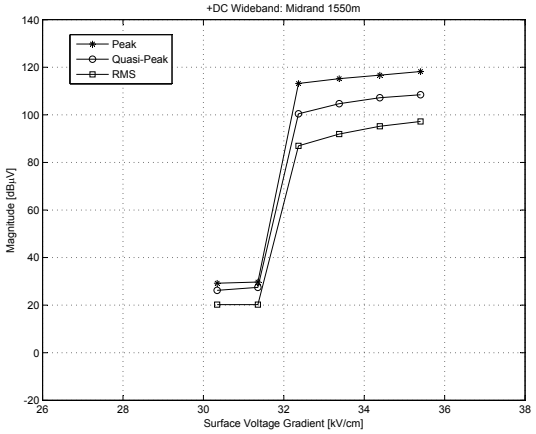

Figure E.22: Positive DC wideband measurements with EMI receiver tuned to $500kHz$

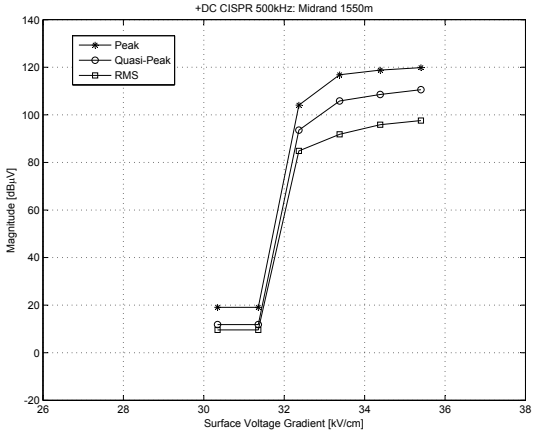

Figure E.23: Positive DC CISPR narrowband measurements with EMI receiver tuned to $500kHz$

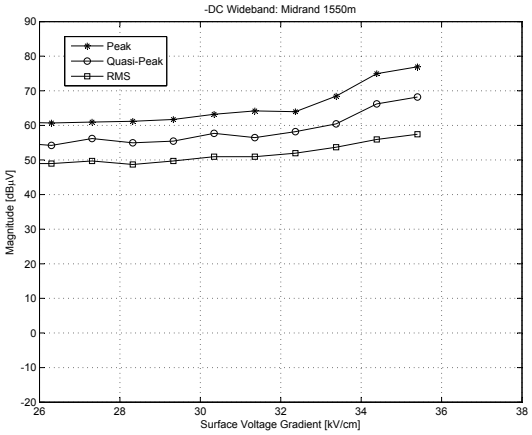

Figure E.24: Negative DC wideband measurements with EMI receiver tuned to $500kHz$

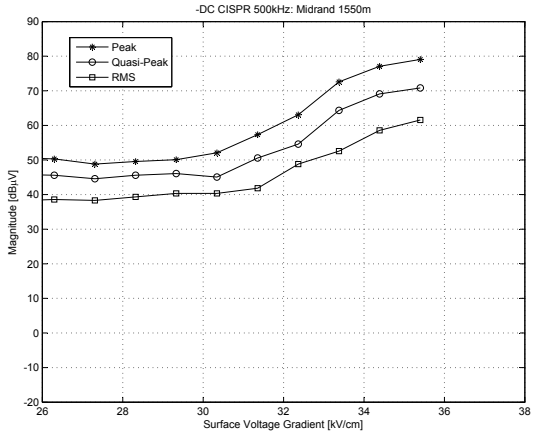

Figure E.25: Negative DC CISPR narrowband measurements with EMI receiver tuned to $500kHz$

E.2.6 Clarens: 1900m

The test site at Clarens is at 1900m above sea level and is situated in the eastern Free State region in South Africa. This is on the Lesotho border in the Drakensberg. The weather conditions were cold and windy when these measurements were made. The positive DC corona inception levels were noted to be $31.36kV/cm$, while the negative corona was between $29.33kV/cm$ and $30.34kV/cm$. The wideband and narrowband RI peak, quasi-peak and rms results are shown in figures E.26 to E.29. The corona inception and extinction levels when moving up from a low to a high, and down from a high to a low surface voltage gradient are shown in figures E.48 and E.49.

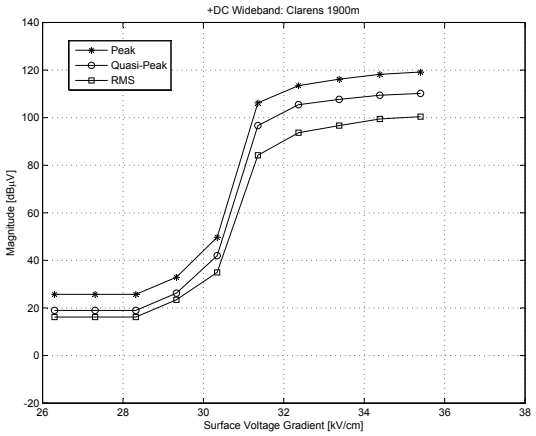

Figure E.26: Positive DC wideband measurements with EMI receiver tuned to $500kHz$

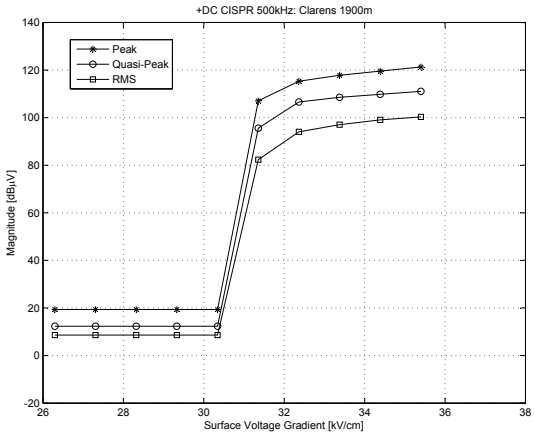

Figure E.27: Positive DC CISPR narrowband measurements with EMI receiver tuned to $500kHz$

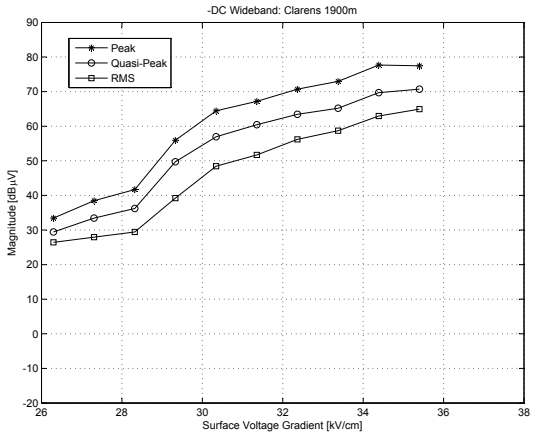

Figure E.28: Negative DC wideband measurements with EMI receiver tuned to $500kHz$

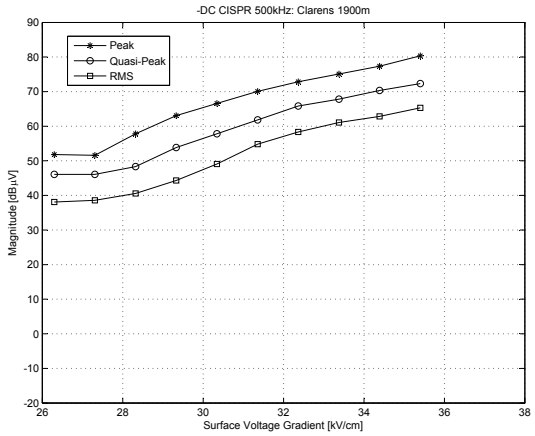

Figure E.29: Negative DC CISPR narrowband measurements with EMI receiver tuned to $500kHz$

E.2.7 Up and Down Readings: Kingbird

The quasi-peak measurement results included in this section of the appendix are from the March 2009 altitude RI measurements using the *Kingbird* conductor in the small corona cage. These results are the average quasi-peak values in $[dB\mu V]$ moving up from a low to a high surface voltage gradient, and down from a high to a low surface voltage gradient.

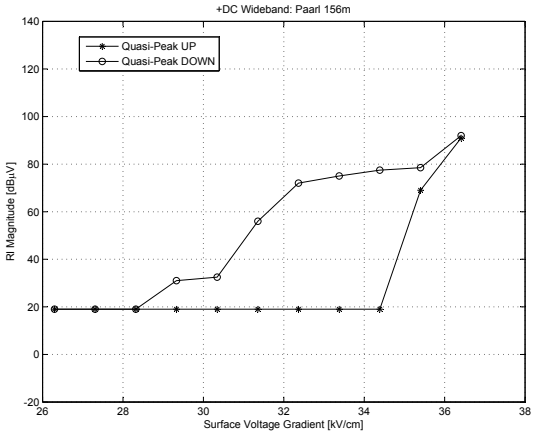

Figure E.30: Positive DC quasi-peak results for wideband measurements moving up and down in voltage (Paarl)

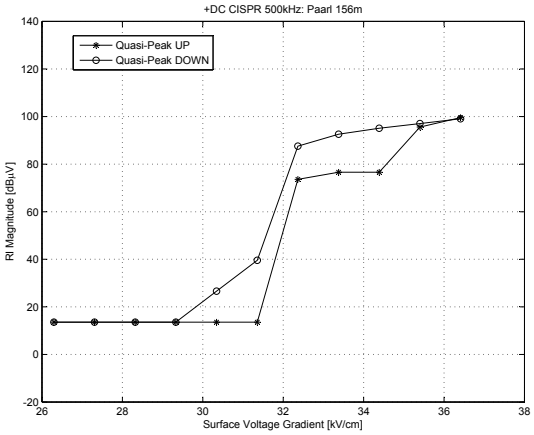

Figure E.31: Positive DC quasi-keak results for CISPR narrowband measurements moving up and down in voltage (Paarl)

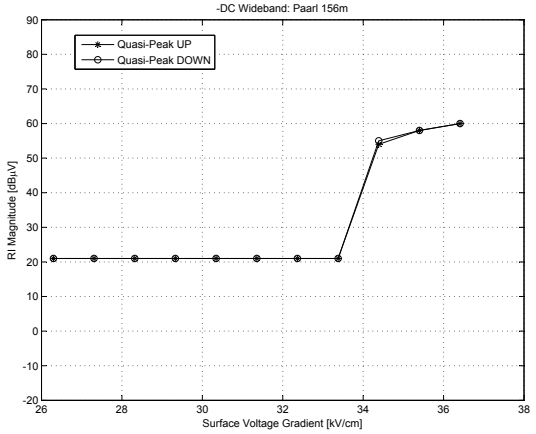

Figure E.32: Negative DC quasi-peak results for wideband measurements moving up and down in voltage (Paarl)

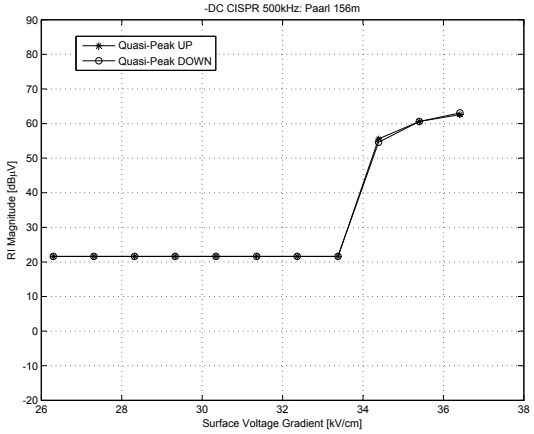

Figure E.33: Negative DC quasi-peak results for CISPR narrowband measurements moving up and down in voltage (Paarl)

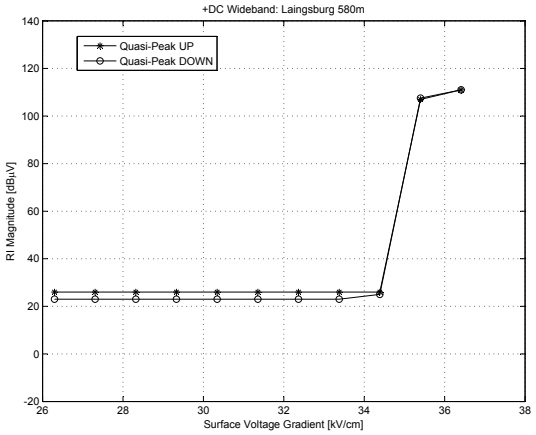

Figure E.34: Positive DC quasi-peak results for wideband measurements moving up and down in voltage (Laingsburg)

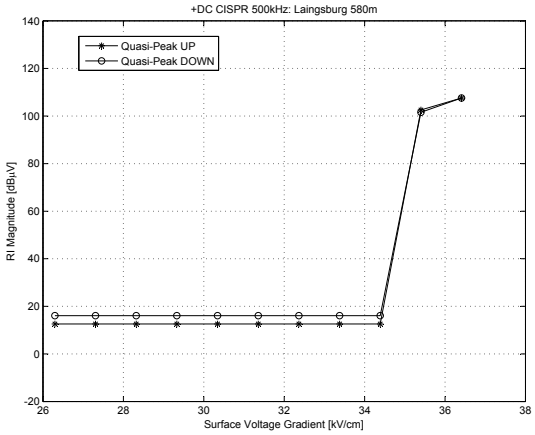

Figure E.35: Positive DC quasi-keak results for CISPR narrowband measurements moving up and down in voltage (Laingsburg)

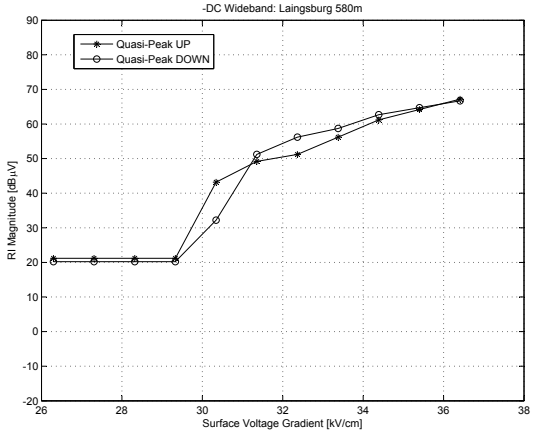

Figure E.36: Negative DC quasi-peak results for wideband measurements moving up and down in voltage (Laingsburg)

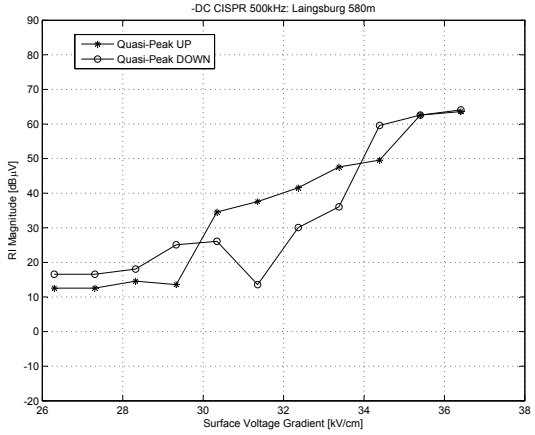

Figure E.37: Negative DC quasi-peak results for CISPR narrowband measurements moving up and down in voltage (Laingsburg)

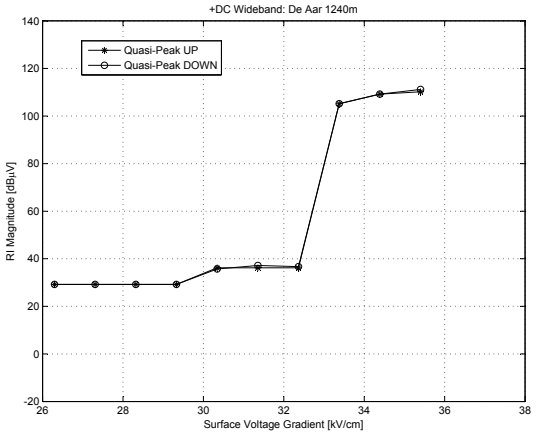

Figure E.38: Positive DC quasi-peak results for wideband measurements moving up and down in voltage (De Aar)

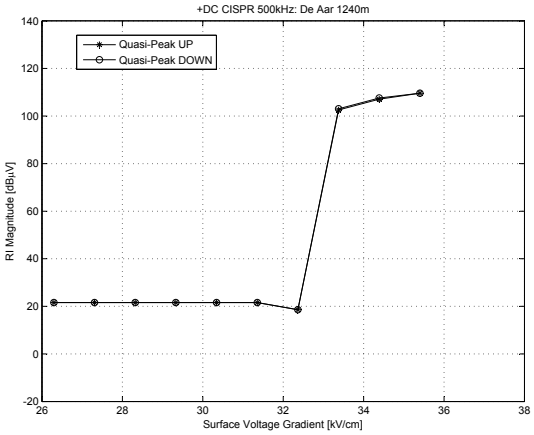

Figure E.39: Positive DC quasi-keak results for CISPR narrowband measurements moving up and down in voltage (De Aar)

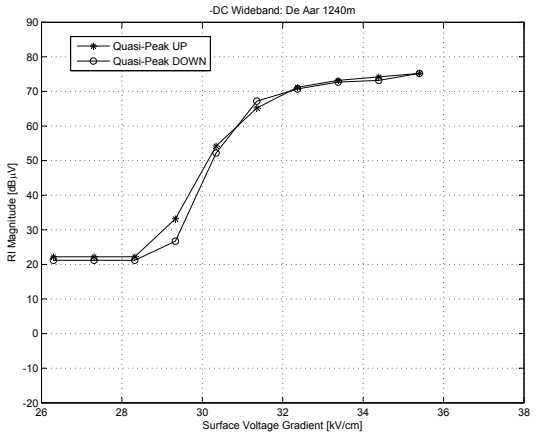

Figure E.40: Negative DC quasi-peak results for wideband measurements moving up and down in voltage (De Aar)

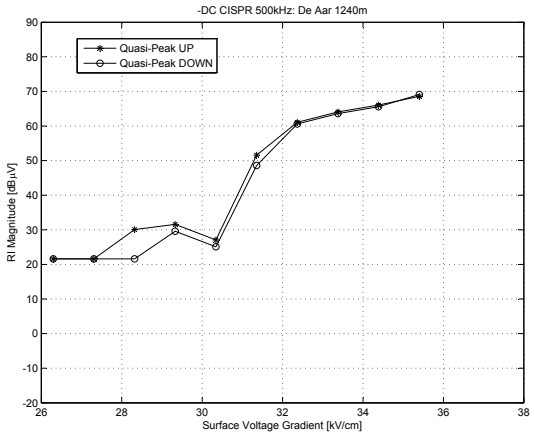

Figure E.41: Negative DC quasi-peak results for CISPR narrowband measurements moving up and down in voltage (De Aar)

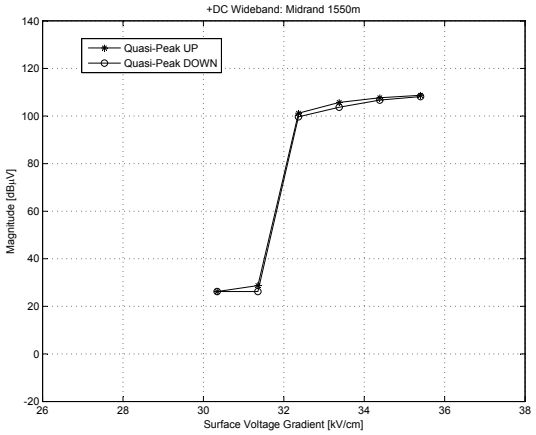

Figure E.42: Positive DC quasi-peak results for wideband measurements moving up and down in voltage (Midrand)

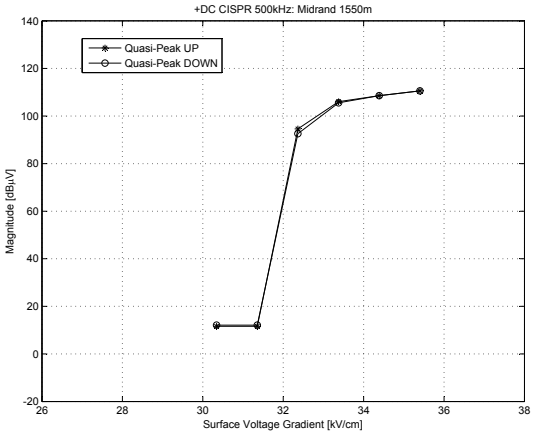

Figure E.43: Positive DC quasi-keak results for CISPR narrowband measurements moving up and down in voltage (Midrand)

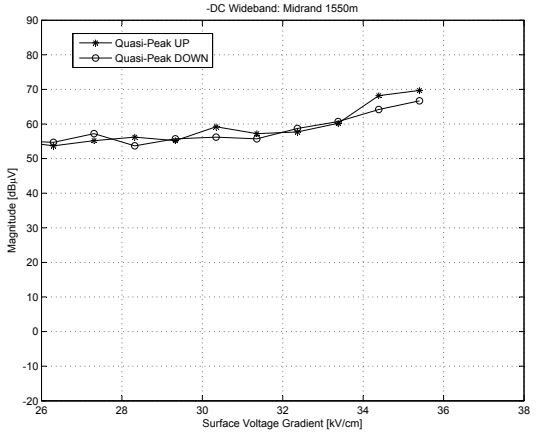

Figure E.44: Negative DC quasi-peak results for wideband measurements moving up and down in voltage (Midrand)

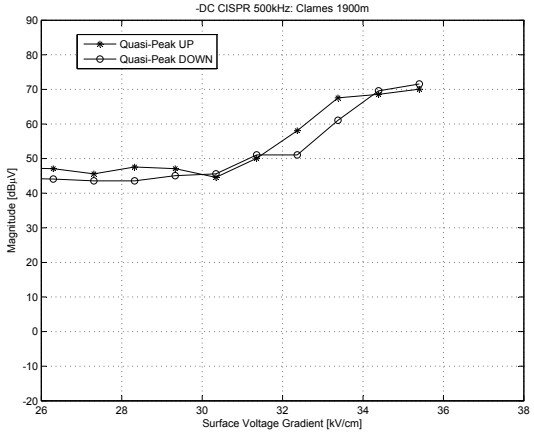

Figure E.45: Negative DC quasi-peak results for CISPR narrowband measurements moving up and down in voltage (Midrand)

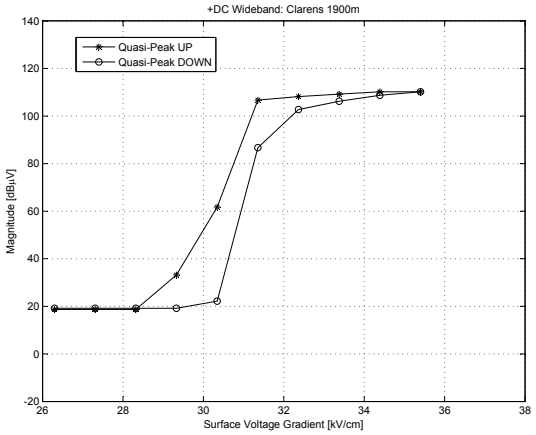

Figure E.46: Positive DC quasi-peak results for wideband measurements moving up and down in voltage (Clarens)

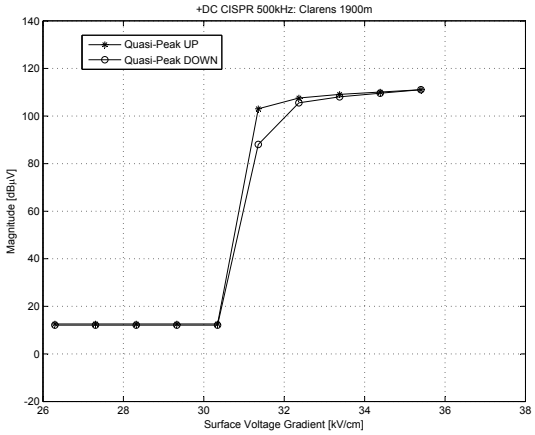

Figure E.47: Positive DC quasi-keak results for CISPR narrowband measurements moving up and down in voltage (Clarens)

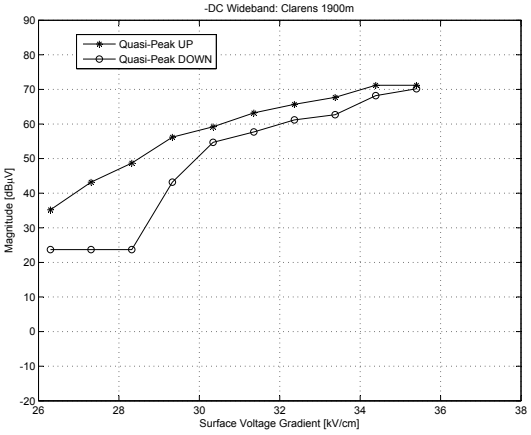

Figure E.48: Negative DC quasi-peak results for wideband measurements moving up and down in voltage (Clarens)

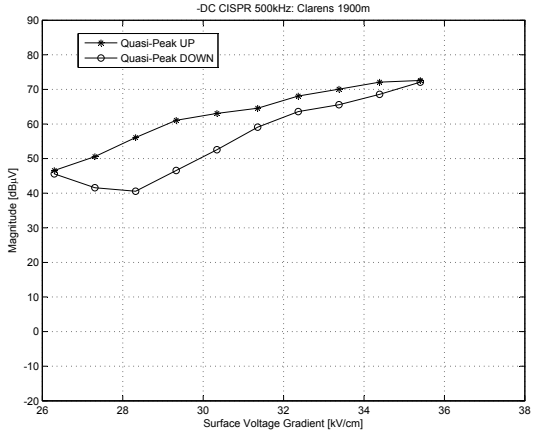

Figure E.49: Negative DC quasi-peak results for CISPR narrowband measurements moving up and down in voltage (Clarens)